The Dissertation Committee for Matthew Warren McCormick Certifies that this is the approved version of the following dissertation:

Study of Picosecond-Scale Electron Dynamics in Laser-Produced Plasmas with and without an External Magnetic Field

Committee:

Todd Ditmire, Supervisor

Roger Bengtson

Mike Downer

Melvin Oakes

Gary Hallock

Study of Picosecond-Scale Electron Dynamics in Laser-Produced Plasmas with and without an External Magnetic Field

by

Matthew Warren McCormick, B.S.

Dissertation

Presented to the Faculty of the Graduate School of

The University of Texas at Austin

in Partial Fulfillment

of the Requirements

for the Degree of

Doctor of Philosophy

The University of Texas at Austin

December, 2013

Acknowledgements

There are a great number of people who contributed to the work presented here, some directly by helping out in some way, and some indirectly through moral support or other means. I hope to cover everyone with the appreciation they deserve, but if I manage to leave someone out, know that I do appreciate what you did to help even if I forgot to acknowledge it here. First, I must thank my advisor, Todd Ditmire. Obviously, he gave me the opportunity to work on this project and was able to support me and this work financially, which was extremely helpful. But more than that, he helped me see the importance of a result when maybe it wasn't immediately obvious to me, and generally supplied the enthusiasm that I sometimes (or quite often, depending on the point of view) lacked. I also thank the National Physical Science Consortium for awarding me a fellowship which funded me during four years of my time, as well as those who helped me receive that award.

Next, I have to thank those who helped with the design and construction of my pulsed power device, as I had basically no idea where to start with that when I began work. A very special thanks goes to Orlin Gotchev, who worked at the Omega facility at the University of Rochester at the time, for showing Hernan and I his pulsed power device, which was extremely useful. Thanks also to Keith Carter for his many hours of help, as well as providing the hardware for the charging and discharging of the device. I also appreciated the many conversations we had over the years. The fabrication of all of the custom parts was performed in the UT Physics Machine Shop, and so I extend a great thanks to those who contributed to that: Allan, Danny, George, Jay, Jeff, Herb, Richard, Terry, and Bryan. Thanks also to Jack in the Student Shop for all his help when I needed to modify or make something, as well as teaching me how to use the various tools. I also thank Gary and Robert in the Electronics Shop, as well as Lanny and Ed in the Cryo Shop, for their help and advice during my time. Lastly, I thank Ken Struve at Sandia National Labs for his advice, especially related to the design of the vacuum feedthrough.

Study of Picosecond-Scale Electron Dynamics in Laser-Produced Plasmas with and without an External Magnetic Field

Matthew Warren McCormick, Ph.D.

The University of Texas at Austin, 2013

Supervisor: Todd Ditmire

The interaction of ultra-short laser pulses and cluster targets can be used to explore a number of interesting phenomena, ranging from nuclear fusion to astrophysical blast waves. In our experiments, we focused on exploring very fast plasma dynamics of a plasma created by ionizing clusters and monomer gas. By using a 115 fs laser pulse, we can even study sub-picosecond plasma dynamics. In addition, we also wanted to impose an external magnetic field on these plasmas to study how the plasma evolution would change. The results of this work produced two significant results. First, a new, extremely fast ionization mechanism, with velocities as high as 0.5 c, was discovered which allows for significant plasma expansion on a picosecond time-scale. Experimental studies measured the velocity of the ionization wave, while particle-in-cell simulations helped explain the source and longevity of the wave. It was also observed that this ionization wave was not affected by the external magnetic field. Second, the external field was shown to inhibit plasma expansion on a time-scale of tens of picoseconds, which seems to be one of the first demonstrations of magnetic confinement on such a fast time-scale. Simple 1D simulations tell us that the field appears to slow electron heat transport in the plasma as well as inhibiting collisional ionization of electrons expanding into the surrounding gas. The inhibition of plasma expansion by the field on this time-scale may provide some evidence that magnetic confinement of a fusion plasma created by exploding clusters could improve the fusion yield by slowing heat loss as well as possibly electrostatically confining the hot ions.

Table of Contents

List of Tables

List of Figures

Chapter 1. Introduction

1.1. OVERVIEW

The interaction of high intensity laser pulses with a variety of targets has been the subject of intense research over the past 25 years thanks to the advent of chirped pulse amplification [1]. Generally, solid or gas targets have been used, which have yielded interesting results. Examples of results generated by irradiating solid targets with intense laser pulses are highly energetic electron [2] and ion [3] beams, megagauss magnetic fields [4], and this interaction is the focus of work trying to initiate positive-yield inertial confinement fusion reactions [5]. Gas targets have generated interesting results as well, such as laser wakefield acceleration [6], high harmonic generation [7], and filament propagation [8]. Solids targets have the advantage of very high absorption of the laser energy, but debris generation can be problematic. Conversely, gas targets do not generate debris, but the absorption of laser energy is often very low.

Atomic clusters result from the adiabatic expansion of gas, usually at pressures above atmospheric, into vacuum, which causes the atoms (or molecules) to condense into small droplets. The first observation of clusters was nearly 60 years ago [9], and the use of clusters in high intensity laser experiments was roughly 20 years ago [10]. The advantage of this media is that it combines the positive aspects of both gases and solids – the average density is similar to a gas, so there are no debris concerns, but the clusters have near solid density, which results in much more efficient absorption of the laser energy. Many interesting experimental results have come from the irradiation of clusters by intense laser pulses, such as nuclear fusion [11], optical harmonics [12], plasma waveguides [13], and blast wave generation [14]. In this work, we will focus on more fundamental studies of laser-cluster interactions.

1.2. MOTIVATION AND PLAN FOR THE THESIS

The experimental results briefly covered in the previous section generally involve physics which deals with ion motion or electron collisions, and consequently, the time-

scale of such observations is generally on the order of nanoseconds, with occasional results being in the tens to hundreds of picoseconds range. As a result, comparatively few experiments have focused on the dynamics of plasmas generated by laser-cluster interaction on a picosecond time-scale. In addition, the observation of nuclear fusion reactions has naturally led to the idea of trying to implement an external magnetic field around the fusion plasma in an effort to improve the fusion yield. In both of these cases, the dynamics of electron motion in the plasma can play an important role in the physics of these plasmas, and thus, the focus of this work is to study electron motion and transport in a laser-cluster plasma with and without an external magnetic field. The time-scale of these observations will be in the first 100 picoseconds after the laser has produced the plasma.

The outline of this dissertation is as follows. In Chapter 2, a theoretical overview of the physics relevant to this research will be presented. In Chapter 3, an overview of two major design projects will be presented. First, a pulsed power device was needed to produce the magnetic field for these experiments, and the construction and testing of this device is covered. Then, in addition to the experiments performed, a separate design project was taken on which involved upgrading two of the amplification stages of one of the lasers in our research group. The results of this work are covered as well. In Chapter 4, an overview of the laser system used for these experiments is presented along with a description of the experimental layouts. Then, the diagnostics used to gather the data are described.

Chapter 5 presents the first main experimental result of our study of the plasma dynamics in the first 2-3 ps after the laser interaction. The details of the data analysis, as well as the results of theoretical simulations, are covered. Then, Chapter 6 presents the results of the effect of an external magnetic field on the laser plasma in the first 100 ps of the plasma evolution. Again, a presentation of the data analysis and theoretical modeling will be covered. Finally, a summary of the results and applications of this work will be discussed in Chapter 7.

Chapter 2. Theoretical Background

In this chapter, the essential physics needed to understand the results of the experiments are reviewed. First, an overview of the interaction of a high-intensity laser pulse with monomer gas and atomic clusters will be covered, which is applicable especially to the results of Chapter 5. Then, relevant plasma parameters and the physics of electron transport in a plasma with and without an external magnetic field will be discussed.

2.1. PHYSICS OF LASER INTERACTION WITH CLUSTERS AND GAS

2.1.1. Free Electron in a Laser Electric Field

Before we examine laser ionization of a cluster or gas, first let us consider the behavior of a free electron under the influence of the electric field of a laser pulse. The electric field E, with amplitude E_0, can be written as

$$E(t) = Re(E_0 e^{-i\omega_0 t}) = E_0 \cos \omega_0 t \tag{2.1}$$

where ω_0 is the frequency of the laser. The equation of motion of the electron is then

$$m_e \frac{dv}{dt} = qE_0 \cos \omega_0 t \tag{2.2}$$

where q and m_e are the electron charge and mass, respectively. Solving for v, we get

$$v(t) = \frac{qE_0}{m_e \omega_0} \sin \omega_0 t \tag{2.3}$$

We can now find the kinetic energy of the electron in the laser field averaged over a laser cycle, which is commonly referred to as the ponderomotive potential of the electron. This quantity plays a role in determining what ionization mechanisms are important. The ponderomotive potential is given by

$$U_p = \frac{m_e}{2} \langle v(t)^2 \rangle = \frac{m_e}{2} \left(\frac{qE_0}{m_e \omega_0} \right)^2 \langle \sin^2 \omega_0 t \rangle = \frac{q^2 E_0^2}{4 m_e \omega_0^2} \tag{2.4}$$

Rewriting this equation to make use of common laser parameters such as the intensity in vacuum $I = c\varepsilon_0 E_0^2 / 2$ and the wavelength λ, we get

$$U_p[\text{eV}] = 9.33 \times 10^{-14} I \left[\frac{W}{cm^2}\right] \lambda^2 [\mu m^2] \qquad (2.5)$$

It is important to note that this is the energy of the electron only while under the influence of the laser field. If the electron is initially at rest, and does not experience any collisions or forces while the laser is interacting with it, the electron will remain at rest once the laser pulse has passed due to conservation of energy. However, when a laser pulse is ionizing electrons, there are ways for the electrons to retain energy following their interaction with the laser, which will be described in later sections.

2.1.2. Laser Ionization of an Atom

When considering the mechanisms in which a laser pulse can ionize an atom, a constant called the Keldysh parameter [15] is often used, which is given by

$$\gamma_K = \sqrt{\frac{I_P}{2U_P}} \qquad (2.6)$$

where I_p is the ionization potential of the atom (or ion) to be ionized. When $\gamma_K > 1$, the common ionization mechanism is multiphoton ionization. In this case, U_p is less than the ionization potential, so the electron will need to absorb multiple photons of energy $h\nu$ to reach the energy needed to liberate the electron. For the purposes of this work, this regime is not important (at least for the first few ionization levels) as we are using laser intensities greater than 10^{14} W/cm^2. Indeed, the ponderomotive potential for a laser with wavelength 1057 nm at that intensity is about 10 eV, which is about the threshold when $\gamma_K \approx 1$.

In the range of intensities where $\gamma_K \geq 1$, from 10^{13}-10^{15} W/cm^2 depending on ionization level, the electrons can absorb more photons than what is required for ionization, which results in the electrons carrying away excess kinetic energy. This process is called above-threshold ionization (ATI), which was first observed in 1979 [16]. However, the energy gained by the electron will generally be less than twice the ponderomotive potential, although it is possible for electrons to gain up to $10U_P$ [17]. As a result, electrons which are ionized at these low intensities will not be very energetic.

4

In the intensity range of $10^{14} - 10^{18}$ W/cm^2 (for ~ 1 μm laser wavelengths), $\gamma_K < 1$ and the predominant ionization mechanism is what is called tunneling ionization. At these intensities, the electric field of the laser pulse is strong enough to distort the Coulomb potential of the atom, as shown in Figure 1. The ionization rate due to tunneling in a hydrogen-like ion in a quasi-static electric field is given by [18]

$$W = 4\omega_a \left(\frac{I_P}{I_H}\right)^{5/2} \frac{E_a}{|E(t)|} \exp\left[-\frac{2}{3}\left(\frac{I_P}{I_H}\right)^{3/2} \frac{E_a}{|E(t)|}\right] \tag{2.7}$$

where $\omega_a = 4.13 \times 10^{16}$ s^{-1} is the atomic unit of frequency, $E_a = 5.14 \times 10^9$ V/cm is the atomic unit of electric field, I_H is the ionization potential of hydrogen, and $E(t)$ is the instantaneous applied electric field strength. A more complete calculation of the ionization rate for more complex atoms and ions was developed by Ammosov, Delone, and Krainov, which is known as the ADK ionization rate [19]. This ionization rate, which is averaged over one optical cycle, is given by

$$W_{ADK} = \omega_a C_{n^*l}^2 f(l,m) \sqrt{\frac{3E_0}{4\pi E_a}} \left(\frac{I_P}{I_H}\right)^{\frac{1}{4}} \left(2\frac{E_a}{E_0}\left(\frac{I_P}{I_H}\right)^{\frac{3}{2}}\right)^{2n^*-|m|-1} \exp\left[-\frac{2}{3}\frac{E_a}{E_0}\left(\frac{I_P}{I_H}\right)^{\frac{3}{2}}\right]$$

$$C_{n^*l} = \left(\frac{2e}{n^*}\right)^{n^*} \frac{1}{\sqrt{2\pi n^*}} \tag{2.8}$$

$$f(l,m) = \frac{(2l+1)(l+|m|)!}{2^{|m|}|m|!\,(l-|m|)!}$$

where $e = 2.718...$, and $n^* = Z\sqrt{I_H/I_P}$, l, and m are the effective principal, angular momentum, and magnetic quantum numbers, respectively. Experiments have verified the accuracy of this formula for various atoms over a wide range of laser intensities [20]. For completeness, the ionization rate in a static field is given by

$$W_{ADK} = \omega_a C_{n^*l}^2 f(l,m) \frac{I_P}{2I_H} \left(2\frac{E_a}{E_0}\left(\frac{I_P}{I_H}\right)^{\frac{3}{2}}\right)^{2n^*-|m|-1} \exp\left[-\frac{2}{3}\frac{E_a}{E_0}\left(\frac{I_P}{I_H}\right)^{\frac{3}{2}}\right] \tag{2.9}$$

Let us quickly compare these rates with an example. Using an intensity of 10^{15} W/cm^2 to ionize the first electron of argon (I_p = 15.76 eV), Equations (2.7-9) give values for W^{-1} of 0.1 fs, 3.5 fs, and 1.3 fs (the equivalent static field strength is 8.7×10^8 V/cm).

atomic potential
$\phi = q^2/r$

electron wavepacket

Before laser interaction

Laser field
$\phi = qEx \sin \omega_0 t$

distorted potential

electron tunnels through

During laser interaction
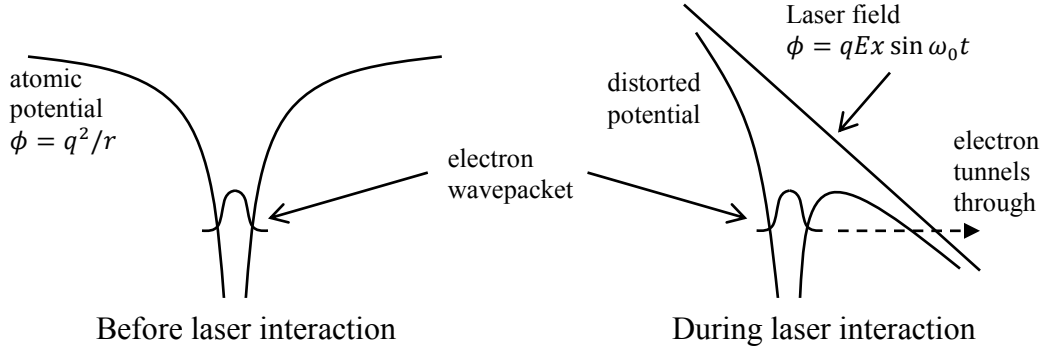
Figure 1.   Illustration of tunneling ionization of an atom by a strong laser field.

When examining the ionization rates given above, the strong exponential dependence on the incident electric field (and hence, intensity) is clear, which indicates that the rate will quickly saturate as the intensity is increased. This can be visualized by looking again at Figure 1. As the laser field gets stronger, eventually the Coulomb potential will become so distorted that the electron will "fall out" of the atom. This is known as barrier suppression ionization (BSI) [20]. The threshold intensity at which an electron can freely escape the Coulomb potential is given by

$$I_{BSI} = \frac{cI_P^4}{128\pi Z^2 q^6} = 4 \times 10^9 (I_P[\text{eV}])^4 Z^{-2} \qquad (2.10)$$

where Z is the charge of the ion being created and the practical formula on the right side gives the intensity in W/cm^2. While this equation is rather simple, it has been found to be quite accurate.

2.1.3. Laser Ionization of Clusters

Clusters are assemblages of atoms (or small molecules) which are normally bound together via van der Waals forces. Clusters are an interesting media for laser experiments because they combine low average density of the collective gas with near solid density,

6

nanometer-scale particles that absorb laser energy very efficiently [21]. The ionization mechanics of a cluster are somewhat different from individual atoms. In fact, there are two general steps involved in the ionization of a cluster [22]. First, the atoms inside are ionized, which is referred to as inner ionization. While the electrons are free, they are still confined within the potential well of the entire cluster, and hence the cluster has no net charge. If the laser field is strong enough, the next step of ionization can occur, which is naturally called outer ionization. Here, the ionized electrons are liberated from the cluster, which leads to a net positive charge developing on the cluster. In addition, the ionized electrons can gain considerable energy through various heating processes, which is an important difference between clusters and individual atoms.

During the inner ionization process, the atoms inside are often ionized via the tunnel ionization process described in the previous section. In fact, the ionization rate can be enhanced because the Coulomb potential of the atoms can be lowered by nearby ions as a result of the high local density [23]. However, because of the high interior density of the cluster, electron collisional ionization can play an important role. The rate of this ionization process is given by the Lotz formula [21,24]

$$W_{las} = n_e \frac{a_i Q_i}{\pi I_P} \left(\frac{1}{m_e U_P}\right)^{\frac{1}{2}} \int_{I_p}^{2U_p} \frac{\ln(K_e/I_P)}{2K_e} \frac{1}{\sqrt{1 - K_e/2U_P}} dK_e \qquad (2.11)$$

where $a_i = 4.15 \times 10^{-14}$ eV^2 cm^{-3}, Q_i is the number of electrons in the outer shell, and K_e is the kinetic energy of the ionizing electron. Once the collisional ionization begins, it will tend to dominate the ionization of the cluster. In fact, this process can lead to charge states in the cluster that are higher than what standard tunneling/barrier suppression ionization would predict for a given intensity [25,26].

As the laser intensity increases, the inner ionized electrons can start to become outer ionized by the laser electric field. This can happen if the laser field is stronger than the electric field of the cluster, namely

$$E_0 > q Q_{cl}/R_0^2 \qquad (2.12)$$

where Q_{cl} is the net charge on the cluster and R_0 is the radius of the cluster. If the peak intensity is higher than the total charge of the cluster, assuming all electrons are outer

ionized on a time-scale less than the pulse duration, the ball of positively-charged ions will naturally expand rapidly, which is appropriately called a Coulomb explosion. This can only be attained under certain conditions, one of which is that the laser pulse duration must be very short, ideally less than 100 fs [27]. If the laser field is comparable to the field of the cluster, the number of electrons extracted by the laser can be written as [28]

$$N_{ext} = 12\pi \frac{n_e R_0^2 q E_0}{m_e \omega_p^2} \tag{2.13}$$

where ω_p is the plasma frequency (see Equation (4.3)).

As mentioned at the beginning of this section, the electrons that are ionized from clusters can be heated by various mechanisms to very high energies. A brief survey of these heating mechanisms will be presented here. The first mechanism is called inverse bremsstrahlung heating [29]. As the electrons are ionized, they can move with the laser field inside the cluster. However, unlike in the case of a single electron in the laser field discussed in Section 2.1.1., collisions will occur and the electron will gain energy. Generally, this heating mechanism will be most efficient in the early stages when the cluster is near solid density and has not expanded much. A second heating mechanism which is most efficient in the early stages is called vacuum heating [30]. Electrons near the surface of the cluster can be pulled into the vacuum, but are still bound to the cluster by space charge forces. While outside the cluster, the electrons obtain the quiver energy of the laser, and then are driven back into the cluster. If a sufficient number of electrons have been inner ionized such that the electron density is higher than the critical density (Equation (4.4)), the heated electrons will deposit their energy into the cluster via collisions. Successive repetitions of this process can result in very energetic electrons. Finally, as the cluster expands, the internal electron density will decrease. When the electron density reaches three times the critical density, resonance absorption can occur, which has become known as resonant heating of a cluster [21]. A number of experiments have shown that the heating mechanisms that laser interaction with clusters enables can generate electrons with energies far above the ponderomotive potential of the laser [31,32,33].

2.1.4. Cluster Behavior after Laser Ionization

Once the laser has passed (or during the second half of the laser pulse, when the intensity is dropping from peak), the cluster will naturally expand and disintegrate. How this happens depends strongly on how much and how fast the laser ionized the cluster, as well as the degree of outer ionization. There are two primary mechanisms by which the cluster will disintegrate – a very fast Coulomb explosion [34], and a slower hydrodynamic expansion [21]. A brief overview of these will now be covered.

In order for a Coulomb explosion to occur, all (or nearly all) of the electrons need to be outer ionized from the cluster in a very short time. If this is achieved, the ball of positively-charged ions that remains will "explode" from the Coulomb force of repulsion between the ions, which can generate ions with energies of many keV. This is the common mechanism which allows fusion reactions to occur in laser-cluster experiments using deuterium [35]. However, as mentioned in the previous section, this can generally only happen with very short laser pulses because the cluster needs to be completely outer ionized before the cluster can expand appreciably. The general rule used is that this would need to happen before the cluster can double in radius, which leads to the requirement that ionization occur on the order of 20 fs [36]. Also, this can usually only occur with clusters of lower-Z atoms since the time and laser intensity required to completely outer ionize higher-Z clusters would most likely not permit a Coulomb explosion to happen. Because of these conditions, Coulomb explosions are not expected to play a part in the experiments described later in this work. However, this is not to say that Coulomb forces do not "help" the clusters expand.

The other mechanism of hydrodynamic expansion happens when the cluster has a significant fraction (or all) of the electrons inner ionized. In this case, depending on the parameters of the interaction, the cluster will expand from the thermal pressure of the heated electrons. The ions in the cluster get pulled by the electrons as they leave the cluster, which results in the ions gaining energy from the electrons. The maximum energy the ions can receive is the initial energy of the electrons, so when we equate these quantities, we can find the velocity that the ions can achieve. This turns out to be

$$v_i = \sqrt{\frac{ZkT_e}{m_i}} = c_s \qquad (2.14)$$

which is also known as the sound speed for the plasma.

2.2. ELECTRON TRANSPORT IN LASER PLASMAS

This section defines a few of the most relevant basic plasma parameters which will be encountered in the analysis of the data covered in Chapters 5 and 6. Also, the way that the parameters in Sections 2.2.1 – 2.2.3 compare will provide clues as to what possible phenomena can be occurring within the plasma. Most of the material presented here follows the discussion in the relevant sections of the excellent book by Chen [37].

2.2.1. Debye Shielding

A well-known characteristic of plasma is the ability to screen out electric (or magnetic in some cases) fields. As an example, imagine a ball with a net positive charge is inserted into a plasma (with a protective insulator). Naturally, the electric field from this ball will attract electrons from nearby until the field is effectively cancelled out. However, since the electrons in the plasma have thermal motion, some will escape the electric potential of the ball at a distance where the electric field is weaker. This defines the extent of the shielding cloud of electrons, which is known as the Debye length. The solution for this situation, which can be derived starting from Poisson's equation, is

$$\Phi = \Phi_0 \exp(-|x|/\lambda_D) \qquad (2.15)$$

where Φ is the electric potential and λ_D is the Debye length,

$$\lambda_D = \sqrt{\frac{\varepsilon_0 kT_e}{n_e q^2}} \qquad (2.16)$$

where ε_0 is the vacuum permittivity and kT_e is the electron temperature.

A similar situation can occur near the edge of a plasma created by a laser. The previous section discussed how lasers can heat electrons to very high temperatures, but the laser only ionizes material within a certain area. This means that there will be a

boundary between the plasma and matter which is not ionized. When the hot electrons try to escape the plasma at this boundary, the ions will electrostatically confine the electrons and not allow them to escape (unless they are so hot that they can overcome the potential of the plasma). Once again, this confinement will occur on the scale of the Debye length, which can result in a large electric field at the plasma boundary (this is often called a sheath field). This situation will be discussed in more detail in Chapter 5 as it is important to the interpretation of the data.

2.2.2. Electron Larmor Radius

All charged particle motions are described by the Lorentz equation,

$$m\frac{d\vec{v}}{dt} = q(\vec{E} + \vec{v} \times \vec{B})$$

(2.17)

For the situation applicable to this work, we will consider the situation for electrons when the electric field is zero and the magnetic field has only one component, taken to be in the z direction, $\vec{B} = B\hat{z}$. Separating the vectors by their components, the Lorentz equation then becomes

$$m_e\ddot{x} = qB\dot{y} \qquad m_e\ddot{y} = -qB\dot{x}$$

(2.18)

with the time derivatives represented by dots. We can define $\omega_c = qB/m_e$ as the cyclotron frequency, and the solution to these coupled equations is

$$x(t) = C_1 \cos \omega_c t + C_2 \sin \omega_c t + C_3$$
$$y(t) = C_2 \cos \omega_c t - C_1 \sin \omega_c t + C_4$$

(2.19)

Suppose the electron starts from a point (x_0, y_0) with a velocity of $\dot{x}(0) = v_\perp$ and $\dot{y}(0) = 0$. Using these initial conditions, the solution becomes

$$x(t) = x_0 + \frac{v_\perp}{\omega_c}\sin \omega_c t$$
$$y(t) = y_0 - \frac{v_\perp}{\omega_c} + \frac{v_\perp}{\omega_c}\cos \omega_c t$$

(2.20)

These equations can be squared and added together to produce a more recognizable form:

$$(x(t) - x_0)^2 + \left(y(t) - \left(y_0 - \frac{v_\perp}{\omega_c}\right)\right)^2 = \left(\frac{v_\perp}{\omega_c}\right)^2 \qquad (2.21)$$

This is the equation of a circle with radius $v_\perp/\omega_c$. Hence, as the electron moves in the plasma with a magnetic field present, it will rotate around a field line with what is called the Larmor radius:

$$R_L = \frac{v_\perp}{\omega_c} = \frac{m v_\perp}{qB} \qquad (2.22)$$

Of course, electrons in the plasma will certainly have a velocity component parallel to the magnetic field, which means the electrons will corkscrew around their respective field lines.

2.2.3. Mean Free Path and Collisions

The concept of a mean free path is derived from how far a particle can travel before it collides with another particle. This can mean a direct impact collision, as is the case between neutral particles or electron-neutral collisions, or Coulomb collisions, where a charged particle has its original trajectory redirected by a certain amount (a common choice is 90°) [38]. The subject of collisions between various types of particles has been an area of considerable study, but some first order estimates can be useful as a starting point.

Consider a flux Γ of electrons incident upon a slab of neutral atoms with area A, thickness dx, and density n_n. If the atoms are considered to be spheres with a cross section area of σ, the change in the flux after traversing the slab would be given by

$$\frac{d\Gamma}{dx} = -n_n \sigma \Gamma \qquad (2.23)$$

Solving this equation for Γ yields

$$\Gamma = \Gamma_0 e^{-n_n \sigma x} \qquad (2.24)$$

We can define

$$\lambda_m = \frac{1}{n_n \sigma} \qquad (2.25)$$

as the distance in which the flux would be decreased to $1/e$ of its initial value. This is the basic definition of the mean free path of a particle. If the particle – in this case, an electron – is traveling with a velocity v_e, the time between collisions is simply given by $\tau = \lambda_m/v_e$, and the collision frequency is then

$$\nu = n_n \sigma v_e \tag{2.26}$$

2.2.4. Plasma Transport Equations

While single particle dynamics are important in studying plasma physics, keeping track of the trajectories of, for example, 10^{18} particles per cm^3 would become overwhelming. Even particle-in-cell simulations, which do exactly that, normally track on the order of millions of particles in a calculation (usually less). A collective model for evolving the plasma in time is needed, and it has been found that the equations of fluid mechanics work quite well. In this section, these equations that govern the evolution of the electron and ion fluids will be briefly reviewed. Generally, we will focus on the equations related to electron motion since they are of interest to this work.

In the most general case, the distribution function for a species s, $f_s(\vec{r}, \vec{v}, t)$, contains the exact phase space information for that species. How each of the species in the plasma evolves with time is described by the kinetic (or Boltzmann) equations,

$$\frac{\partial f_s}{\partial t} + \vec{v_s} \cdot \nabla f_s + \frac{\vec{F}}{m} \cdot \frac{\partial f_s}{\partial \vec{v_s}} = \left(\frac{\partial f_s}{\partial t}\right)_c \tag{2.27}$$

In a hot, collisionless plasma, this equation takes on a special form known as the Vlasov equation,

$$\frac{\partial f}{\partial t} + \vec{u} \cdot \nabla f - \frac{q}{m}\left(\vec{E} + \vec{u} \times \vec{B}\right) \cdot \frac{\partial f}{\partial \vec{u}} = 0 \tag{2.28}$$

This kinetic description of the plasma often contains more information than is required, depending on the situation. In addition, finding solutions to the full kinetic equations is often quite hard. In order to simplify the situation, a fluid description of the plasma can be developed by taking moments of the kinetic equation. This has been described in

many textbooks, with the first derivation performed by Braginskii [39]. The fundamental equations for the fluid description of a plasma are given by

$$\frac{\partial n_e}{\partial t} + \nabla \cdot (n_e \vec{u}) = 0 \tag{2.29}$$

$$m_e n_e \frac{d\vec{u}}{dt} = -q n_e (\vec{E} + \vec{u} \times \vec{B}) - \nabla p_e - \nabla \cdot \overset{\leftrightarrow}{P} + \vec{R} \tag{2.30}$$

$$\frac{3}{2} n_e \frac{dT_e}{dt} + p_e \nabla \cdot \vec{u} = -\nabla \cdot \vec{q}_e - \overset{\leftrightarrow}{P} : \nabla \vec{u} + Q_e \tag{2.31}$$

In these equations, $\frac{d}{dt} = \frac{\partial}{\partial t} + \vec{u} \cdot \nabla$ is the convective derivative; $p_e = n_e T_e$; $\vec{R}$ is the momentum transfer by collisions, and is the sum of the friction force between the ion and electron fluid with the thermal force; Q_e is the heat generated in electrons from collisions with ions; and $\vec{q}_e$ is the electron heat flux. Expressions for these additional quantities can be found in Ref. 39 or the NRL Plasma Formulary [40].

2.2.5. Free and Magnetized Electron Diffusion

Charged particles in a plasma will move according to the Lorentz equation until collisions occur, which will change the equations of motion. As described earlier, there are various types of collisions that can occur in a plasma, and this will naturally cause the plasma to expand and diffuse. A rather simple estimate of how a plasma will diffuse can be derived from the fluid equation of motion, Equation (2.30). If the collision time is sufficiently small such that fluid elements in the plasma do not move much in a collision time, the left side of Equation (2.30) can be set to zero (with $B = 0$ and disregarding the higher order $\nabla \cdot \overset{\leftrightarrow}{P}$ term) and a drift velocity can be found:

$$v_d = \frac{q}{m_e v_e} E - \frac{kT_e}{m_e v_e} \frac{\nabla n_e}{n_e} \tag{2.32}$$

The coefficient of the electric field is called the mobility, which is not of as much concern for this work. The other coefficient is the diffusion coefficient, which gives a quantitative estimate for how a fluid will change based on a random-walk process. Obviously, this is the diffusion coefficient for plasma which has no external magnetic field present, so this can be considered to be free diffusion.

Conversely, when an external magnetic field is present, a different diffusion coefficient can be found. Chen goes over the derivation and arrives at the result that the diffusion coefficient in this case is

$$D = \frac{2n_e kT_e \eta_\perp}{B^2} = \frac{2n_e kT_e}{B^2} 1.03 \times 10^{-4} \frac{Z \ln \Lambda}{(T_e[\text{eV}])^{3/2}} \qquad (2.33)$$

where $\ln \Lambda$ is the familiar Coulomb logarithm, and $\eta_\perp$ is the Spitzer resistivity [41]. This has become known as the classical diffusion coefficient. However, experiments (at generally lower density) were unable to verify this scaling. In the late 1940's, Bohm, Burhop, and Massey proposed a different diffusion coefficient which accounted for larger electron diffusion via plasma oscillations [42]:

$$D_B = \frac{1}{16} \frac{kT_e}{qB} \qquad (2.34)$$

Drift velocities can be found using these coefficients by simply inserting them in place of the free diffusion coefficient in Equation (2.32).

Let us use these coefficients to see what we can expect from the plasma with and without the magnetic field present. It is worth noting that the effect of mobility will not be accounted for because we will assume the plasma is quasi-neutral, meaning that $E = 0$. Taking parameters which are relevant to the work that will be shown later, such as $T_e = 100$ eV, $n_e = 2 \times 10^{18}$ cm^{-3}, $B = 5$ T, and using an analytical fit of a starting electron density profile to estimate ∇n_e near the boundary of the plasma, we find the following results for the drift velocities: $v_{\text{free}} \approx 4$ µm/ps, $v_{\text{class}} \approx 0.05$ µm/ps, and $v_{\text{Bohm}} \approx 0.02$ µm/ps. It is interesting to note that the two coefficients give similar velocities for these parameters, quite unlike what they give for parameters representative of lower density fusion plasmas (Chen gives an example with similar conditions but the electron density is only 10^{13} cm^{-3}). However, there is a stark difference between the free and magnetized drift velocities. As will be seen in Chapter 6, our data showed noticeable restriction of the plasma expansion when the field was present, quite in line with what would be expected.

Chapter 3. Design Work

During the course of this work, two substantial design projects were completed. The first was necessary for the experiments performed – the design and construction of a pulsed power device to produce the external magnetic field. The second was part of an overall project to upgrade one of the laser systems in the research group. In this chapter, the work involved in the completion of these projects will be discussed.

3.1. DESIGN, CONSTRUCTION, AND TESTING OF PULSED POWER DEVICE

3.1.1. Design Considerations

The overall goal of building the pulsed power system was a simple, compact device that could produce moderate magnetic field strength (on the order of 10 T) as a proof of principle for experiments related to improving fusion yield from cluster fusion experiments. The main requirement was to minimize the total system inductance and resistance, which would help produce maximum current using minimum energy from the capacitors.

An electrical schematic of the circuit is shown in Figure 2. The charging supply is simply a transformer that takes up to 120 V AC input and produces up to 50 kV DC. The input voltage is controlled using a Variac, so that the output charging voltage can be controlled. A pair of 110 MΩ high voltage resistors in parallel limits the charge current to 1 mA. A high voltage relay is used to turn the charging voltage on and off. From here, the circuit is basically an LRC circuit. Four General Atomics 31160 low inductance capacitors (C = 220 nF each) are connected in parallel to one side of the discharge switch, which is a laser-triggered spark gap. The receiving side of the switch is connected to a transmission line, which delivers the current to the field coils. The current then returns back to the ground side of the capacitors, and since the circuit is underdamped, the current rings out when a discharge occurs. The capacitors have a 10 kΩ dump resistor and a HV relay connected across them to allow for safe dumping of the charge if a shot needs to be cancelled, as well as providing a safe way to keep the capacitors from building up
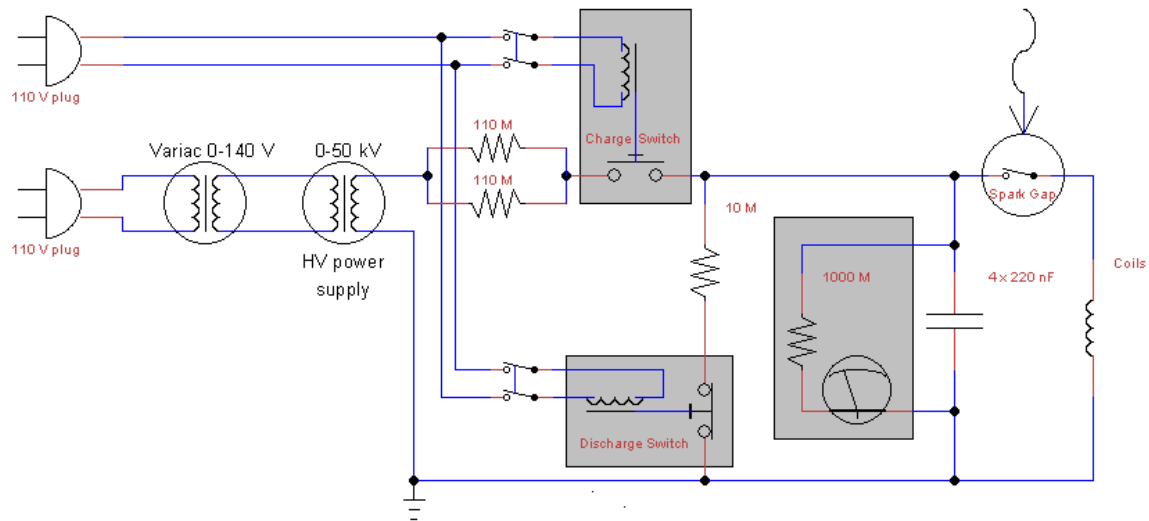
Figure 2.　　Electrical schematic of the pulsed power circuit.

charge when the system is not in use. Also, a custom-built voltage meter measures the voltage across the caps.

　　　　While the conceptual design of the circuit is rather simple, the mechanical design of the device was much more involved. Many design elements used in the construction of our system were modeled after a similar level device in use at the University of Rochester's Laboratory for Laser Energetics, the Magnetized-Inertial Fusion Electrical Delivery System (MIFEDS) [43]. The design of each of the major elements will now be discussed.

　　　　First, the laser spark gap used to trigger the system needed to be built. A picture and cross section view of the spark gap are shown in Figure 3. A spark gap relies on knowledge of the Paschen curve [44] for the gas to be used in the space between the electrodes. Our choice was to use dry nitrogen, usually at pressures between 20 and 50 PSI. The spacing of the copper electrodes could be controlled by rotating the receiving electrode in the plastic casing, but when the device was assembled, it would have been extremely difficult to change the spacing. O-rings between the electrodes and the casing kept the gas from leaking out. The laser used to trigger the spark gap was a Quantel Brilliant Q-switched Nd:YAG laser operating at 532 nm. To produce the most consistent,

17

low jitter discharges, the laser was run at full operation. While its nominal output is 200 mJ, the maximum output was usually around 80 mJ, most likely because the internal alignment was somewhat off. The laser was focused using a 7.5 cm focal length lens. The beam passed through a window on the back side of the charged electrode, and then through a ~1 mm hole in the front surface of the electrode. The focus was positioned so that it would be near the midpoint between the two electrodes. The receiving electrode had a cone-shaped hole drilled in it to serve as a beam dump for the laser pulse. The spark gap generally performed well, but after a few hundred shots, copper dust and electrical ablation of the electrodes would prevent the gap from holding off more than 15 kV before it would self-discharge, even with N_2 pressures higher than 50 PSI. This required the gap to be disassembled and cleaned occasionally.
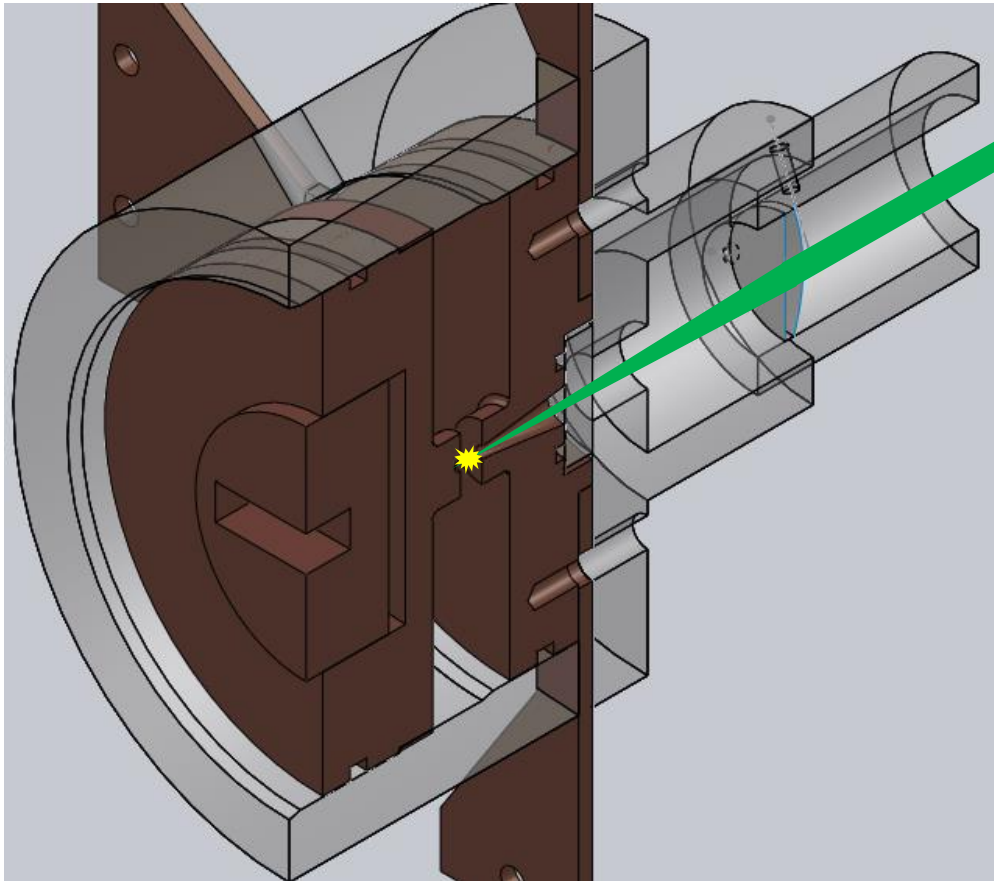
Figure 3.   Cross section rendering of the spark gap, showing the 532 nm trigger laser focusing between the electrodes.
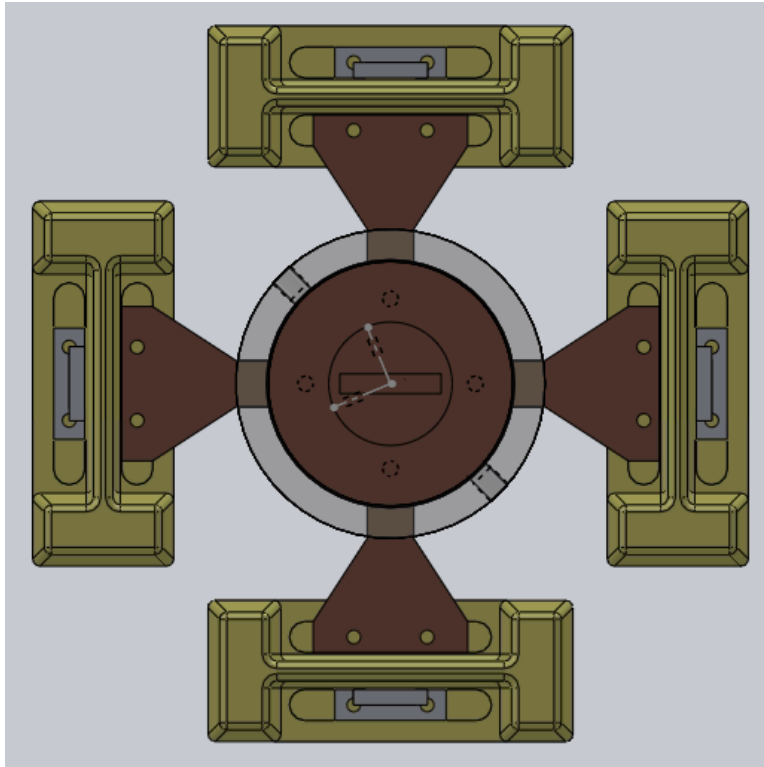
Figure 4.   Front view of the spark gap and capacitors.

The capacitors were mounted such that they were equidistant from the spark so that the discharge from all four caps would be timed to add maximally. As shown in Figure 4, the caps were mounted in a square with short plates connecting the charged side to the electrode of the spark gap. In order to minimize the inductance, it was also important to mount the caps as compactly as possible, which was simply determined by the size of the caps.

Next, the design of the transmission line had to be figured out. The MIFEDS device used a shielded stripline, similar to a rectangular coaxial line [45], and we decided to use a similar design, which is shown in Figure 5. The advantage of this design is that the current delivered to the coils is shielded from the chamber, and, if designed correctly, the inductance of the line can be quite low. The inductance estimates will be presented later, but it was decided to use a copper center conductor with dimensions 1.6" x 0.2" (with rounded corners), which toward the coil end would taper down to 0.4" x 0.2". The

aluminum shield was separated from the center conductor by 0.02" and insulated using Mylar sheet. The length was dependent on the chamber used for the experiment, so different length transmission lines were made.

Originally, we used coils similar to what MIFEDS used, which were coils cut from Pyralux sheet, which is thin copper sheet with a Kapton backing. Since the coils were so thin (less than 100 μm thick), they would be destroyed with every shot. Eventually, solid coils machined out of copper were made that would never be destroyed. Two single turn coils were the easiest to make, so the goal was to produce maximum field between the coils on axis. Since the nozzle of the gas jet needed to be near the plasma for optimal cluster conditions, the coils needed to be separated enough to let the nozzle between them. Coil dimensions were generally a separation of 4 mm and inner diameter of 4-7 mm, with each coil having width of ~1 mm. The solid coils had a radial thickness of about 4 mm.
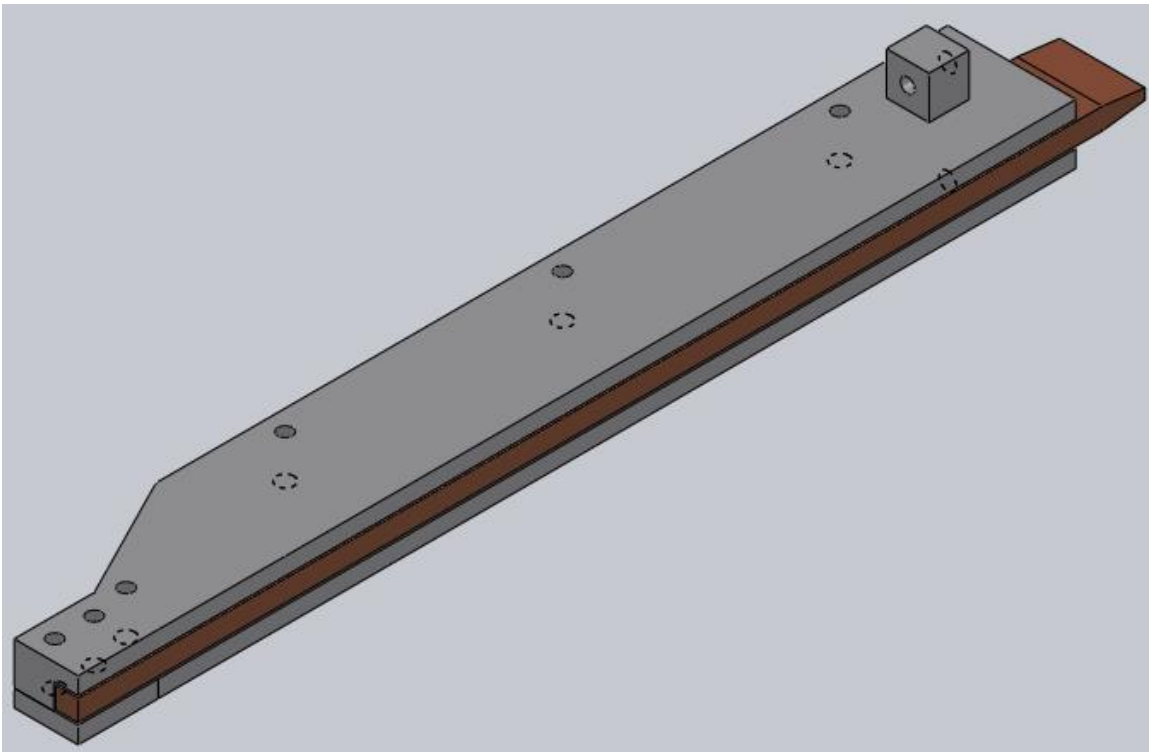
Figure 5.   Cross section view of the transmission line.

The final part needed was the vacuum feedthrough which would couple the current from the spark gap into the transmission line inside the chamber. This required a lot of thought since it had to be custom designed, low impedance, and for added safety, isolated from the chamber. Finally, the design which was used is shown in Figure 6. The center conductor couples to the receiving electrode of the spark cap via a plate in contact with brass fingerstock. It then passes through a Lexan insulator which has a round countersunk hole with an o-ring sealing the plastic to the center conductor. On the vacuum side, the center plate of the transmission is connected to the feedthrough using the same brass fingerstock. The return current passes through a holder which attaches the transmission line to the feedthrough. The plastic insulator seals against the return current plate, and the plate serves as the flange which connects to the chamber. Also, between the flange and the chamber is a 1/4" thick Lexan insulator, sealed with o-rings on both sides, which isolates the chamber from the current path. Four plates extend off of the ground flange which connect the return current to the capacitors via plates attached to the caps. A picture of the assembled device is shown in Figure 6.
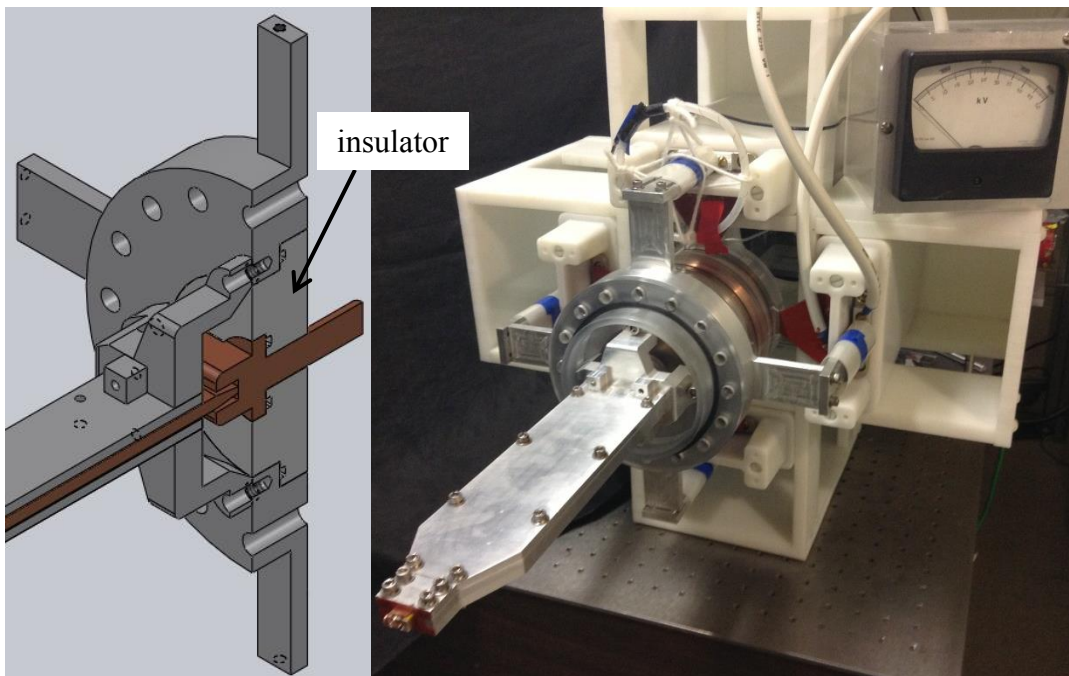
Figure 6.   Cross section view of the vacuum feedthrough (left) and picture of the assembled device (right).

The inductance of the system can be estimated using simple formulas. First, each capacitor has an internal inductance of 20 nH. Inductances add inversely in parallel, so the total inductance is 5 nH. The spark gap and feedthrough can be estimated using the formula for a coaxial line,

$$L = \frac{\mu_0 l}{2\pi} \ln \frac{b}{a}$$
(3.1)

where a, b, and l are the inner radius, outer radius, and length of the conductors, respectively. b is about 5", which is the distance from center of the aluminum arms connected to the caps, while a and l vary. For the dimensions of the parts, the estimate for this section is about 40 nH. Next is the transmission line, which can be estimated by using the formula for parallel plates,

$$L = \frac{\mu_0 l d}{w}$$
(3.2)

where d and w are the separation and width of the plates, respectively. Using the dimensions listed before, plus the length of each section (multiple lines were made, but all were less than two feet long), the total inductance is 10-15 nH. Finally, the inductance of the coils can be estimated using

$$L = \frac{\mu_0 \pi r^2}{a}$$
(3.3)

where r is the coil radius and a is the thickness of the coil. For a 2 mm radius and 1 mm thick coil, the inductance of one coil is about 16 nH. Since the two coils are in parallel, the inductance is reduced by a factor of two. The mutual inductance for the two coils can be calculated using [46]

$$M = \mu_0 r \frac{2}{k} \left(\left(1 - \frac{k^2}{2} \right) K(k) - E(k) \right), \quad k = \sqrt{\frac{4r^2}{r^2 + d^2}}$$
(3.4)

where $K(k)$ and $E(k)$ are the complete elliptic integrals and d is the separation of the coils, about 4 mm. This gives about 2 nH, so the total inductance of the coils is about 10 nH. The total system inductance, then, can be estimated to be about 65-70 nH, which is very close to the measured value as shown in the next section.

22

3.1.2. Initial Performance Results

With the device constructed, characterizing the operation was needed. The first step in the process was to measure the current the device could deliver at various charge voltages. Given the high currents we were hoping to achieve (up to 100 kA peak), most "off the shelf" current monitors would be insufficient, so a custom Rogowski coil [47] was made. A Rogowski coil is a toroidally wrapped wire which measures the magnetic field produced by a current flowing inside the area of the torus, as shown in Figure 7. The voltage induced by the magnetic flux, and hence the current, is

$$V = -\mu_0 \frac{n}{l} A \frac{dI}{dt} \tag{3.5}$$

where n is the number of turns, l is the length of the winding, I is the current enclosed, and A is the cross section area of the winding. As an example, taking a coil with diameter 5 cm, cross section radius of 3 mm, and 15 turns, with a current rise of 100 kA in 500 ns, the voltage measured would be 340 V. The actual coil made used magnet wire wrapped around a 0.25" diameter PVC tube. The radius of the tube was made to be about 1.5" and the wire had 17 turns. Calibration of the Rogowski was done using a Pearson Model 110
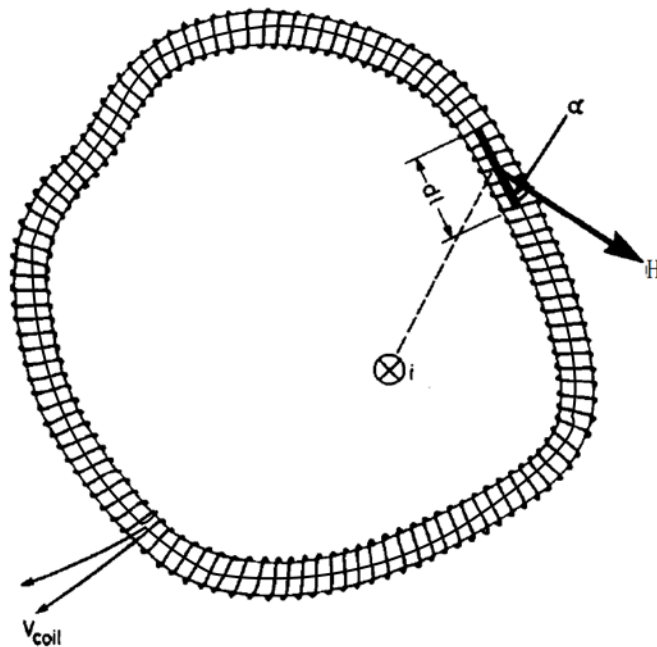
Figure 7.   Schematic view of a Rogowski coil.

Current Monitor which has a peak current of 5 kA, so the calibration was done at very low charge voltages and then extrapolated to higher voltages. Due to the high voltages that could be measured, two 10x attenuators were used when connecting the Rogowski to an oscilloscope. In practice, the Rogowski was installed to measure the return current through one of the bars connected to the ground side of one of the capacitors. Since the coil measures the derivative of the current, the signal is numerically integrated and multiplied by four (along with appropriate calibration factors) to give the total current.

A sample plot of measured Rogowski signal from a 35 kV discharge is shown in Figure 8a. In order to calculate the current that was measured, a least squares fit of the form $y = a\,e^{bt}\cos ct$ was used on the signal. The integral of this fit then gives the current. We can also use the current fit to determine what the inductance, resistance, and voltage of the discharge are. From Kirchoff's Voltage Law, the sum of the voltages across the elements in a circuit must equal zero, which for an LRC circuit gives

$$0 = L\frac{d^2Q}{dt^2} + R\frac{dQ}{dt} + \frac{Q}{C} = \frac{d^2Q}{dt^2} + \frac{R}{L}\frac{dQ}{dt} + \frac{Q}{LC} \qquad (3.6)$$

Solving for $Q(t)$ with the initial conditions $Q(0) = CV$ and $Q'(0) = 0$ gives a general solution of the form $Q(t) = A_1 e^{s_1 t} + A_2 e^{s_2 t}$. The derivative of the solution is the current, which after some algebra has the form $I(t) = ae^{bt}\sin ct$ with coefficients

$$a = \frac{2V}{\sqrt{\dfrac{4L - CR^2}{C}}} \qquad b = -\frac{R}{2L} \qquad c = \frac{\sqrt{\dfrac{4L - CR^2}{C}}}{2L} \qquad (3.7)$$

Using the value for C of 880 nF, and the values for the coefficients from the current fit, the values of L, R, and V are obtained. The reason V is not assumed to be known is because measurements of the voltage across the capacitors using a Tektronix P6015 high voltage probe showed that the DC charge voltage matched what the voltage meter read, but when the discharge started, the voltage would drop by 10-20%. Also, reading the voltage on the cathode side of the spark gap showed the peak voltage measured was again 10-20% less than the DC charge voltage. Sample plots showing these two observations are shown in Figure 8c, and Figure 8b shows the trend of how the DC charge voltage

24
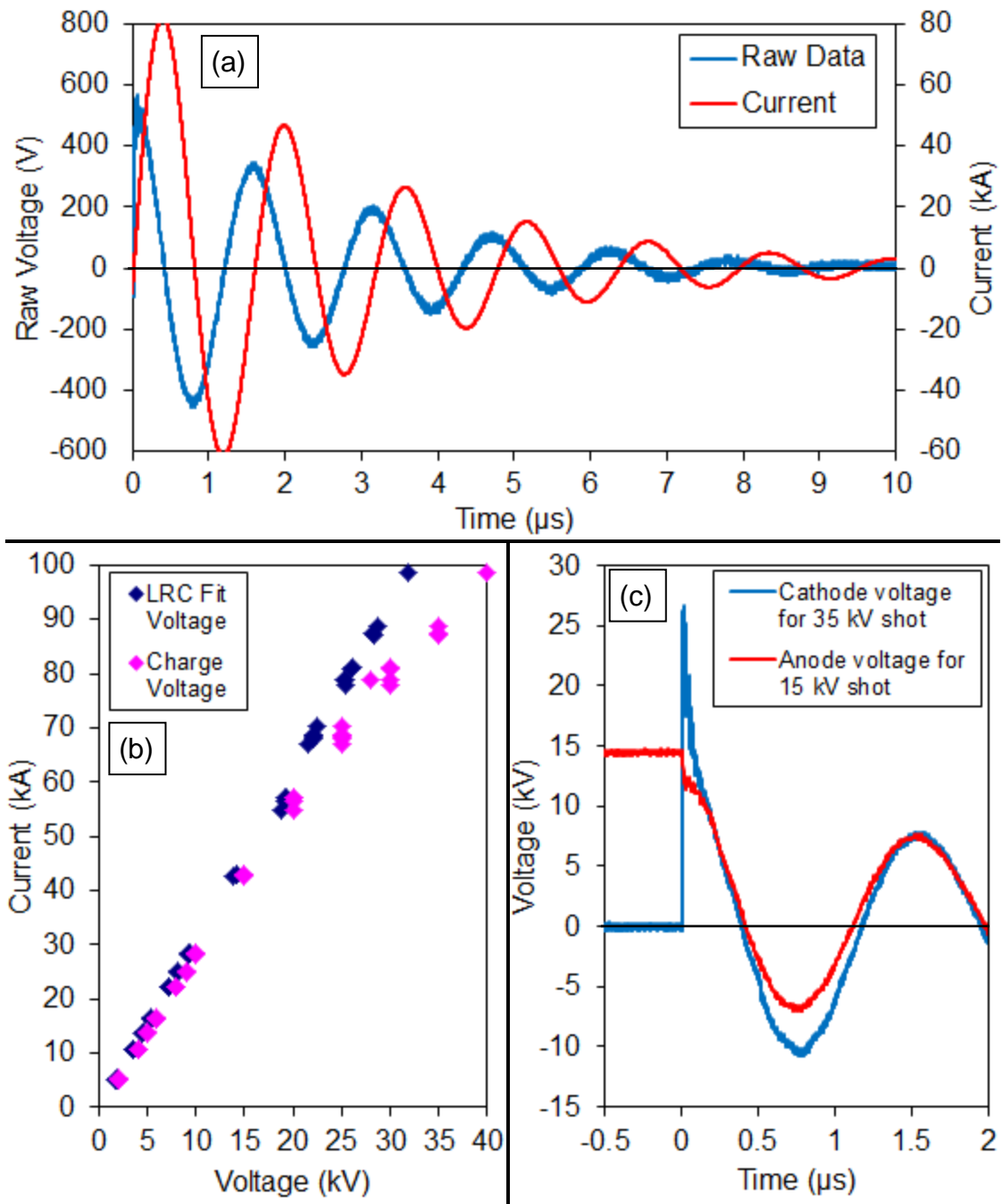
Figure 8.   (a) Plots of measured Rogowski signal and integrated current for a 35 kV discharge. (b) Plot showing disparity between observed charge voltage and peak voltage from LRC curve fit of the current trace. (c) Example plots of measured voltage from the anode and cathode plates of the spark gap showing the disparity described in plot (b).

would differ from the voltage obtained from the LRC curve fit. The values for L, R, and V for the current trace in Figure 8a are 73.3 nH, 51.5 mΩ, and 26.9 kV. In general, L ranges from 70-75 nH and R ranges from 50-60 mΩ.

The next diagnostic needed was a way to measure the magnetic field produced. The simplest way of doing so is using a magnetic pickup coil, also commonly known as a B-dot coil [48]. A schematic view of such a coil is shown in Figure 9. This coil works on the same principle as the Rogowski coil does where the time-varying magnetic field inside the area of the coil induces a voltage in the wire, given by

$$V = n\pi r^2 \frac{dB}{dt}$$
(3.8)

where the coil has n turns and radius r. Once again, since the measurement is the time derivative of the magnetic field, the signal must be integrated. A number of these coils were made throughout the process of this work as they would commonly get damaged. Usually, especially when measuring the field strength in the center of the coils, the B-dot would be made with a diameter of around 1 mm in order to sample a small area. Even with such a small area, the signal measured was tens of volts, so a 2.5x attenuator was used on the connection to the oscilloscope. Also, a small resistor was often used on one of the wires to help damp very high frequency noise.
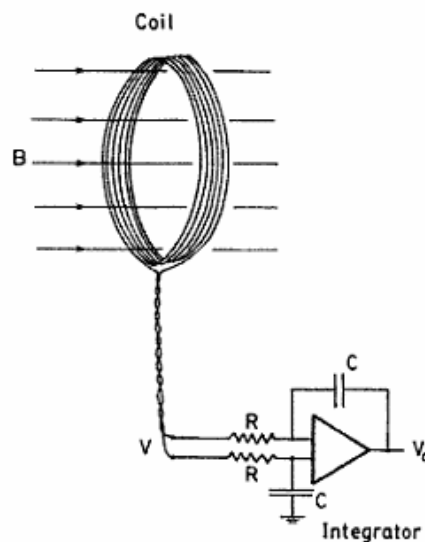
Figure 9.   Schematic view of a B-dot pickup coil with a physical integrator.

26

Calibration of the B-dot was done by constructing a Helmholtz coil which could be used with the pulsed power device. This way, the expected field strength and frequency could be used, which helped gauge the effectiveness of a B-dot under test. The Helmholtz was designed using magnet wire that was 0.014" diameter, with the ends of the wire soldered to plates which would connect to the transmission line. The two loops had one turn each with radius and separation of 0.125". A code was written in Matlab which used the Biot-Savart law to simulate the field produced by coils of varying radius and separation. The expected value of this simulation, given the measured current and coil dimensions, was then used to calibrate the B-dot.

Figure 10a shows a plot of the measured field strength as a function of the measured current. The measured values are compared against the predicted field strength using the simulation mentioned previously for the dimensions of the coils used. The measured and calculated field values agree nicely, although interestingly, a power law fit to the measured values is slightly better than the linear fit. We suspect the reason for this is due to the exploding coils. Above about 40 kA, the coils are destroyed with every shot, and the "violence" of the coil explosion increases with current, as expected. The observation of a slightly decreasing field strength than predicted could be explained by the fact that before the coil is destroyed, the radius of the coil will expand. If this expansion occurs near the peak current, certainly one would expect the measured field to be lower. In fact, at charge voltages of 35 kV, which produce a peak current of about 90 kA, the coil is observed to break just after the peak current is reached. At 30 kV, the coil breaks a few hundred ns later. Figure 10b shows a few representative B-dot traces for different charge voltages, which show how when the coil breaks depends on the charge voltage.
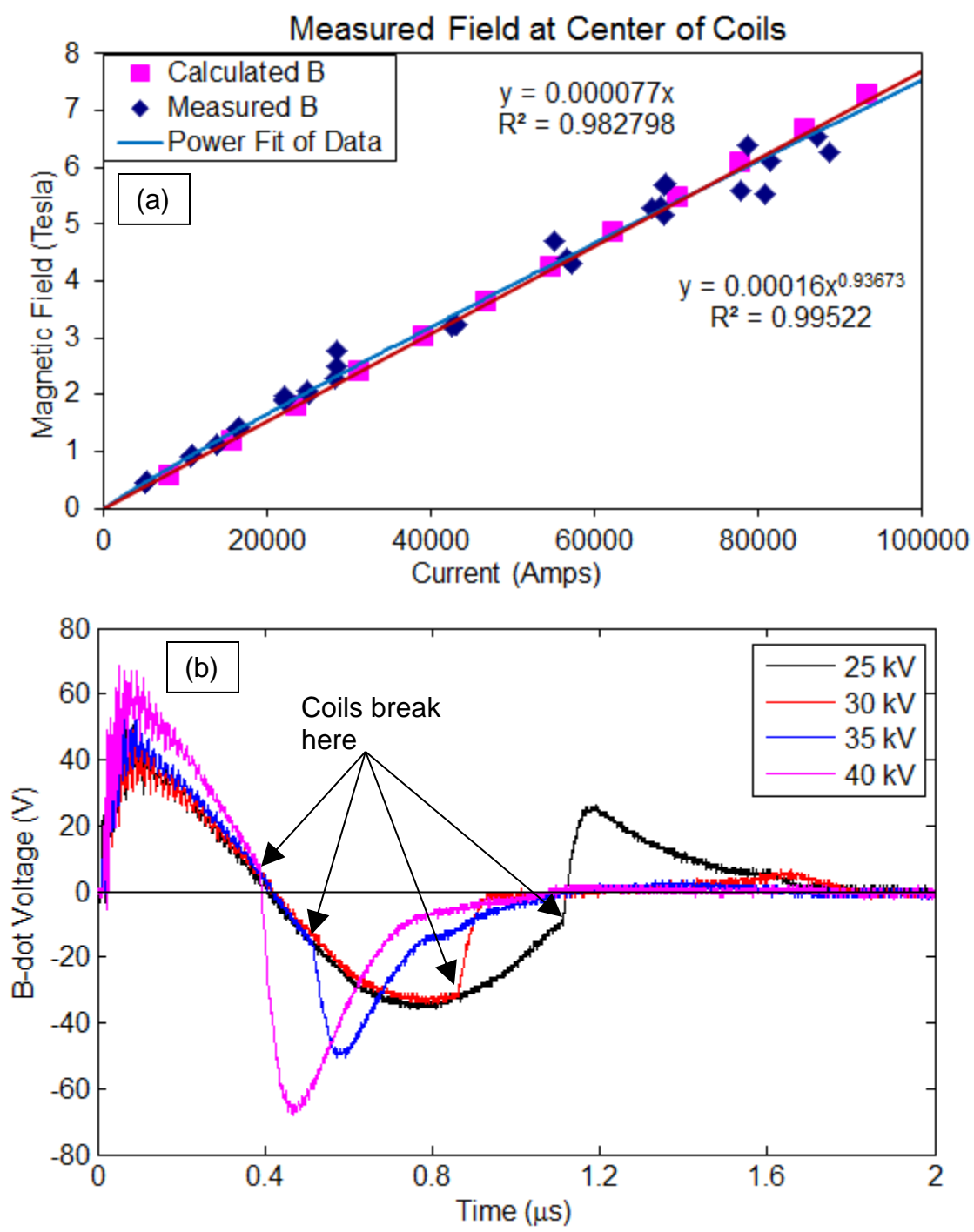
Figure 10.   (a) Plot of measured field in the coils with fits. Also plotted is calculated field for comparison. (b) Plots of raw B-dot signal for different charge voltages, illustrating when the coils break depends on charge voltage.

While B-dot coils could be used at any time, especially during the experiment to confirm the presence of the field, another way of measuring the field produced during the characterization of the device was desired, especially given the self-calibration of the B-dot. The method used was Faraday rotation [49] as measured in a small Terbium-Gallium-Garnet (TGG) crystal. The crystal used had a diameter of 3 mm and was 1 mm thick. A schematic view of the setup for this measurement is shown in Figure 11. A 532 nm laser pointer was sent through a polarizer, and a lens focused the beam so that the sampled area in the TGG crystal was small. A second polarizer was oriented at 45° with respect to the first polarizer, giving maximum sensitivity to changes in the field strength. A second lens was needed to make the beam fit onto the active area of the photodiode. The photodiode had to be positioned far away from the pulsed power device and shielded from EMP noise produced by the discharge of the capacitors.
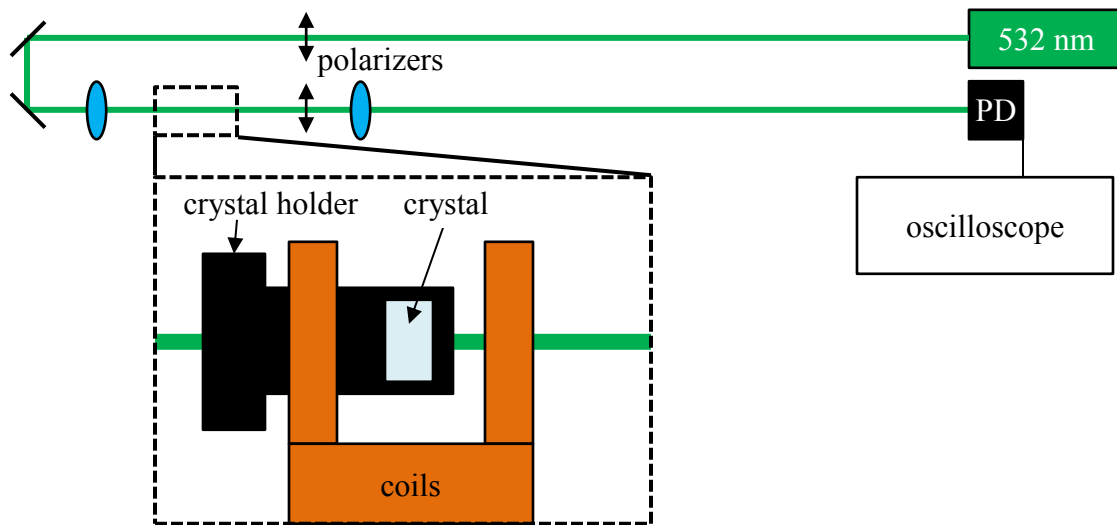
Figure 11.   Schematic layout of setup used for Faraday rotation measurements.

Ultimately, very little data was taken with this setup because above charge voltages of 15 kV, the EMP noise overwhelmed the measured signal. Also, the crystal would get dirty when the coils exploded, and when cleaning the crystal on one occasion, the crystal was dropped and not found. However, the data that was taken did match the measurements using the B-dot probe reasonably well. Figure 12 shows a comparison of Faraday field measurements with similar measurements done using a B-dot. While the B-

dot was generally less than the Faraday, the signal from this measurement was generally cleaner and less noisy, especially since the Faraday signal was less than 100 mV while the B-dot was tens of volts, so it is believed to be somewhat more accurate.
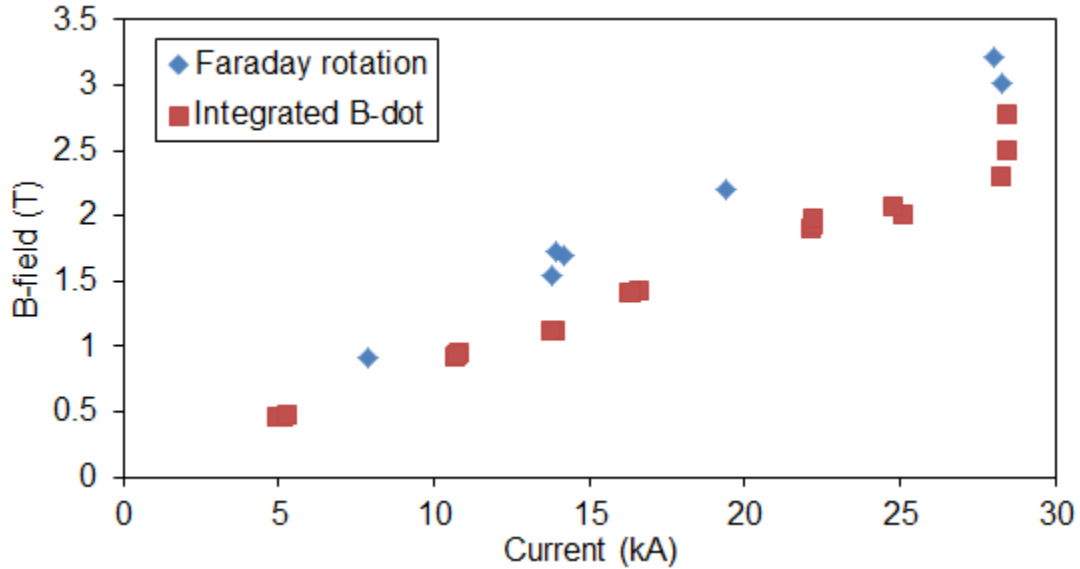
Figure 12.   Comparison of Faraday rotation data with B-dot data.

Finally, we needed to test whether the pulsed power device could deliver the field reliably when the gas jet to be used in experiments was in operation. The testing described above was all done at atmosphere, with no gas jet, so operation was consistent and reliable. However, when tests in vacuum with the gas jet operating were performed, many problems were found. These tests were done in a vacuum chamber which was an experimental chamber for the THOR laser (see Section 3.2.). Initially, the nozzle of the gas jet was oriented parallel to the transmission line, such that the gas was shot at the end of the line, as shown in the picture in Figure 13. It was quickly apparent that the gas jet was affecting the current discharge because the signal from a B-dot monitor (uncalibrated, but used to check for presence of field) was dramatically different when the gas jet fired as opposed to just the field generator discharging on its own. Also, the coil would survive a discharge at a voltage it normally would not survive. An inspection of the end of the transmission line found that arc marks were appearing on the copper coils and the aluminum "ground" of the transmission line, indicating the current flow was

being shorted out and not flowing through the coils. Efforts to prevent this arcing were unsuccessful, so it was hoped that orienting the gas jet to be perpendicular to the transmission line would solve this problem.
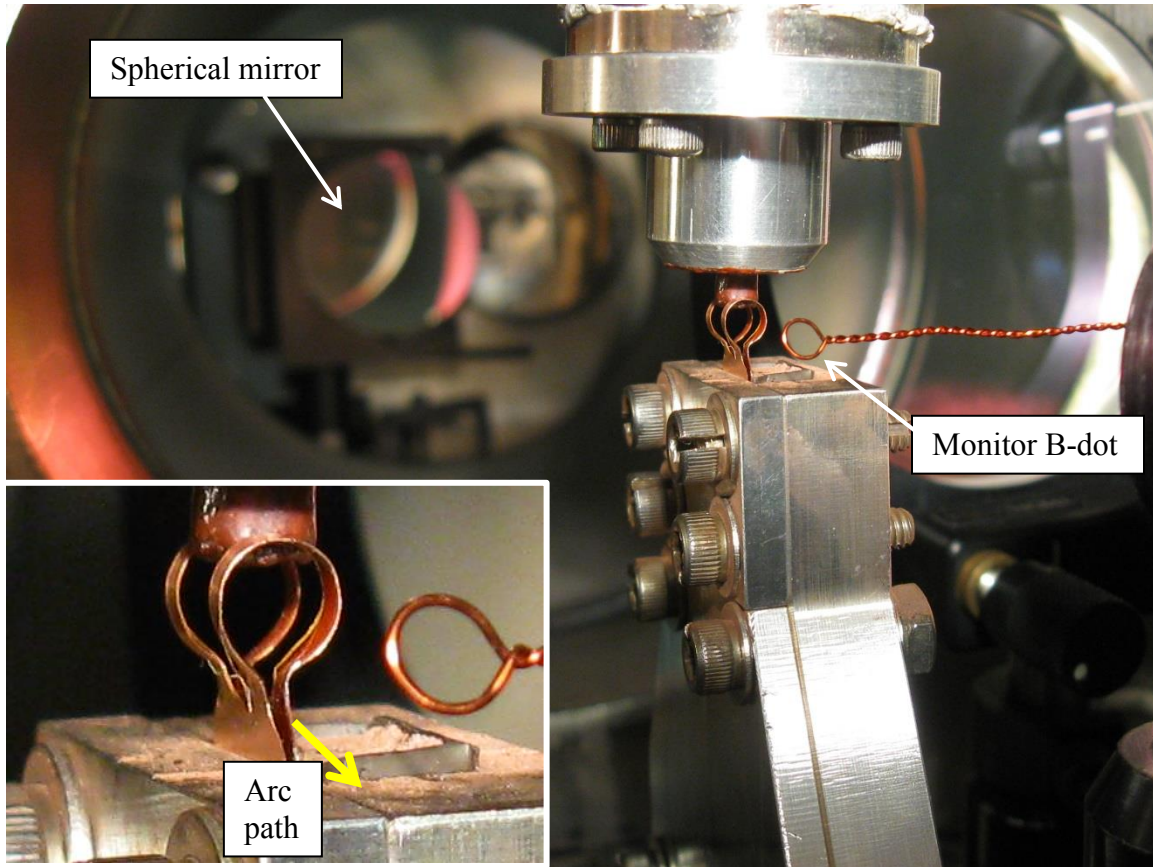
Figure 13.   Image of the first setup which showed the gas jet and pulsed power did not operate well together. The inset shows a magnified image of the coils and the path the arc would take that shorted out the current to the coils.

In order to test this without using laser time, the same chamber was moved to another lab (due to the THOR upgrade discussed in section 3.2). The pulsed power generator was installed perpendicular to the gas jet, and a solid coil was machined out of copper so that the destructible coils wouldn't have to be replaced frequently. The coil used in the following tests was square-shaped, but the interior diameter, coil width, and separation between the coils were the same as the destructible coils. Also, a nozzle made out of delrin was used instead of the aluminum nozzle, which protected the gas jet from

the possibility of arcs. Cameras were set up to monitor the coils from the side, providing a coil-axis view, and the front, showing the end of the transmission line.
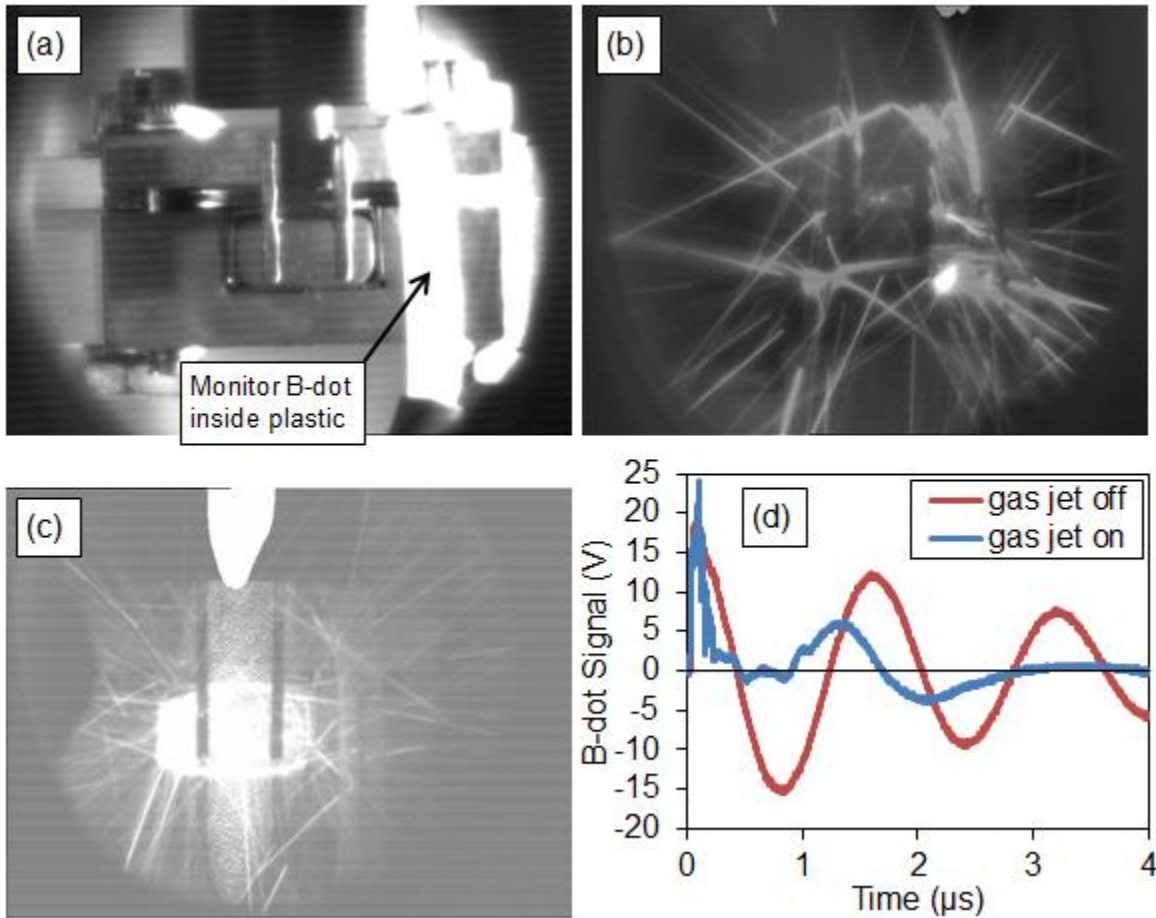
Figure 14.   (a) Reference image of the transmission line and coils. (b) and (c) Sample images showing arcing when gas jet fires with current flow. (d) Sample plot showing the difference in B-dot signal with and without the gas jet on.

Unfortunately, this simple change did not solve the arcing problem. Figure 14 shows some sample images taken of shots with the current discharge and the gas jet operating together, along with a reference picture. Many iterations of trying to improve the existing insulation, from painting on an insulating varnish on the coils and the end of the transmission line to extending the transmission line insulation out into the coils, proved fruitless. Also, the insulation in the transmission line would occasionally fail as a result of the way it had to be installed in the tight spacing between the conductors. In

addition, the end of the transmission line was designed to take the thin, destructible coils, not the solid coils used in these tests. So, it became clear that a redesign of the transmission line and the coils was needed.

3.1.3. Redesign Considerations

As a result of the problems described in the previous section preventing production of the magnetic field reliably when the gas jet is in operation, it became apparent that a more robust design was needed to eliminate arcing problems. The two improvements that were needed were a redesign of the transmission line to allow for a solid insulator between the anode and cathode, and the addition of insulation around the coils. Redesigning the transmission line also required a change in how the line attached to the vacuum feedthrough.

In order to incorporate a solid insulator into the transmission line, it was decided to change the design from the stripline style to a more conventional bi-plate style. This way, a solid insulator could be machined out of plastic (Lexan), and the anode and cathode plates for the current flow could fit into this insulator. However, the spacing between the plates could not be maintained at 0.02" as we worried the plastic would break too easily. As such, we settled on a thickness of 0.062" for the insulator, which seemed like a good compromise between material strength and inductance penalty. Indeed, as will be shown later, the rise time of the pulse was found to increase by about 100 ns because of the increase in inductance from the new transmission line. Figure 15 shows a SolidWorks rendering of the redesigned transmission line and the connection to the vacuum feedthrough. The primary goal of this redesign was to make the possible arcing paths as long as possible in order to defeat the Paschen curve breakdown, especially in areas where the gas jet could affect things. As such, instead of using screws to directly hold together the transmission line, we decided to use clamps around the exterior insulation so that the insulation was as intact as possible.

With the transmission line done, attention was turned to the coils. Various iterations of coil designs were tested, but many would still arc across the coil leads,
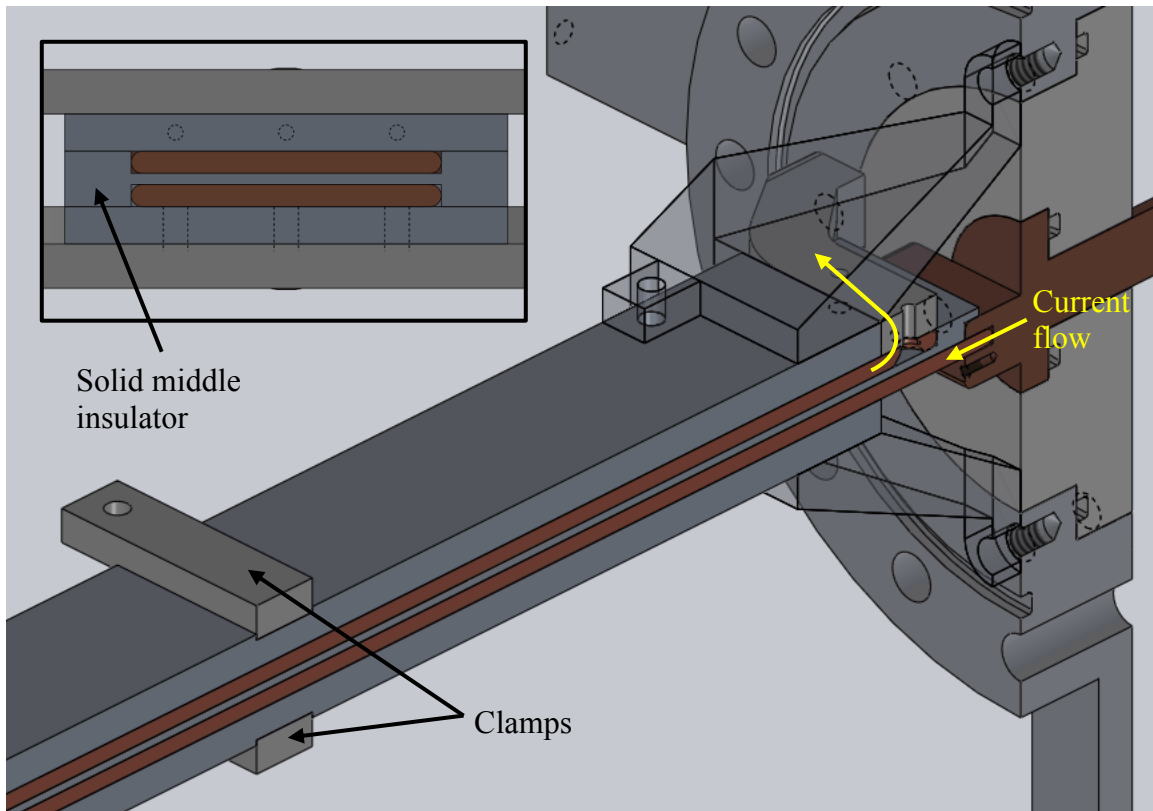
Figure 15.   Cross section views of the redesigned transmission line.

shorting out the current and preventing the magnetic field from forming. Without going into all of the detail of the designs tested, I will present the final design that worked. Figure 16 shows a SolidWorks rendering of this coil design. A feature we added to solve the arcing problem was what we call the "coil shield". Essentially, this is a plastic insulator meant to surround the coils and extend the possible arcing path as much as possible. The shield also had to integrate into the insulation of the transmission line. While this design would still arc on occasion, it was found that using standard silicone vacuum grease to seal the seams between the insulation pieces was the solution to reliably generating the magnetic field in conjunction with the gas jet.

As shown below, the coil shield consists of a central piece which the two individual coils fit into. Then, two additional plastic pieces fit into the recess where the coils are, forming a flush exterior face which helped with the application of the vacuum
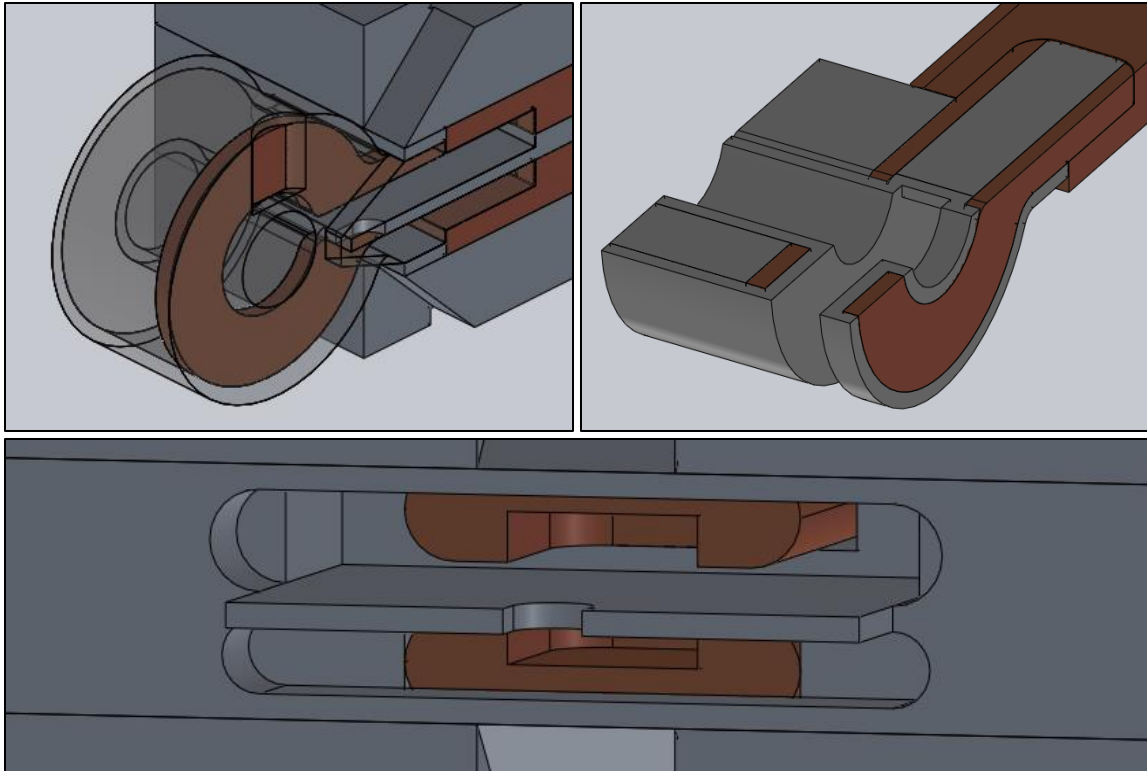
Figure 16.   The top pictures show two views of the coil and coil shield assembly
connected to the transmission line. The bottom picture shows how the coil
assembly fits into the end of the transmission line.

grease. This assembly then slides into the two slots in the end of the center transmission line insulator. Slots are cut into the conductor plates which receive the coils and the center spacer of the shield. Since the electrical contact area is much smaller, the coils essentially become welded to the transmission plates after a number of shots. Additionally, a round recess was cut into the coil shield into which the end of the gas jet nozzle would fit. This was done to allow the coils to be minimally separated axially, which improved the field strength generated. Also, the radius of the coils was increased from about 2 mm to about 3.5 mm in this design.

3.1.4. Testing to Verify Correct Performance

As mentioned in the previous section, many coil/coil shield designs were tested to see if the system could produce magnetic field when the gas jet fired, as would be needed

to perform the experiment. The details of all these tests will not be presented here – only a representative selection of failed tests will be shown, and these will be compared to the tests of the final design, which was found to perform reliably.

First, however, the change in design of the transmission line and the coils caused a change in the discharge characteristics, as noted in the previous section. Figure 17 shows a representative current trace for the old design compared with the new design, as well as a table of the values for the resistance, inductance, and peak current. Using Equations (3.2-4) to estimate the inductance for the new design, we get about 25 nH for the transmission line and about 30 nH for the coils, which gives a total system inductance of about 100 nH, almost exactly matching the measured inductance.

	Old	New
L (nH)	74.7	100.7
R (mΩ)	43.5	46.4
I (kA)	75	67.5
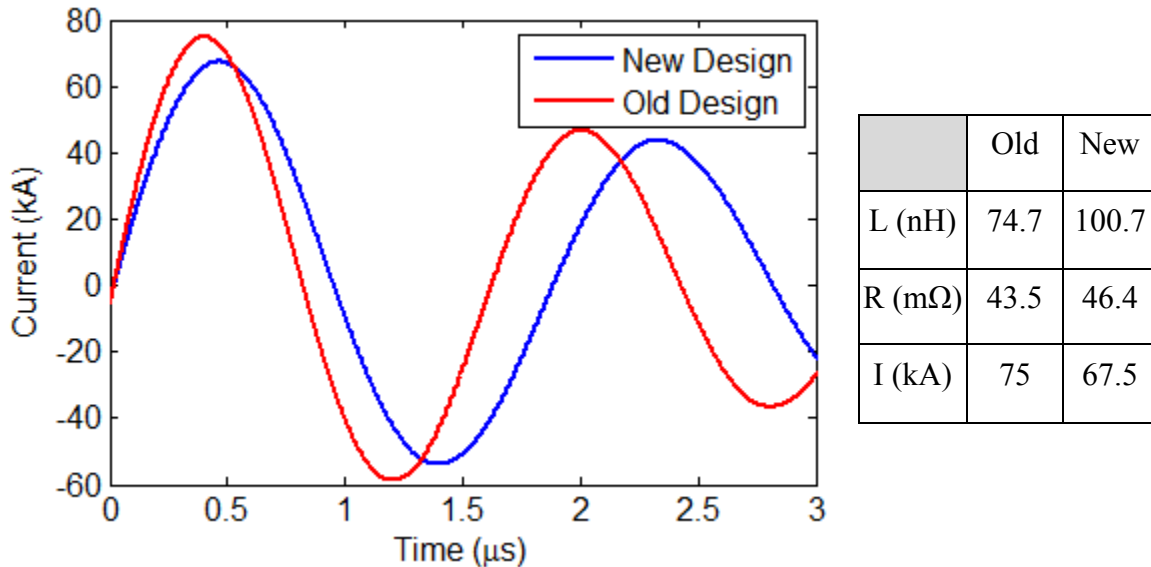
Figure 17.   Comparison of 30 kV discharge characteristics for the old and new designs of the transmission line and coils.

At first, our design of the coils had two forms of insulation that we tried separately. The first was a coil shield similar to what is shown in the previous section but with shorter axial shields extending out away from the nozzle area, and the second was the double coil dipped in a thin ceramic insulation. Both insulation methods failed, but what we observed in testing them proved useful in the final design, which did eventually work. In order to improve our diagnosis of the arcing, a Cordin 220C-8UV gated

36

intensified CCD framing camera was used. This camera has eight separate CCDs which can be independently triggered, and the input light is split using prisms to send the light to each CCD. It also has excellent time resolution, down to as small as 10 ns. The first test on the coils insulated by the ceramic coating showed two clear failure modes. Figure 18 shows a sequence of images using this camera of an axial view of the coils. Looking at the reference image, there is a tab between the coil feeds which is mean to help prevent arcs between them, but from image (d), it is clear the arc finds a way around that. Images (a)-(c) are also interesting since they show an arc propagating from the point of the coils out to the center diameter. This discovery helped inspire the coil shield idea, as it was clear more insulation around the inside of the coils was needed.
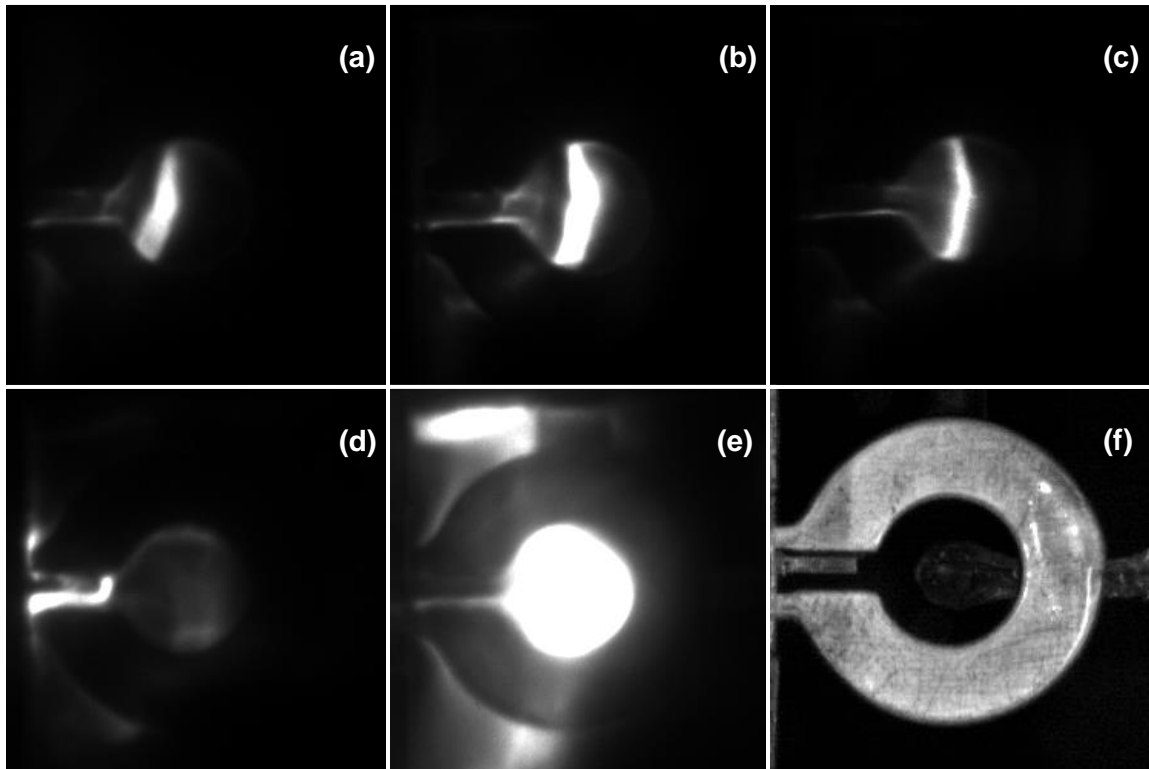
Figure 18.   Images from framing camera showing arcs at various times during current discharge. Each frame is 100 ns long starting at time (a) 200 ns, (b) 300 ns, (c) 400 ns, (d) 800 ns, and (e) 1400 ns after the discharge started. (f) is a reference image of the coated coil.

Figure 19 shows a SolidWorks rendering of the first coil shield design we used. As noted, the inner diameter of the coils is now insulated to prevent the arc shown above. However, while this improvement did suppress that arc, there was still an arcing path that was available to be exploited. The exposed end of the coil contact, indicated by the yellow circle, was able to arc around the tab extending out from the end of the transmission line and reach the other exposed coil contact. Figure 19 also shows a sample image where this arcing can be seen, although not directly. The bright light seen does seem to indicate that this arc is happening. Images looking at the front view show just a bright area between the coils in the area where this arc would be expected to be. The result of this testing led to the design shown in the previous section, where the minimum arcing path was over 1.5 cm.
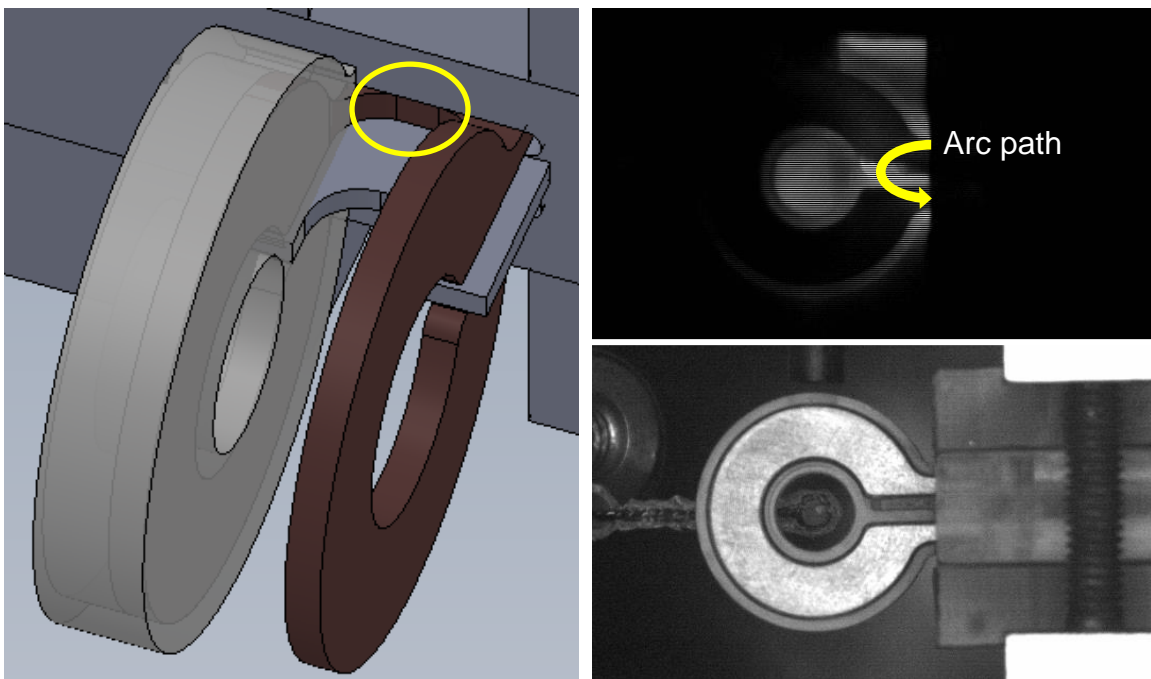
Figure 19.   Images showing the first coil shield design. While some arcing was suppressed, there were still failures, as indicated in the top right image.

Even with the increased minimum arcing distance, failure of the production of the magnetic field still happened when the gas jet was used. However, if we consider the

inductive voltage across the coil feeds, this is not as surprising. Using the equation for the voltage induced by an inductor,

$$V = L\frac{dI}{dt}$$ (3.9)

we have the values L = 30 nH and $dI/dt \approx 70\ kA/500\ ns$, which results in a voltage across the coils of about 4,000 volts. At atmosphere, using a value for $p \times d$ of ~1000 Torr-cm, this is below the breakdown voltage predicted by a Paschen curve for Argon [50]. Also, at a vacuum level of 10^{-4} Torr (pd of .00015 Torr-cm, or 2 x 10^{-6} bar-mm), this is once again below the breakdown voltage [51]. When the gas jet fires, though, the ambient pressure in the region can easily jump to tens or hundreds of millitorr, shifting the point of interest on the Paschen curve to a position much closer to the minimum, and hence to breakdown voltages that are lower than the induced voltage, causing the arcs.

As a last effort to try and prevent this arcing problem, we hoped that using standard silicone vacuum grease could be used to seal the seams and gaps between the insulating pieces, thus blocking the remaining paths where arcs could form. As it turned out, this did work at stopping the arcs, as shown in Figure 20. An image with the arc is compared to an image without any arcs, and the corresponding B-dot signals are shown. While the image without the arc does still have a lot of light, we suspect that this could be due to an induced electric field caused by the time-varying magnetic field, as given by Faraday's law,

$$\nabla \times E = -\frac{dB}{dt}$$ (3.10)

or in integral form,

$$\oint_L E \cdot dl = -\frac{d}{dt}\oint_A B \cdot da$$ (3.11)

for a surface A with boundary L. If we take a circular loop of radius 1 cm which is concentric with the coils, the average field strength through the surface will rise from 0 to ~1 T in 500 ns. Using Equation (3.11), the electric field along the boundary of the surface (outside of the coils in the area where the light is seen in Figure 20) induced by the magnetic field is about 10 kV/m. Looking at the plot comparing the discharges, the B-dot

39

signals seemed to show little difference, but the cleaner signal from the right image discharge implied the situation was improved. Also, the noise is thought to be electrostatic in nature, and indeed, a B-dot design which can compensate for electrostatic noise [52] showed a cleaner signal when the gas jet was used during the experiments described in Chapter 6.
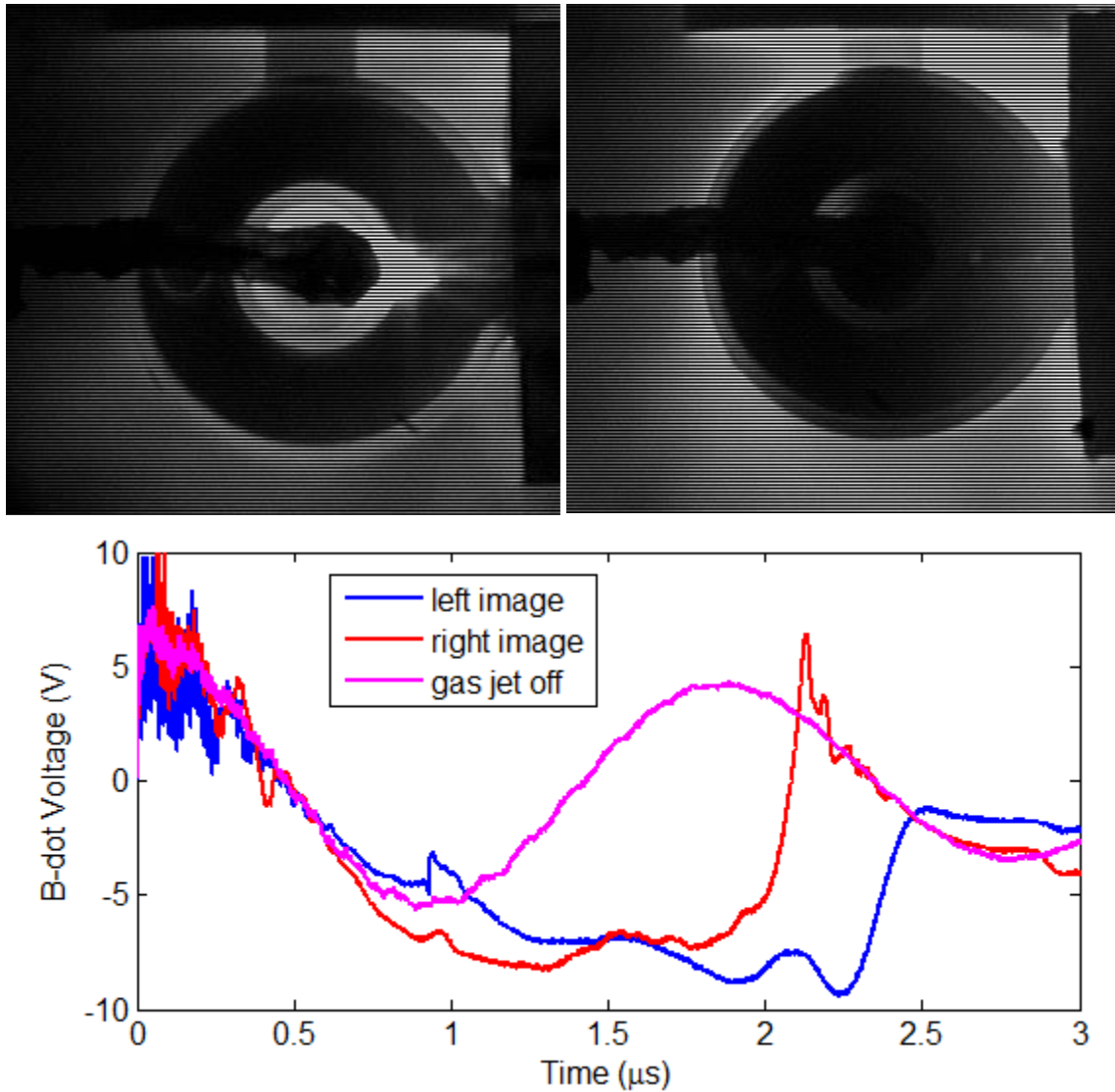
Figure 20.   Before (left) and after (right) the application of vacuum grease. The lack of light in the coil center and near the coil feeds suggests the arcs are gone.

40

3.2. **UPGRADE OF MULTIPASS TI:SA AMPLIFIERS ON THE THOR LASER**

During the course of this work, a project to upgrade the Texas High-Intensity Optical Research (THOR) Laser was undertaken. Part of the upgrade consisted of redesigning the two multipass Ti:Sapphire amplification stages to make the 10 Hz operation of the laser more energetic. The design and performance of this upgrade will now be presented.

3.2.1. Design Considerations

The main goal, as stated, was to extract more energy from the two amplifiers. This was possible because both amplifiers would be pumped with more energy. The original design was as follows. The first amplifier, a 4-pass bowtie, was pumped with the remaining energy of the Big Sky CFR-400 Nd:YAG laser which was not used in the regenerative amplifier. Typically, this was about 130 mJ. The second amplifier, a 5-pass bowtie, was pumped by two Spectra-Physics PRO-350 Nd:YAG lasers which provided about 1.2-1.3 J each. As part of the upgrade, the regenerative amplifier was to be replaced with two OPCPA stages pumped by a Continuum PowerLight 9000 seeded Nd:YAG laser. As such, the full energy of the Big Sky was now available to pump the 4-pass, which is 200 mJ at 532 nm. In addition, since the OPCPA only uses a small amount of the pump energy, it was decided to use the remainder of the Continuum beam to pump the 5-pass, in addition to the two PRO-350 lasers. The Continuum provides about 1 J of light at 532 nm, and it was thought that it could provide as much as 900 mJ to the 5-pass crystal, resulting in about 3.5 J of total pump energy.

With these numbers in mind, pump beam sizes can be determined for the amplifiers. Typically, pump fluences of about 3 J/cm^2 are used on Ti:Sa, so this will be the target. For the Big Sky, it is a bit more involved since a Brewster-cut crystal is used in the 4-pass. The Brewster angle for Ti:Sa, using the refractive index of 1.76, is 60.4°, and so the equation to solve is

$$3 = 0.2/(\pi r^2/(2\cos 60.4)) \tag{3.12}$$

This gives a radius ($1/e^2$) of 1.5 mm, which would normally be much too hot, but since the beam is "smeared" out on the crystal face because of the Brewster angle, the fluence desired is achieved. For the 5-pass, the crystal is at normal incidence, so we simply find the radius needed for a 3 J/cm^2 fluence. This turns out to be 6 mm at $1/e^2$ radius.

In order to model the amplification expected from these amplifiers, I wrote a code in Matlab using the concept of excited atom accounting [53,54]. The pump beam spatial profile is taken as an array with a cell size Δx (assuming a square cell – rectangular cells may be used as well), with the fluence of each cell given by the energy within the cell divided by its area. The pump beam incident on a crystal of length L will then create an excited atom density

$$n_0 = \frac{F_{pump}}{L} \frac{1}{h\nu_{532}} \tag{3.13}$$

in each cell, where F_{pump} is the pump fluence in the cell, and $h\nu_{532}$ is the energy of 532 nm photons. The pump beam is assumed to create a uniform density through the crystal which, while not realistic, is good enough for the purpose of this modeling. The seed beam is similarly modeled as an array of the same cell size. However, the temporal shape of the pulse is added to this, making a 3D array. The stretched pulse of THOR (and the upgrade) is about 600 ps FWHM, so this is folded into the array. This way we can predict how much red-shift of the pulse will occur. The reason for this red-shift is due to the stretching process, described briefly in Section 4.1. Since the longer wavelengths of the pulse precede the shorter wavelengths, the longer wavelengths will experience a slightly higher gain than the shorter wavelengths. This will cause the peak wavelength to shift, from 800 nm to maybe 805 nm, as an example.

With each time slice of the seed beam, the gain is calculated using the small signal gain formula

$$G_0 = e^{n_0 \sigma L} \tag{3.14}$$

where σ is the stimulated emission cross section for Ti:Sa, 2.8×10^{19} cm^2. This is valid because the fluence of each cell in each time slice of the seed pulse is much less than the

saturation fluence. After the slice of the pulse has been amplified, the energy extracted is calculated, and the excited atom density is reduced using

$$n_{0,new} = n_{0,old} - \frac{\Delta E}{h\nu_{800}\Delta x^2 L}$$

(3.15)

This illustrates the reason why the seed beam will be red-shifted. This process is repeated for each time slice of the seed pulse, and then with each pass through the crystal. Using this code, not only can analytical spatial profiles be modeled, but images of the seed and pump beams can be used. When using images, knowledge of the pixel spatial resolution and beam energy are required to generate the fluence map of the beams. Additional factors of excited atom density loss through fluorescence, percentage of pump beam absorption, and seed energy loss per pass can be included if desired.

First, we will use this model to analyze the 4-pass amplifier. In this case, using a rectangular cell size is useful due to the Brewster angle of the crystal. This will give cells of size $(\Delta x, \Delta x / \cos 60.4°)$. The input seed energy from the OPCPA stages is expected to be at least 1 mJ with a beam size similar to that of the 4 pass pump beam, about 3 mm diameter. The crystal has an optical path length of 1 cm. After amplification, the seed beam is predicted to reach about 43 mJ. A plot of the gain per pass, as well as the energy after each pass, is shown in Figure 21.

Next, for the 5-pass, we will use the output of the 4-pass as the input (minus some transmission losses). The beam size will be near the pump beam size, however the final input seed size will not be finalized until the amplifier is built. This is because the significant pump energy in the crystal creates a thermal lens [55]. This results from the refractive index of Ti:Sa having a positive temperature dependence. Since the crystal is in a water cooled mount, the outer radius will be cooler than the center, and so the effective refractive index in the center is higher, resulting in the crystal acting as a positive lens. As such, the input beam will be made so that it is diverging, and after all five passes, the output beam will be collimated. For the purposes of this estimate, using a collimated beam will give a decent idea of what amplified energy we can expect. The crystal length is 1.47 cm, the pumped region spatial profile is roughly fourth order super-Gaussian with
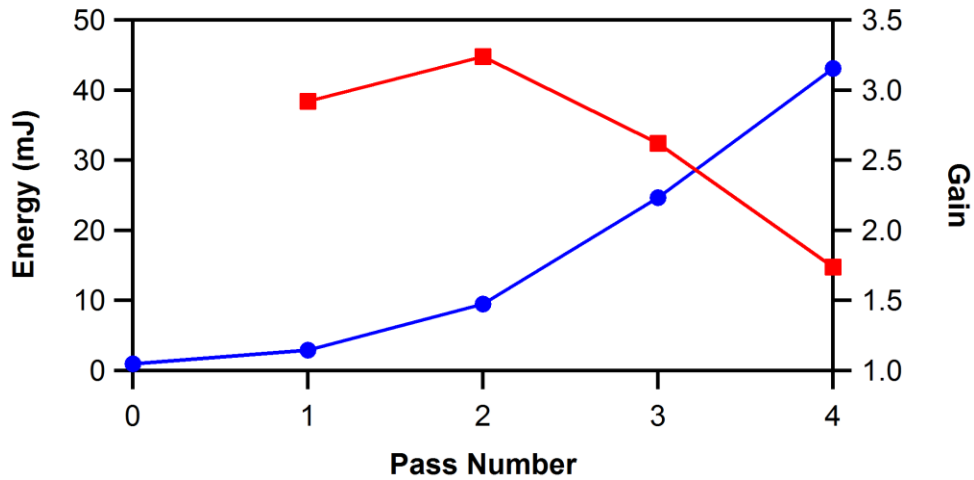
Figure 21.   Plot of simulated energy per pass (blue) and gain per pass (red) for the 4-
            pass amplifier.

$1/e^2$ radius of 6 mm, and the seed beam spatial profile is Gaussian. Assuming the input seed energy is about 30 mJ, the output energy is expected to be near 1.8 J. The gain and pulse energy per pass, as well as the amplified seed pulse, are shown in Figure 22. While the input seed is Gaussian in shape, the output beam takes on the spatial profile of the pumped region, or equivalently, the spatial profile of the pump beams. Also, the amplification strongly saturates after the third pass, indicating that the output energy should be quite stable over a range of input seed energies.
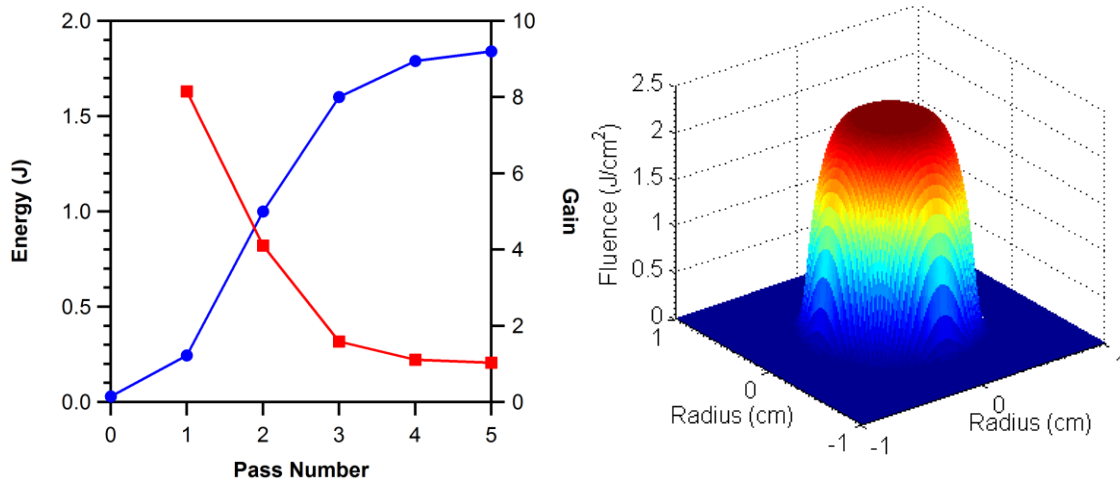
Figure 22.   Simulated gain (red) and energy (blue) per pass, as well as the output spatial
            profile.

44

With the energetics modeled, the physical layout for the system had to be designed. The layout of the two bowtie amplifiers was essentially the same, so the telescopes/spatial filters that routed and resized the beams, both pump and seed, required the most work. An important part of this work was to improve the imaging of the pump beams used for the 5-pass as this would impact the spatial profile of the amplified beam, as mentioned above. The final design for the whole system is shown in Figure 23.
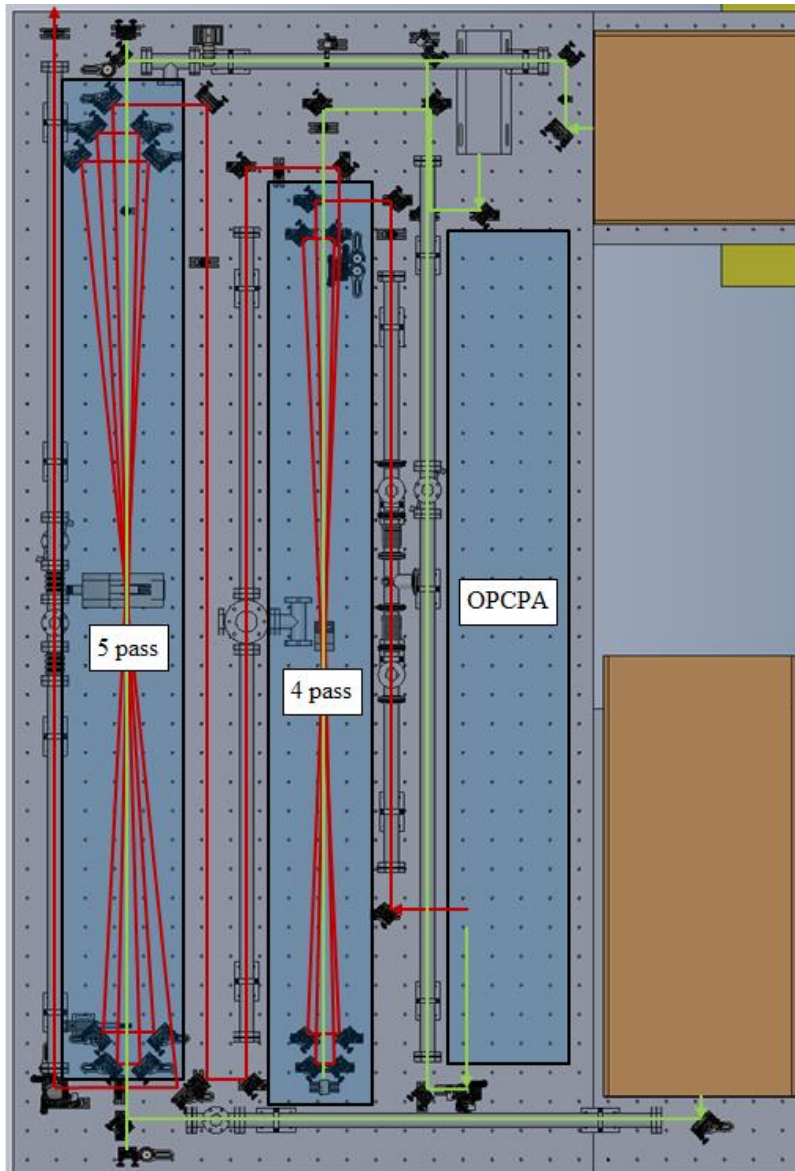
Figure 23.   SolidWork layout of redesigned 4-pass and 5-pass amplifiers. Pump beams are in green while the seed beam path is red.

The seed beam comes from the OPCPA section near the bottom of Figure 23. It passes through a slightly magnifying telescope with a spatial filter at the focal plane. After passing through the 4-pass, the beam is periscoped up and sent through another telescope/spatial filter combination. In order to image the beam from the last pass of the 4-pass to the first pass of the 5-pass and magnify the beam by about 5x, the telescope had to be folded. As mentioned before, the final position of the second lens of this telescope will be determined experimentally. Finally, after going through the 5-pass, the beam is sent through one more telescope/spatial filter combination. This telescope is does not magnify the beam, and the last pass of the 5-pass is imaged to a point in space in the target room. The reason for this is that the THOR upgrade will have two modes of operation, and the diverging point for the two beam paths begins at the image plane of this last telescope. One beam path magnifies the beam by a factor of five to send it into the 10 Hz compressor chamber, while the other beam path sends the beam to a final power amplifier for higher energy/lower rep-rate operation. The pump beam for the 4-pass is simply resized using a 1m lens since the beam is Gaussian. The residual pump beam from the OPCPA is imaged from the second stage crystals onto the 5-pass crystal using a telescope with magnification of just over two. Finally, both pump beams from the PRO-350 lasers are imaged from the doubling crystal inside the laser head onto the 5-pass crystal with only slight magnification.

3.2.2. Performance Results

The first task was to size the pump beam on the 4-pass crystal and image the seed beam from the OPCPA to the crystal. The spatial filter which transports the seed beam has a 75 cm focal length (FL) lens and a 90 cm FL lens, which slightly enlarges the beam. At the focal plane of the 75 cm lens is a pinhole with a diameter of 400 μm. An image of the beam after the spatial filter is shown in Figure 24. The output energy of the OPCPA stages was as high as 10 mJ with saturation, but in the initial stages of setting up this amplifier, the seed energy was often less than 1 mJ. Next, the pump beam from the Big Sky had to be aligned and sized onto the crystal. It was discovered that the beam

emerging from the laser was noticeably divergent, although it seemed to match the specification of 2.5 mrad divergence. As such, using a 1 m FL lens to demagnify the beam (which was about the shortest focal length that could be used given the length of the bowtie) did not quite make the beam fit the design specification of 2 mm $1/e^2$ diameter. This resulted in the pump fluence in the crystal being just under 2 J/cm^2. An image of the pump beam just after the 4-pass crystal is also shown in Figure 24. The image of the beam was taken after it had passed through the crystal, which may account for the somewhat spiky nature of the spatial profile.
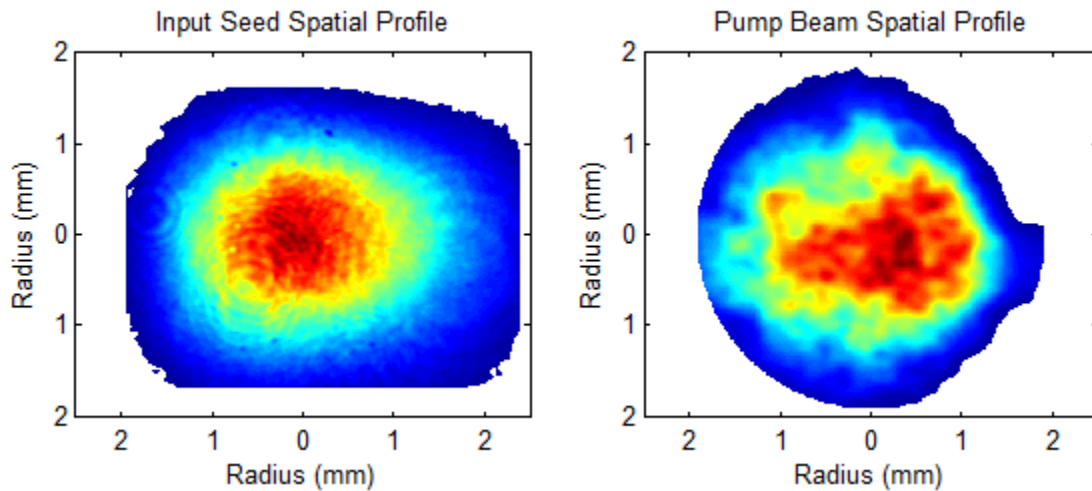
Figure 24.   Images of the seed beam (left) and pump beam (right) in the 4 pass.

Since the pump beam's fluence was lower than planned, we wanted to see how this would affect the amplification. Using the amplification code and the images of the seed and pump beams above, the performance of the amplifier was evaluated. For the range of input seed energies at the time (300 μJ to 1 mJ), the model predicted amplified energies ranging from 6.5 mJ up to 24 mJ. This was found to be a bit too low to seed the 5 pass, so it was decided to add two more amplification passes to this stage, making it a 6 pass. With this addition, the predicted output energies ranged from 28 mJ up to 54 mJ. With the saturated OPA seed energy input (7-8 mJ after the spatial filter), the energy was predicted to be near 80 mJ. Clearly, strong saturation in this stage is not achieved, but with the addition of the two passes, the scatter in the seed energy is expected to be

reduced from a factor of five or more down to a factor of two or less. Also, this input seed energy range is high enough that the output of the 5 pass will be more stable.

The alignment and optimization of the amplifier was done in the following way. First, the seed beam was roughly aligned through all six passes without the pump beam running. Then, to remove a variable from the process, a pair of irises was used to level the beam so that it was in a plane parallel to the table. Since the crystal was mounted to transmit S-polarized light, each iris was a different height. The pump beam was aligned such that it was in this plane as well. Now, all that needed to be done was to optimize the horizontal position so that maximal gain was extracted with each pass. For each pass, a mirror was inserted which took the beam out of the amplifier and sent it to a camera. While watching the beam on the monitor, the steering mirror which sent the beam through the crystal was adjusted to achieve peak brightness (with the pump beam running, obviously). Images were saved, and then an energy meter measured the energy. Figure 25 shows the amplified beam after the six passes, as well as a comparison of the
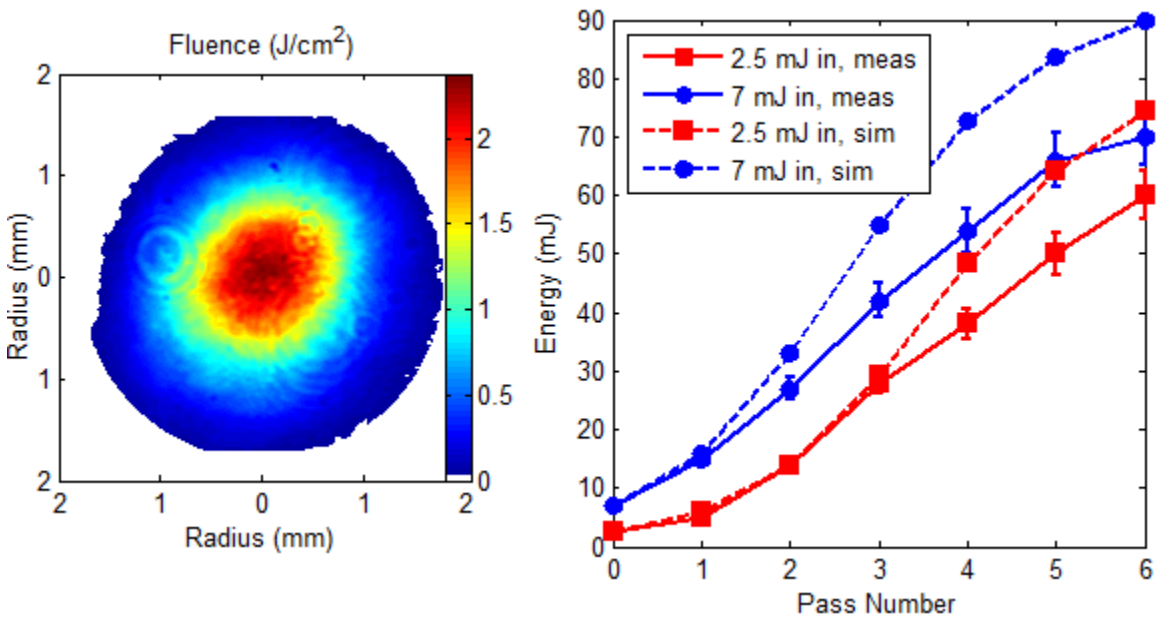
Figure 25.   Amplified 6 pass spatial profile with fluence in J/cm^2 (left) and comparison of measured energy per pass for two input energies with the simulation (right). Error bars on measured energy represent a ±7% spread in the energy as seen on the energy meter.

48

measured energy per pass with the simulation prediction. The peak fluence of the seed beam is over 2 J/cm^2, which is a result of the amplifier crystal set at Brewster's angle, and the spatial profile is Gaussian with a $1/e^2$ diameter of about 2.5 mm. The measured energies do not quite agree with the simulation, although the fact that the seed beam size coming out is somewhat smaller than the pumped region could help explain this. In any case, 60 mJ is plenty to seed the 5 pass, so this less-than-optimal performance will not hurt us.

With the 6 pass completed, the next thing to do was to image the three pump beams onto the 5 pass crystal. The two PRO350 lasers are each imaged onto the crystal using a telescope with a 75 cm FL lens and a 90 cm FL lens, leading to a slight magnification of each beam. As stated before, each telescope was designed to take the beam image from near the doubling crystal in the laser head and put that onto the 5 pass crystal. In order to image these beams at the 5 pass crystal, a HR mirror was used to divert most of the beam into a power meter, with the leakthrough allowed to pass through the mirror. Then a wedge was used to send a small reflection to a camera. The camera was set up to image the beam at a point that would be equivalent to the crystal plane. Each PRO350 delivered about 1.2 J onto the crystal.

The leftover pump beam from the OPCPA also had to be imaged onto the crystal. Here, the input image plane was set to be near the second stage crystals of the OPCPA. The telescope used a 1 m FL lens and a 2 m FL lens, giving a magnification of two. It was discovered, however, that the energy delivered to the crystal was much less than expected, about 500 mJ. By inspecting the energy at a number of points throughout the OPA, we found that the transmission losses were higher than our intuition expected, although most were within the specifications of the optic. The dichroic mirrors which transmitted the pump beam and reflected the seed beam around the OPA crystals were found to be especially lossy, losing about 10-11% from each mirror. As such, the total energy in the 5 pass crystal was about 2.9 J. Figure 26 shows images of the three pump beams at the crystal, as well as a sum of the beams showing the pump fluence in the crystal. The individual beam profiles are not especially great, but the summed profile

generally looks pretty uniform with a large area having the desired 3 J/cm^2 fluence. Fits to the spatial profile of the combined beams give a fifth order Gaussian along a horizontal lineout, but only a second order Gaussian along a vertical lineout. Both lineouts give a 1/e^2 radius of about 6.5 mm.
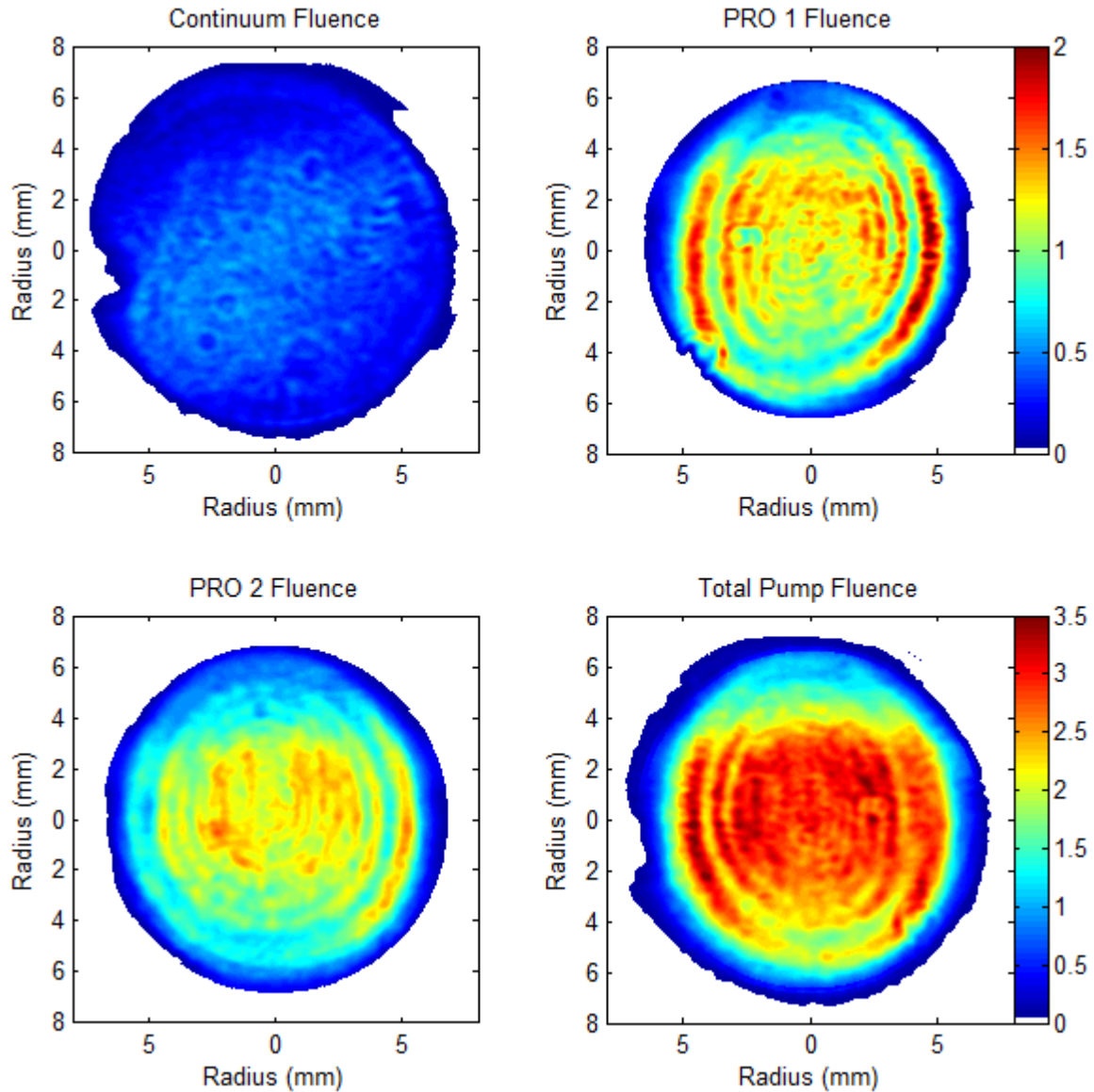
Figure 26.   Images of the three pump beams on the 5 pass crystal, plus a sum of the beams showing the total fluence in the crystal. The three individual beam images use the top color bar, while the sum image uses the bottom one. Fluences for all plots are in J/cm^2.

The spatial filter for the seed beam after the 6 pass uses a 30 cm FL lens and a 1.25m FL lens, with a 200 μm pinhole at the focal plane of the 30 cm lens. As mentioned previously, the second lens is less than 1.25 m from the focal plane so that the beam is diverging coming out of the telescope. The final position of this lens such that the beam emerging from the 5 pass was roughly collimated was found to be 38" from the focal plane of the first lens. Figure 27 shows plots of measured data in comparison with simulations for the same input energy. The measurements were taken using a pick off mirror, which sent the beam to a power meter. A wedge before the power meter reflected some light to another wedge, which was sent to a camera, enabling simultaneous energy and image data to be taken. While this setup was useful, it was found the losses from the first wedge were 15-20% (this has been accounted for in the data plotted). First, it is clear the simulated output energy is lower than what was predicted above, but this is primarily a result of the reduced pump energy. In addition, the measured energy is definitely less than what is predicted. One thing to check would be that the seed beam after the later passes was the correct size, i.e. near the size of the pumped region. Using the simulation, the beam profile can be predicted using the images of the pump beams and the seed beam
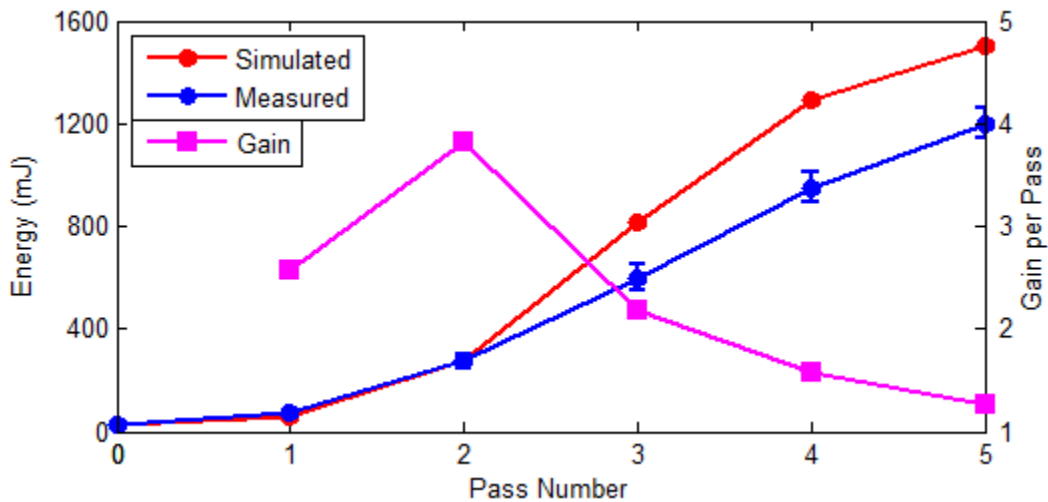
Figure 27.   Plot of measured data (blue) for amplification in the 5 pass along with the simulation result (red) for comparison. The measured gain per pass is shown by the magenta squares. The error bars range from 5-10% to represent the range of energies seen on the power meter. The gain from pass 1 is low because PRO2 is delayed to arrive after the first pass of the seed.

51

(assuming no thermal lensing), and this can be compared to the measured beam. Figure 28 shows the simulated and measured beam profiles after the 5 pass, along with a horizontal lineout of each beam. While the vertical cross-section is apparently different, the horizontal lineouts do agree quite well, which seems to indicates the beam has the correct divergence and size into the amplifier. If this is all correct, then our source of energy loss lies somewhere else.
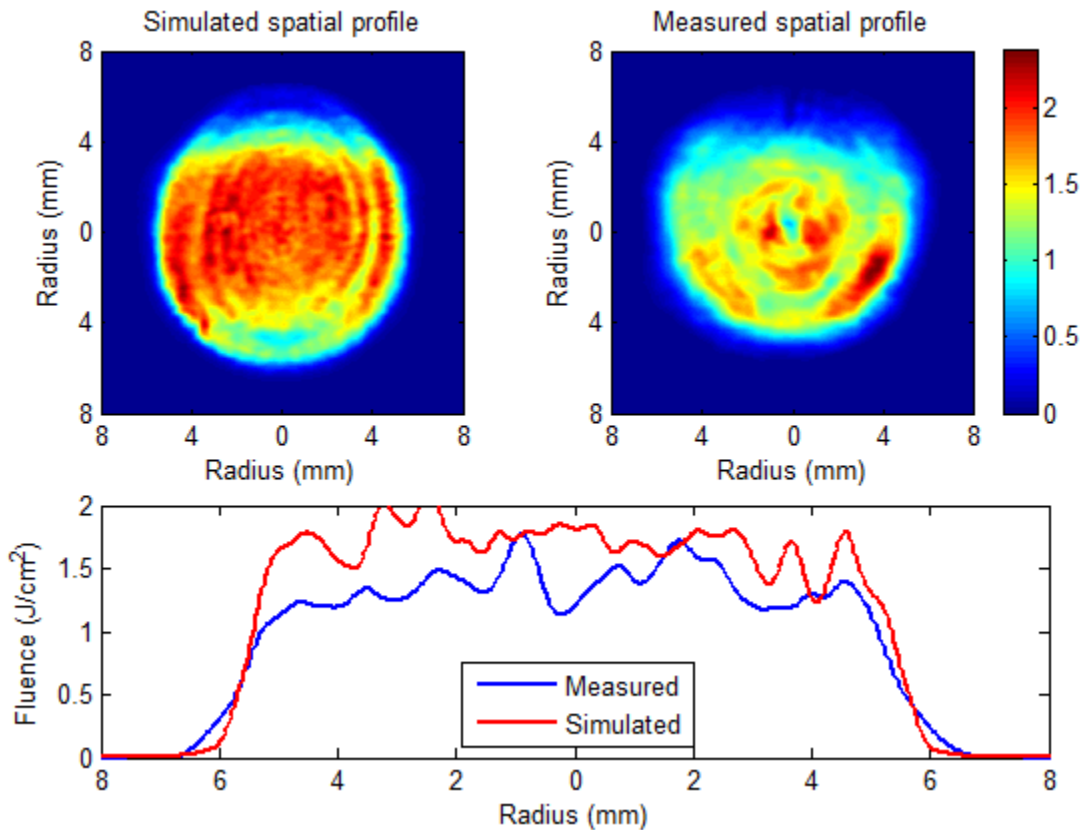
Figure 28.   Image of the amplified beam after the first and last pass of amplification, along with horizontal lineouts showing the width of the beams.

Because of the high pump fluence and large gain area in this crystal, there can be cause for concern about parasitic lasing [56]. Essentially, spontaneously emitted light in the crystal can bounce back and forth inside the crystal and experience gain, which therefore depletes the excited atom density in the pumped region, and results in lower gain in the amplifier. Steps can be taken to inhibit this parasitic lasing, such as having the

52

barrel of the crystal rough-ground to scatter light reflecting from that surface, and having something on the crystal to absorb that light. In our case, our crystal is rough-ground, and we have used a black Sharpie marker to paint the barrel, which acts to absorb that light. On the original THOR laser, this was found to be sufficient to suppress any parasitic lasing [57]. However, using a photodiode to look at the fluorescence of the crystal when it was being pumped by all three lasers, there did appear to be parasitic lasing occurring. When all three pump lasers were incident on the crystal, a spike with amplitude on the order of the fluorescence of one pump laser appeared, as shown in Figure 29. Interestingly, when the Continuum laser was blocked, and just the two PRO lasers were pumping the crystal, the presence of this spike was not observed. The absorption coefficient of the current 5 pass crystal is $\alpha = 2.6$ cm^{-1}, which leads to strong absorption near the surface of the crystal. We believe that since PRO2 and the Continuum are incident on the same side of the crystal, the additional gain provided by the Continuum allows parasitic lasing to occur near that surface. One solution to this problem is optimizing the timing of the pump lasers with respect to the seed so that the threshold
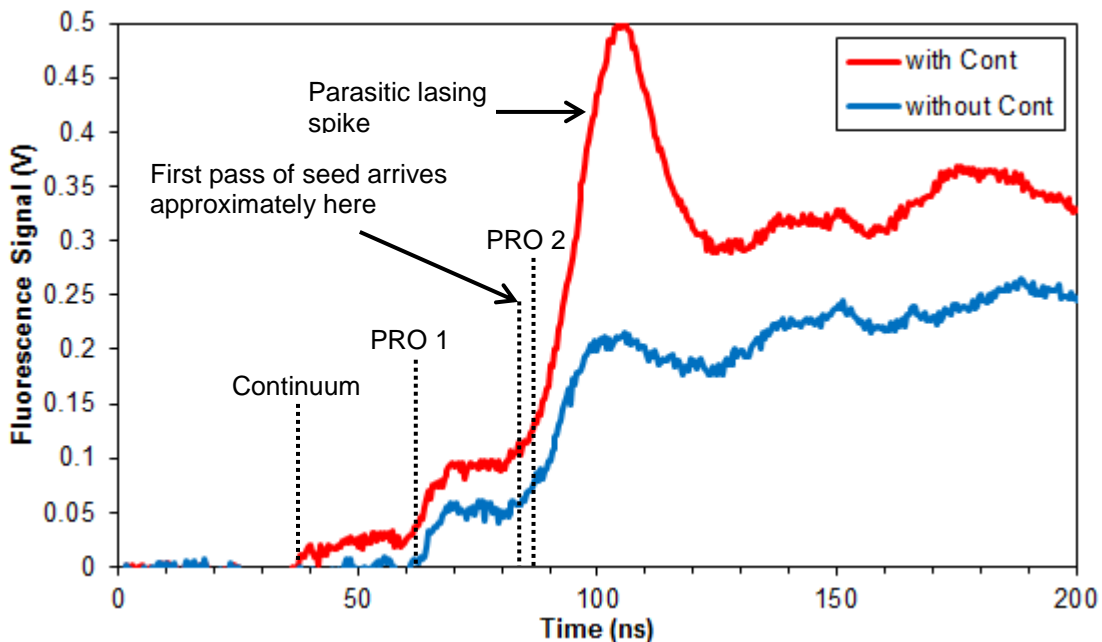
Figure 29. Plot of fluorescence signal from 5 pass crystal pumped by the two PRO 350 lasers (blue) and all three lasers (red). The large spike on top of the fluorescence signal indicates parasitic lasing is occurring.

gain for parasitic lasing is not reached [58]. Using this result, we decided to mis-time PRO2 so that the energy is deposited after the first pass of the seed. Indeed, this step did help reduce the amplitude of the parasitic lasing signal as well as maximize the energy extracted from the crystal. In the future, half-wave plates could be used to rotate the polarization of the pump lasers, which effectively reduces α such that the energy is absorbed more uniformly in the crystal volume.

Even though the amplification was not tested using only the PRO's, a measurement of the small signal gain coefficient could be made to see if this matched the expected value from the fluence of the pumped region. Using the stretched oscillator beam, which is only about 1-2 mm diameter and has energy on the order of 0.5 nJ, a photodiode compared the signal of the beam when it was amplified versus going through unamplified. Since the seed is much smaller spatially, the beam only samples a part of the gain region, which was chosen to be near the center of the crystal. This measurement was performed on the 6 pass crystal as well. Table 1 shows the results of this measurement. The fact that the measured small signal gain values agree reasonably well with the calculated values indicates that pumping the 5 pass with only the PRO lasers, with a diverging seed beam matching the thermal lens of the crystal, should produce gain in line with what the model would predict. Unfortunately, this measurement was performed during a period where the Continuum was not working. However, this measurement along with the photodiode signal looking at the crystal fluorescence described previously indicates parasitic lasing is occurring.

(all in mV)	Signal Thru	Fluor. Level	Amplified	$G = (A - F) / S$	G Expected
6 pass	34	24	130	3.12	3 - 3.5
PRO1+PRO2	64	220	540	5	5 - 6
PRO1 only	64	80	240	2.5	2.2 - 2.7
PRO2 only	64	65	190	1.95	2.2 - 2.4

Table 1.   Measurements of small signal gain in the amplifiers. "G Expected" is calculated based on the fluence map of the pump beams and has uncertainty resulting from the spatial irregularity of the beams.

After the 5 pass is a spatial filter using a 1.25 m lens and a 1.5 m lens with a 0.5 mm diameter pinhole at the focus of the first lens. This images the beam from near the last pass of the 5 pass crystal to a point in space inside the target area. A second telescope with a 50 cm lens and a 1.5 m lens then takes this image and relays it into the compressor. The second telescope originally had a 30 cm lens in place of the 50 cm lens, but it was found that it expanded the beam too much and caused it to clip on the aperture of the 1.5 m lens, which is 3" in diameter. In the short term, we are using the 50 cm lens, but we plan to change that to a 40 cm lens so that the fluence on the gratings is further below the damage threshold of 300 mJ/cm^2. The final step was to set the 1.5 m lens so that the beam is collimated into the compressor, and this was achieved at a low level by checking the beam size at two positions separated by about 7 m. Images of the beam after the spatial filter and the final telescope are shown in Figure 30.
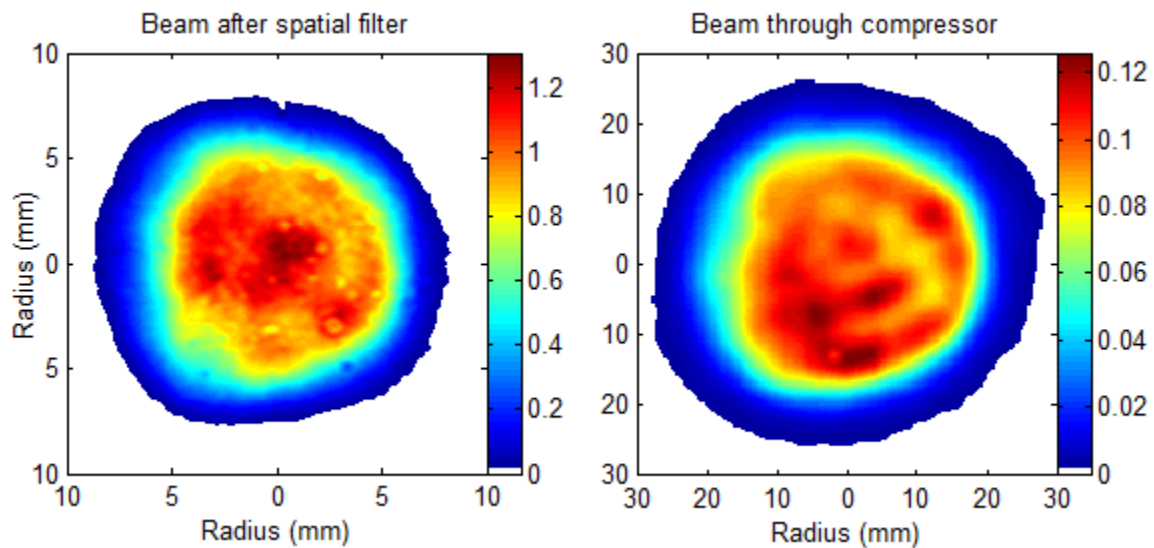
Figure 30. Images of the beam after the spatial filter after the 5 pass (left) and through the last telescope at an image location ~8 m from the collimating lens (right). Fluences shown on the colorbars are in J/cm^2.

Chapter 4. Experimental Setup

In this chapter, the "nuts and bolts" needed to perform the experiments are described. First, an overview of the laser system used is presented, followed by an explanation of the experimental setups. Finally, the diagnostics used to collect the data are explained in detail.

4.1. OVERVIEW OF GHOST LASER

The experiments detailed in this dissertation were performed on the Glass Hybrid OPCPA Scale Testbed (GHOST) laser. As the name implies, this laser was designed to be a testbed for the hybrid glass amplification used on the Texas Petawatt laser [59]. An overview of the GHOST laser will now be presented.

As with many high power lasers, the general principle this laser works from is the concept of chirped pulse amplification [1]. A schematic layout of the laser system is shown in Figure 31. The laser begins with a Coherent MIRA 900 mode locked Ti:Sapphire oscillator operating at a central wavelength of 1057 nm. The oscillator is pumped by a 10 W 532 nm Nd:YVO$_4$ laser. The higher pump energy is required in order to sustain the laser operation at the edge of the Ti:Sapphire emission spectrum [60]. The output from the oscillator is a train of 100 fs, ~1 nJ pulses at a frequency of about 73 MHz. A pockels cell is then used to reduce the frequency of the pulses down to 10 Hz. From there, the pulse enters the stretcher, which chirps the pulse to about 1 ns duration. This is done by forcing the different wavelengths in the pulse to travel different distances − the longer wavelengths travel a shorter distance than the shorter wavelengths, so the lower frequency light is ahead of the higher frequency light (hence the name "chirp"). Now that the pulse is much longer temporally, it will be safe to amplify since the power density will be below the damage threshold of the optics.

The first stages of amplification use optical parametric chirped pulse amplification (OPCPA) [61]. The advantage of this technique is that once the seed pulse saturates, bandwidth can be added to the pulse, which will counteract gain narrowing in

56
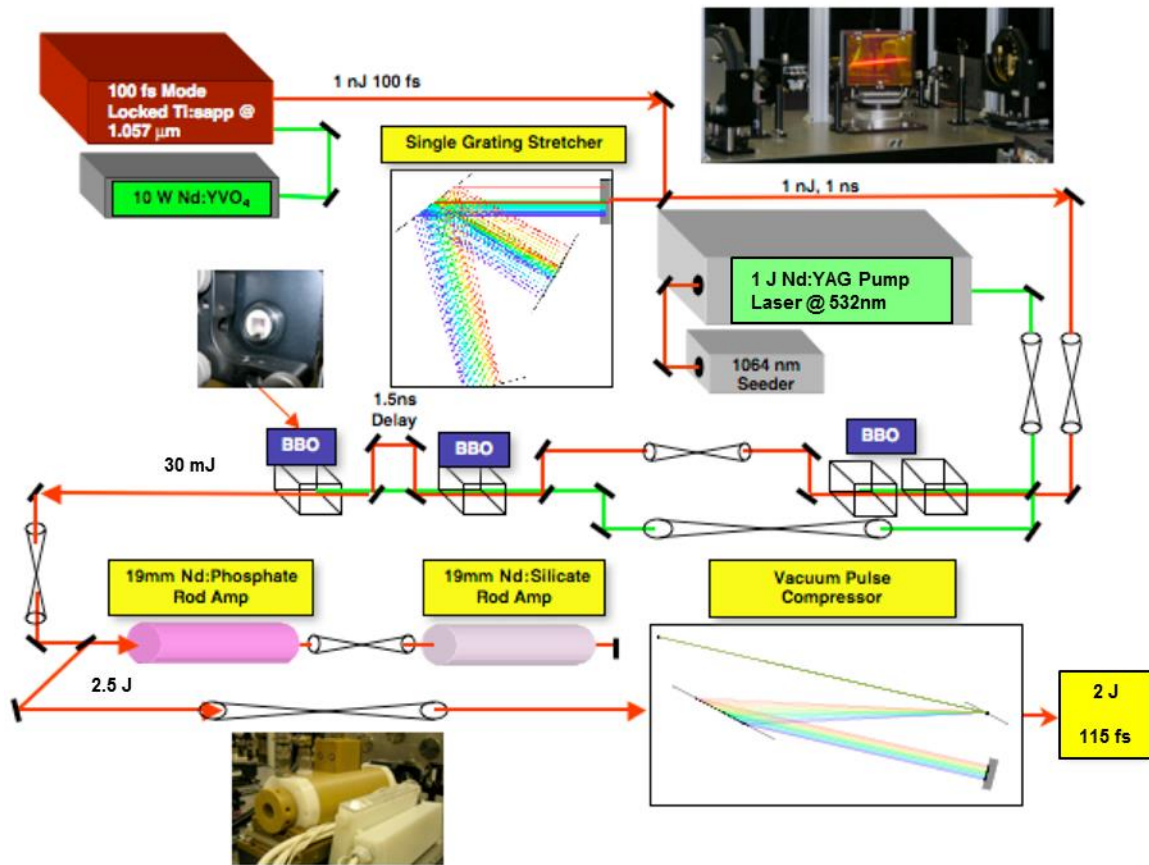
Figure 31.   Schematic layout of the GHOST laser (modified from Ref. 62).

the following amplification stages to enable compression back to near 100 fs. Also, since the amplification is single pass, pre-pulses and ASE are eliminated (unless following stages can introduce them), resulting in a high-contrast laser pulse. OPCPA is a nonlinear optical process based upon difference frequency generation. Here, a Spectra Physics PRO 350 Q-switched Nd:YAG laser operating at 532 nm provides the pump energy which is coupled into the 1057nm seed laser pulse. The pump laser is seeded by a 1064 nm single mode laser to produce a temporally-smooth, low jitter pump pulse, since OPA is strongly dependent on the intensity of the pump pulse. There are two stages of OPCPA, with two BBO crystals per stage. The first stage uses 130 mJ of the pump laser and amplifies the seed pulse to about 100 μJ, a gain of about 10^5. In the second stage, 570 mJ of the pump

laser is used, which brings the seed energy up to about 30 mJ. The much lower gain is attributed to the saturation of the seed pulse.

From here, the pulse enters the glass amplification stage. One Nd:Silicate rod and one Nd:Phosphate rod are set sequentially, and the seed double passes both rods. The reason two glasses are used is that the emission spectrum of these are peaked at two wavelengths (silicate at 1064 nm, phosphate at 1053 nm), and so this will allow for a broader amplification spectrum, which results in a broader amplified pulse. After this stage, the seed is amplified by near a factor of 100 to about 2.5 J. Finally, the pulse enters the compressor, which essentially undoes what the stretcher did. With the ~80% transmission of the compressor, the final compressed laser pulse has about 2 J of energy and a pulse duration of about 115 fs FWHM. Further details on the design and operation of GHOST can be found in Refs. 54 and 62.

4.2. EXPERIMENTAL LAYOUT

In total, there were three experimental runs performed on the GHOST laser. Each experiment had its own layout, although the first two layouts were very similar and only differed by the addition of the streaked interferogram diagnostic. The setup for these experiments will be detailed in this section.

4.2.1. 5 T Field Generator Experimental Layout

The bulk of the data for this dissertation was taken using the setup described in this section. This layout is shown, with beam paths overlaid, in Figure 32. The compressed high energy laser pulse from GHOST is delivered from the vacuum compressor chamber into the target chamber, which enters from the top right of the picture. This beam was sent to a 45" focal length spherical mirror at a slight angle (maybe 1-1.5°), which introduces some astigmatism to the focal spot. However, the focus used for the experiments was the best circular spot between the horizontal and vertical focal points so that the plasma would be approximately cylindrically symmetric. An image of the focus is shown in Figure 33. The FWHM was measured to be 35 μm, which

for a 1 J beam gives a peak intensity of 9×10^{17} W/cm^2. The real peak intensity may have been somewhat lower for reasons that will be described in Chapter 5.
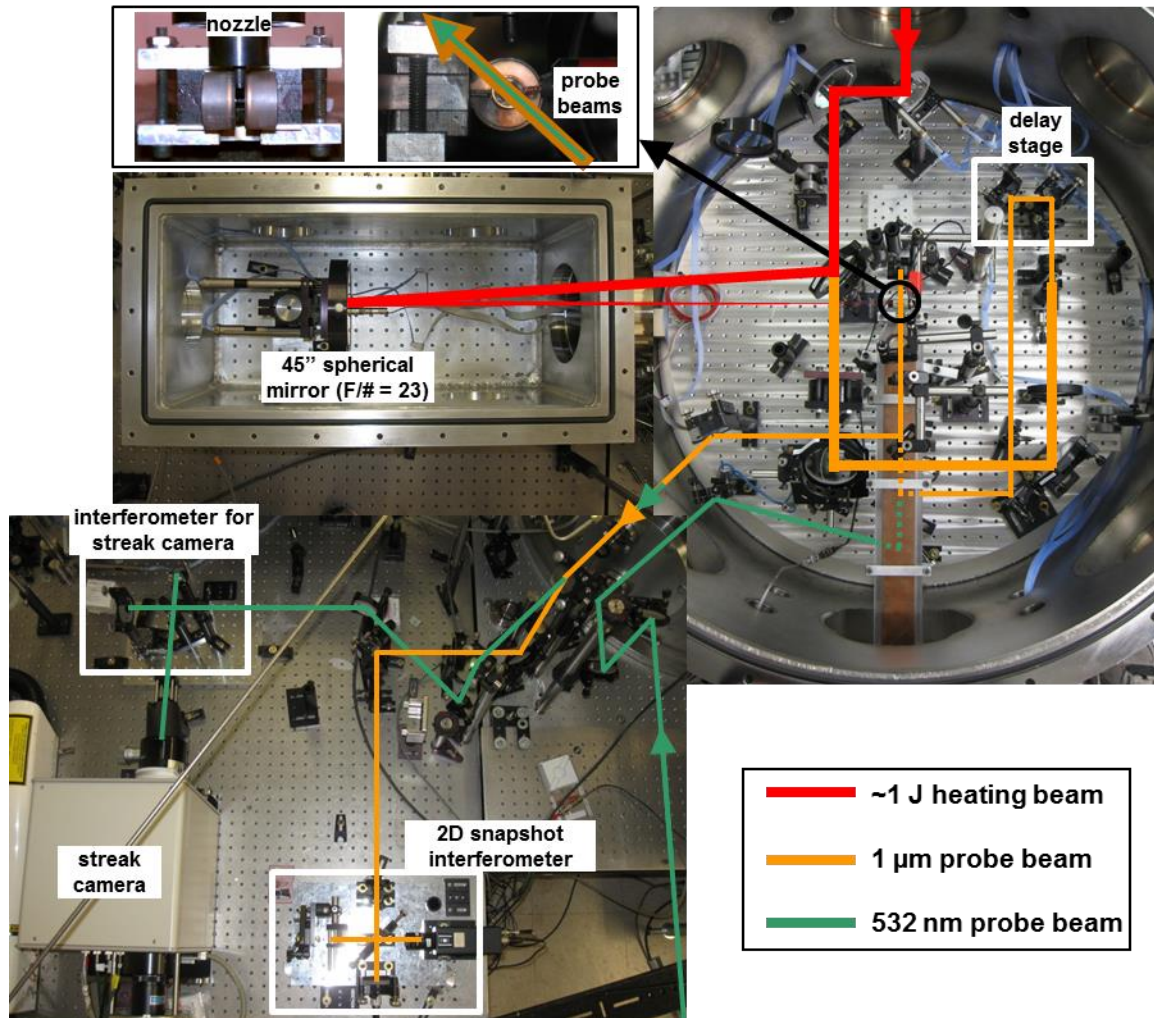
Figure 32.   Overview of the optical layout used for most of the experiments.

The short pulse probe beam needed to probe the plasma was obtained by taking the leak-through of the last mirror that sends the main beam to the spherical mirror. To avoid problems with B-integral, this mirror was 1/4" thick instead of the normal 3/8" or 1/2" thickness. The probe was then periscoped down so that it could pass underneath the transmission line of the pulsed power device. A telescope demagnified the beam from 5 cm diameter to about 8 mm diameter. From here, the beam entered the delay stage, which

had a travel of one inch, allowing for a maximum optical delay of 160 ps between the probe and main beams. The beam then went to a short wave pass mirror underneath the transmission line, which would reflect the 1057 nm short probe, but transmit the 532 nm long probe. This also allowed the two probe beams to be aligned so they were collinear.
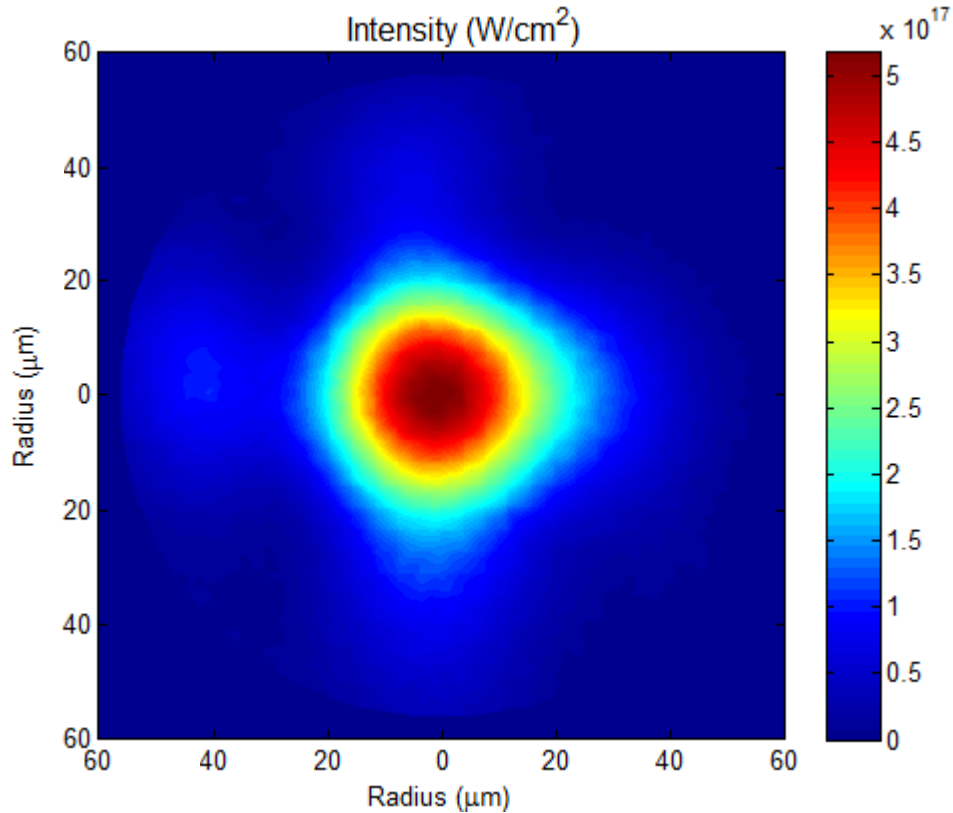
Figure 33.   Focal spot intensity for the 5 T experimental layout.

As mentioned, a second probe beam was needed for probing the plasma, which was generated by a seeded Q-switched Nd:YAG laser in an adjoining room. In order to send the beam to the target chamber, it needed to propagate close to 10 m through air, which would lead to degradation of the spatial profile. To get around this, an aperture was used to sample ~1 mm of the beam. While this only allowed about 1 mJ of energy through, it was enough for the diagnostic. Then, this beam was allowed to free propagate the path to the chamber, resulting in a large (over 1 cm diameter), smooth beam profile. An iris outside the chamber sized the beam to be similar to the short probe beam size.

Once the two probe beams were concentric, they were directed up at a 45° angle between the end of the gas jet nozzle and the end of the transmission line, as shown in the top left inset of Figure 32. The gas jet was a General Valve Series 9 pulsed valve controlled by an Iota One driver. The nozzle attached to the jet was made of delrin instead of aluminum to prevent the current being driven through the coils arcing to the gas jet. It was found that this nozzle material did not significantly affect the gas flow. The expansion cone of the nozzle was 5° full angle to allow it to fit between the coils. Since the main heating beam traveled down the axis of the coils, the probe beams were orthogonal to the plasma created by the main beam.

A mirror above the transmission line collected the beams and sent them to an imaging telescope which magnified the beams by a factor of two. The telescope imaged the beams from the plasma to a point outside the chamber. After the second lens of the telescope, a second short wave pass mirror separated the two beams, reflecting the 1057 nm short probe down and transmitting the 532 nm probe. The short probe had a second telescope which collected the image point and relayed it to the CCD camera at the output of the interferometer. The long probe also had a telescope to send the image point through its interferometer. Both telescopes were one-to-one imaging. It was found that more magnification was needed on the long probe, so a final 35 mm lens was added after the interferometer to expand the beam about 4x. It also imaged the image point after the interferometer onto the input slit of the streak camera.

4.2.2. Sandia Pulsed Power Experimental Layout

The third experiment performed used a pulsed power device built for another experiment in the research group [63]. It was capable of producing much stronger fields than the homebuilt device, but due to problems with arcing when the gas jet was fired, the strongest field used in this experiment was 14 T. Since the Sandia device used its own vacuum chamber which was connected to GHOST's vacuum system, a new optical layout was needed for the probe diagnostics. This will be described here.

61

A picture showing the first part of the layout is shown in Figure 34. The compressed pulse from GHOST comes in from the top. Two mirrors direct it to the same 45" focal length spherical mirror used in the previous experiments, and the beam was focused through the center of the coils in the target chamber. The maximum field produced by the device is strong enough to destroy the coils, so the nozzle of the gas jet was set at a 45° angle with respect to the pump beam (with the gas emitted in the laser propagation direction), but still perpendicular to the probe beams. This meant the focus was still cylindrically symmetric, but the plasma conditions along the laser axis were not as uniform as in the previous experiments.
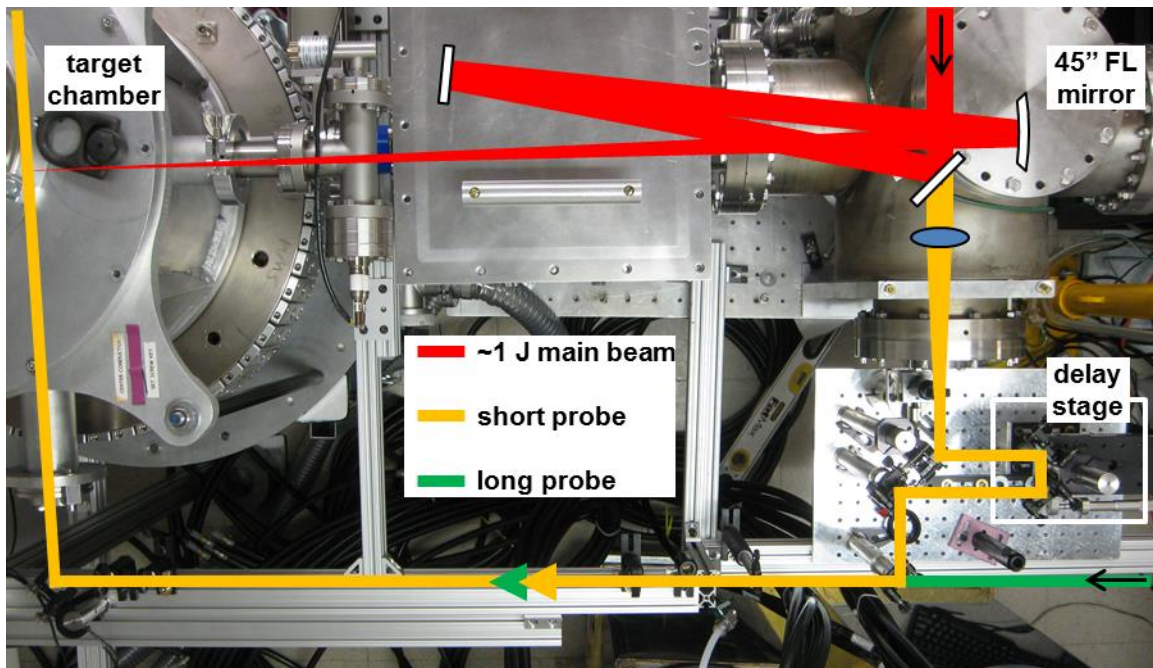
Figure 34.   Overview of part of the optical layout used for the higher field experiment.

The leakage of the first mirror was used for the short pulse probe beam. The beam was immediately demagnified to about 6 mm diameter and sent to a delay stage. A 2" travel translation stage was used, allowing a delay of over 300 ps. After that, the beam went to the short wave pass mirror which combined the two probes. As in the previous experiments, the Nd:YAG laser was used for the long pulse probe. This beam was routed to the short wave pass mirror in a similar way as before.

Once the two beams were combined, an iris was set at the object plane of a 2x magnifying telescope. The image of this telescope was set at the plane where the plasma would be created. The iris allowed the size of the probe beams to be set as well as sample both larger beams to get a more uniform spatial profile. Setting the iris at the image plane prevented diffraction rings from obscuring the collected data images, as long as the plasma plane was imaged correctly. The beams were sent into the target chamber and through the coils where the plasma would be, once again orthogonal to the main laser pulse axis. Another 2x magnifying telescope collected the beams, imaging them from the
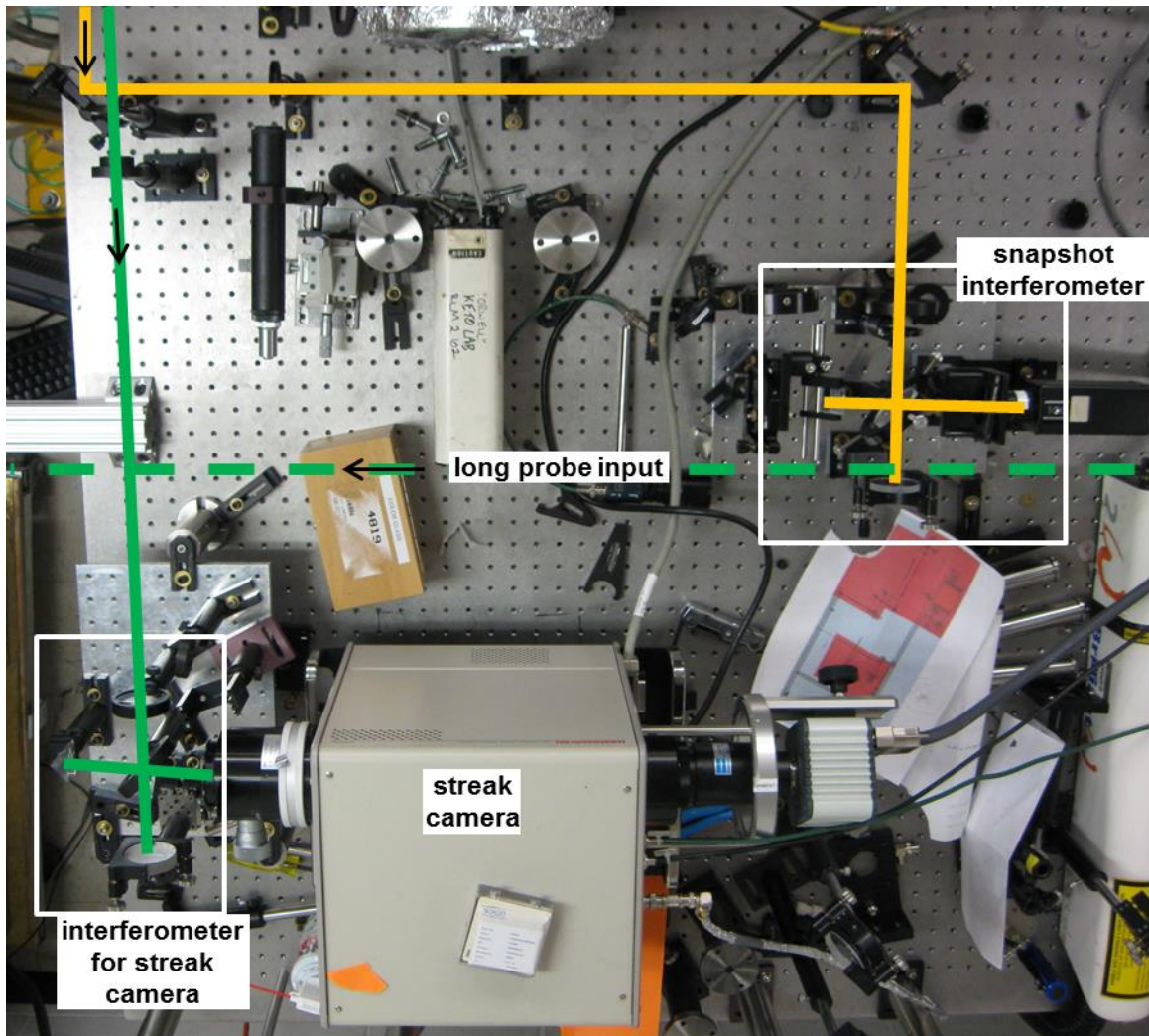
Figure 35.   Overview of the diagnostics after the two beams have been separated. The long probe is also seen heading to the previous figure.

plasma to separate relay points after the second short wave pass mirror which separated the two beams.

The rest of the layout is shown in Figure 35. The short probe then entered a final 2x magnifying telescope, which took the image from the relay point and imaged it to the CCD camera at the output of the same interferometer used in the previous experiments. The long probe, once separated, was again rotated by a periscope so the laser axis would be orthogonal to the slit of the streak camera. A final 4x magnifying telescope took the relay image through the interferometer to the input slit.

Unfortunately, because of arcing problems when using the gas jet with this pulsed power machine, a plastic tube was needed to divert the gas flow away from the current flow, as shown in Figure 36. There were still arcing problems when the jet was fired at the optimal time for cluster formation, and the short-term solution was to fire the gas jet 500 μs after the optimal time so that the gas was in the chamber for less time before
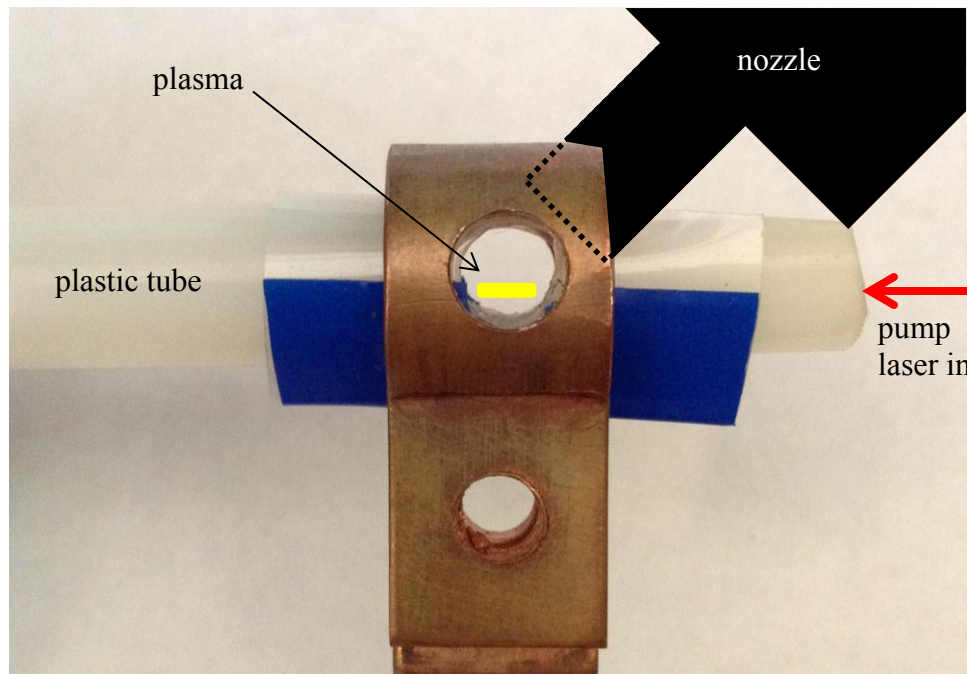
Figure 36.   Side view of the coil and nozzle as used during the Sandia pulsed power experiment. The pump pulse enters from the left and the probe goes through the hole in the coil to probe the plasma. The clear plastic tube helped divert the gas flow away from the coil contacts.

the current flow. The combination of these two issues led to smaller clusters being formed for the same backing pressure as well as less uniformity of the experimental conditions from shot to shot. This resulted in interferograms from shots with fairly identical conditions (laser energy, backing pressure, pump/probe delay) looking quite different, occasionally with rather strange shapes. Ultimately, most of the data from this run ended up not being useful.

4.3. DIAGNOSTICS

In the experiments performed on the GHOST laser, two diagnostics were used to study the plasma evolution. Both diagnostics made use of modified Michelson interferometers where a right-angle prism was used in one leg of the interferometer (see Figure 38). First, the underlying physics of how these diagnostics work will be explained.

4.3.1. Interferometry

In order to measure the expansion of the plasma as a function of time, we measured the electron density. This can be done by sending a probe laser beam through the plasma. The index of refraction of the plasma is a function of the electron density, and as such, the laser pulse propagating through plasma will accumulate phase. This phase is given by

$$\varphi = \int \vec{k} \cdot d\vec{l} = \int \frac{\omega}{c} n \, dl \qquad (4.1)$$

where φ is the phase, ω is the frequency of the laser, and n is the refractive index of the plasma,

$$n = \sqrt{1 - \frac{\omega_p^2}{\omega^2}} = \sqrt{1 - \frac{n_e}{n_c}} \qquad (4.2)$$

where

$$\omega_p^2 = \frac{n_e q^2}{\varepsilon_0 m_e} \qquad (4.3)$$

In these equations, ω_p is the plasma frequency; n_e, m_e, and q are the density, mass, and charge of electrons in the plasma; and n_c is the critical electron density, defined to be the frequency at which the laser and plasma frequencies are equal:

$$n_c \equiv \frac{\omega^2 \varepsilon_0 m_e}{q^2} \qquad (4.4)$$

Consider now the two beams in the interferometer. The electric fields can be described simply by

$$E_1 e^{i\omega t}, E_2 e^{i(\omega t + \varphi)} \qquad (4.5)$$

When the two beams are recombined by the beamsplitter, the resulting electric field is

$$E_T = (E_1 + E_2 e^{i\varphi}) e^{i\omega t} \qquad (4.6)$$

and the resulting intensity of the light is

$$I = |E_T|^2 = (E_1^2 + E_2^2)\left(1 + \frac{2E_1 E_2}{E_1^2 + E_2^2}\cos\varphi\right) \qquad (4.7)$$

Taking the difference of the phases of the beam with the accumulated phase and the reference beam (meaning $n \cong 1$) from Equation (4.1), we get

$$\Delta\varphi = \int (n-1)\frac{\omega}{c}dl = \int \left(\sqrt{1 - \frac{n_e}{n_c}} - 1\right)\frac{\omega}{c}dl \qquad (4.8)$$

This expression can be simplified if the electron density in the plasma is much less than the critical density, which is equivalent to saying the laser frequency is much higher than the plasma frequency. If this is the case, the phase shift is given by

$$\Delta\varphi \approx \frac{\omega}{2cn_c}\int n_e dl \qquad (4.9)$$

In the experiment, the plasma is a small cylinder, so the phase shift imparted on the laser pulse is integrated along chords across the cylindrical plasma. Equation (4.9) needs to be inverted to solve for the electron density, and given the cylindrical symmetry, the technique of Abel inversion [48] is used. An illustration of the situation is shown in Figure 37. Rewriting Equation (4.9) using common laser parameters, we have

$$\varphi(x) = \frac{\pi}{\lambda n_c} \int_0^{x_0} n_e(r)dx \qquad (4.10)$$

Converting this to cylindrical coordinates, we have

$$\varphi(x) = \frac{\pi}{\lambda n_c} \int_{y_0}^{a} n_e(r) \frac{r}{\sqrt{r^2 - x^2}} dr \qquad (4.11)$$

Using the Abel inversion, the electron density is then

$$n_e(r) = -\frac{\lambda n_c}{\pi^2} \int_r^{a} \frac{d\varphi(x)}{dx} \frac{dx}{\sqrt{x^2 - r^2}} \qquad (4.12)$$
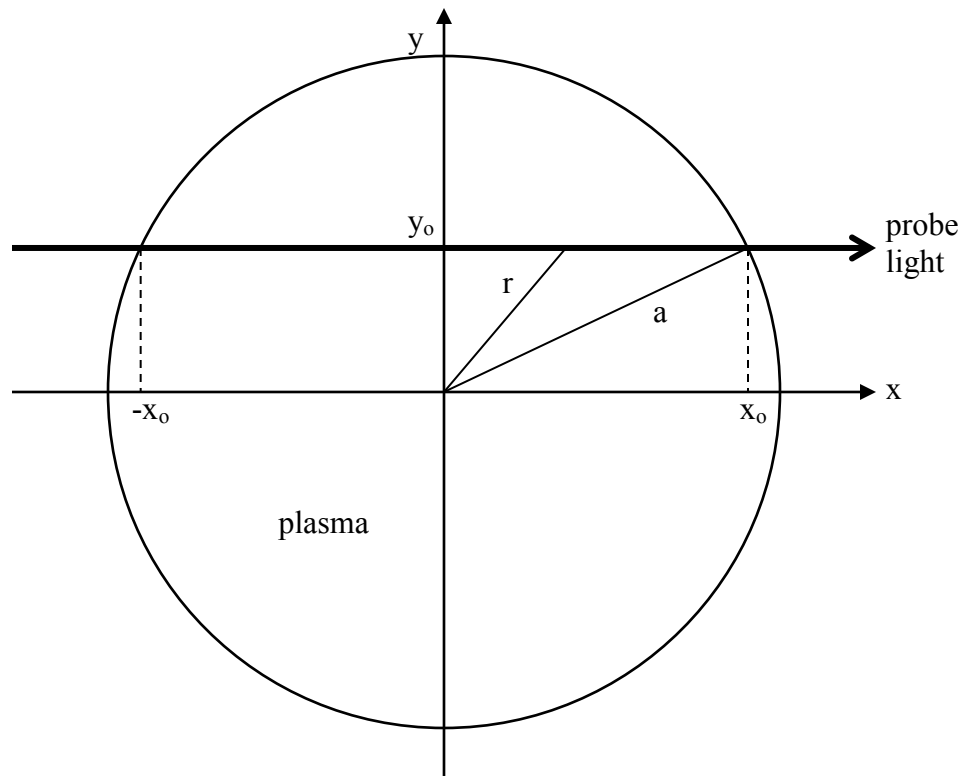
Figure 37.   Illustration of variables used for the Abel inversion of cylindrical plasma. Probe laser travels in x-direction across the plasma of radius a.

We see, then, that the electron density depends on the derivative of the phase, which can be problematic if the phase data is noisy as this will introduce unwanted errors

67

into the result. In an effort to alleviate this problem, Equation (4.12) can be integrated by parts [64], which gives

$$n_e(r) = -\frac{\lambda n_c}{\pi^2}\left(\frac{\varphi(x)}{\sqrt{x^2-r^2}}\Bigg|_r^a + \int_r^a \frac{x\varphi(x)}{(x^2-r^2)^{3/2}}\,dx\right) \tag{4.13}$$

Dealing with the evaluation of the first part, especially at the lower limit where $x = r$, requires a little work. Since the phase is continuous, we can rewrite that term as

$$\frac{\varphi(x)}{\sqrt{x^2-r^2}}\Bigg|_r^a = \frac{\varphi(a)}{\sqrt{a^2-r^2}} + \left(\frac{\varphi(r)}{\sqrt{x^2-r^2}}\Bigg|_r^a - \frac{\varphi(r)}{\sqrt{a^2-r^2}}\right) \tag{4.14}$$

The first term in the parentheses can be rewritten as an integral, and the result is

$$\frac{\varphi(x)}{\sqrt{x^2-r^2}}\Bigg|_r^a = \frac{\varphi(a)-\varphi(r)}{\sqrt{a^2-r^2}} - \int_r^a \frac{x\varphi(r)}{(x^2-r^2)^{3/2}}\,dx \tag{4.15}$$

Substituting this back into Equation (4.13) gives the final result:

$$n_e(r) = -\frac{\lambda n_c}{\pi^2}\left(\frac{\varphi(a)-\varphi(r)}{\sqrt{a^2-r^2}} + \int_r^a \frac{x[\varphi(x)-\varphi(r)]}{(x^2-r^2)^{3/2}}\,dx\right) \tag{4.16}$$

4.3.2. 2D Snapshot Interferometer

The first diagnostic implemented for these experiments was a two dimensional "snapshot" interferogram. In describing the experimental layout, it was mentioned that one probe beam was the mirror leakage of the main heating beam, which makes it short in time (~115 fs). As such, when this probe passes through the plasma, it captures a nearly instantaneous snapshot of the plasma. The probe light is then imaged from the plasma to the CCD camera at the output of the interferometer. Many of these images are then used to piece together the plasma evolution in time by varying the delay between the main heating pulse and the probe pulse.

A standard Michelson interferometer has two legs with flat retro-reflecting mirrors, one of which is on an adjustable delay stage, and the sample to be studied is in the optical path of one of the legs. In this experiment, the plasma is probed outside of the

interferometer, so a standard Michelson will not work. Since the probe is much larger than the plasma, part of the probe beam that has not been affected by the plasma can be used as the reference for the interferometer. In order to do this, a right angle prism is used in one of the legs of the interferometer instead of a flat mirror, as shown in Figure 38. Since the laser pulse is so short, the two legs must have exactly the same optical path length in order to produce fringes.
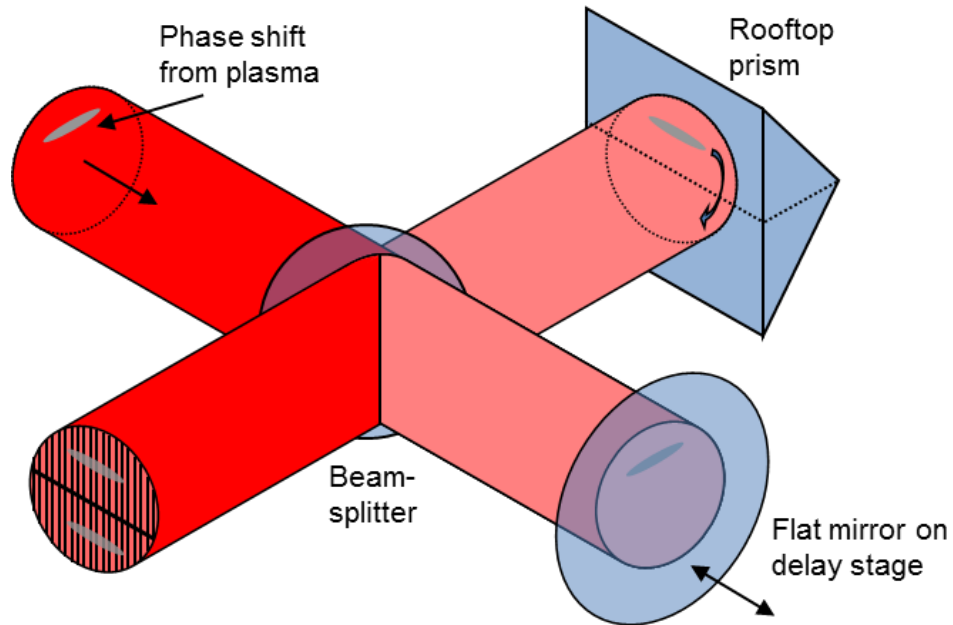
Figure 38.   Diagram of a modified Michelson interferometer. One leg of the interferometer inverts the beam via the right angle prism, which provides a reference to interfere with the part of the probe affected by the plasma.

A sample image produced by the interferometer is shown in Figure 39. Clearly, the image is 2D with spatial dimensions parallel and perpendicular to the main laser propagation axis. However, especially when the main laser is in the region captured in the image, as in Figure 39, the dimension parallel to the laser axis can be transformed into a temporal axis. The straight fringes on the left are times before t_0, while the curved fringes indicating plasma formation to the right are times after t_0. This fact will be very useful in the analysis presented in Chapter 5.
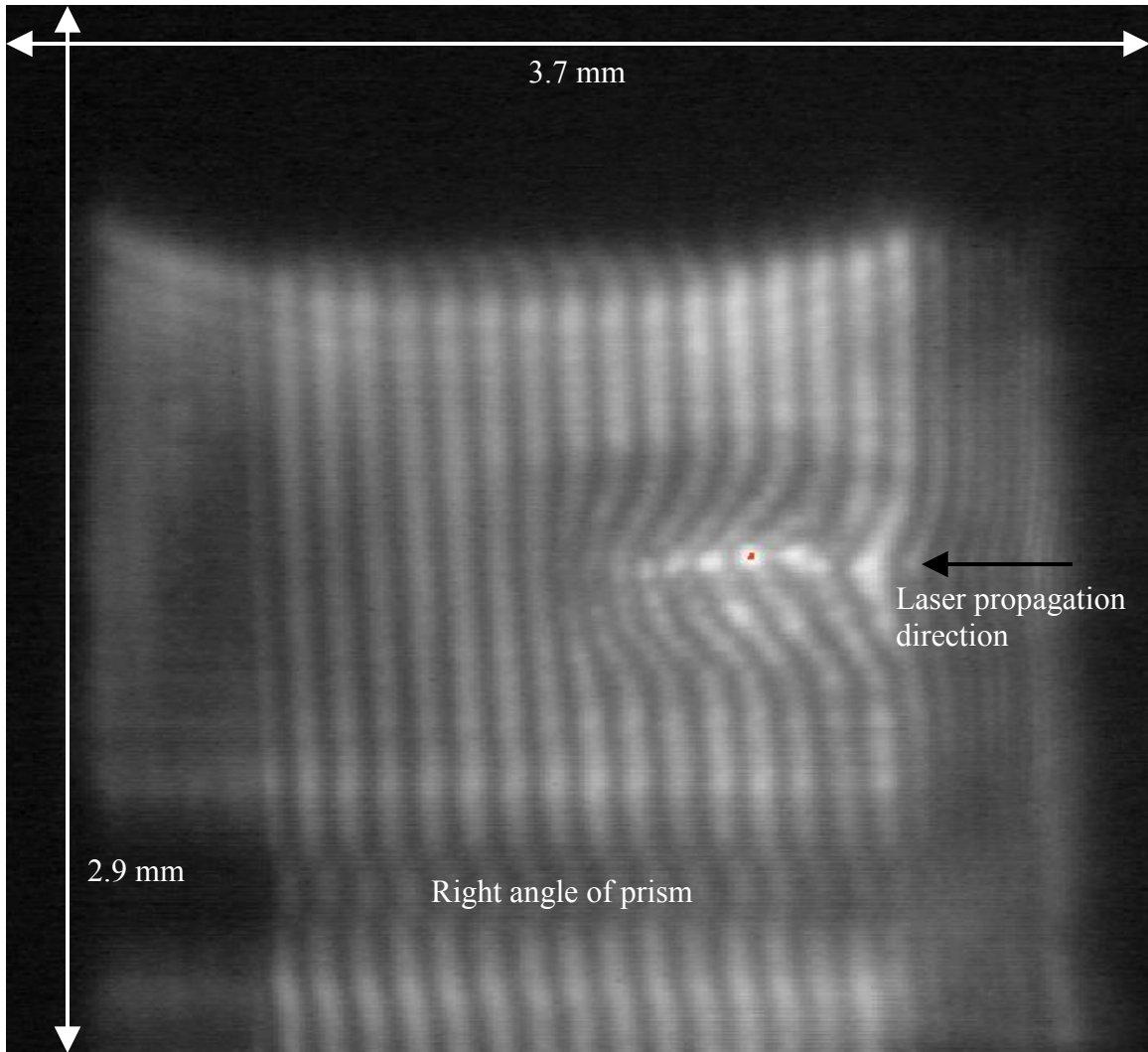
Figure 39.   Sample snapshot interferogram of an Argon plasma being created.

4.3.3. Streaked Interferogram

The second diagnostic used in these experiments is an extension of the snapshot interferometer explained in the previous section. While piecing together many 2D images at different time delays does work, it relies on the heating laser being reasonably stable through all of the shots, which could number in the hundreds for good statistics. For example, a low energy shot at an early snapshot and a high energy shot at a later snapshot could give a misleading result for the plasma evolution. A way around this issue is to use a streak camera to capture the complete evolution of the plasma in one shot.

70

The schematic layout of a streak camera is shown in Figure 40. The light is incident on an adjustable slit, which is imaged to a photocathode via internal imaging optics. This converts the photons to electrons, which are accelerated inside the streak tube toward a phosphor screen. Between the photocathode and the phosphor screen are electrodes which deflect the line of electrons to give the temporal aspect of the image. The phosphor screen converts the electrons back to photons, which then go through an image intensifier/multichannel plate to amplify the signal (if needed). Finally, output optics image the light to a camera. In using the streak camera, the tradeoff is that while the evolution of the plasma can be captured in one shot, only one point along the laser axis can be probed. However, using this data along with the 2D data can provide a more complete understanding.
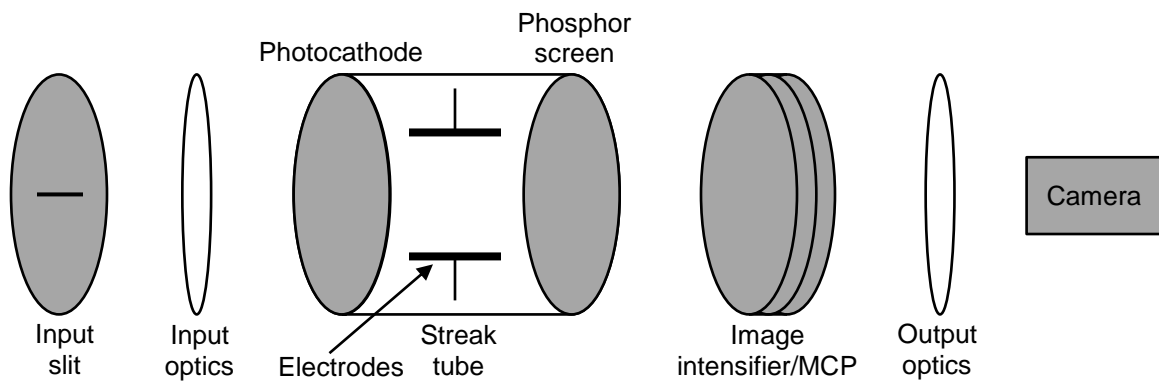
Figure 40.   Schematic overview of a streak camera.

Implementation of the streak camera is as follows. Using the same style of interferometer described in the previous section, the normal CCD camera at the output is replaced with the streak camera. Also, since the input slit is parallel to the plane of the interferometer (for ease of mounting optics), the prism is rotated 90°. This also demanded that the probe beam be rotated 90° using a periscope so that the beam could be inverted as before. The probe beam is imaged onto the input slit of the streak camera. The laser propagation axis is aligned perpendicular to the slit so that the streak camera is taking a radial cross section of the plasma.

Since our streak camera, a Hamamatsu C7700, has a maximum temporal resolution of about 3 ps at the 500 ps sweep speed, a temporally longer probe beam must be used. As described previously, a seeded Spectra Physics GCR270 Q-switched Nd:YAG laser was used for this probe beam. Since the pulse duration is about 10 ns FWHM, this is plenty long to capture the initial 0.5 ns expansion of the plasma. It was important that the laser be seeded because in unseeded operation, multiple modes in the laser pulse will lead to intensity variations that will make analyzing the resulting image much harder.

Both the streak camera and the probe laser must be synchronized with the main heating pulse from GHOST. This was done as follows. First, the green laser pulse was timed with respect to the GHOST pulse using an SRS box. Then, in order to trigger the streak camera with minimal jitter, an EOT ET-3000 photodiode with rise time of <175 ps was used. This photodiode looked at the rejected light from a Brewster window before the glass rods, which was attenuated but set at a level which saturated the photodiode so that the rise time was minimized. Then, since this photodiode directly triggered the streak camera, the length of coaxial cable between the two, plus the internal trigger delay of the camera, had to match the time for the laser to travel from that window to the focus plus the additional path length the probe light took to go from plasma to camera. Watching when the plasma would appear on the streak camera confirmed that the jitter was at most the rise time of the photodiode, and often less.

There are two ways of using this diagnostic, which are dependent on how the fringes from the interferometer are oriented relative to the input slit of the streak camera. Two sample images which illustrate this are shown in Figure 41. Each image is a 500 ps streak (temporal axis is vertical). In the left image, the fringes are oriented parallel to the slit, or perpendicular to the laser axis as in Figure 39. The right image shows the fringes oriented perpendicular to the slit. Each has an advantage and disadvantage. When the fringes are perpendicular to the slit, analyzing the image is much easier, whereas looking at the image does not immediately provide much information. Conversely, the left image

is very easy to look at and discern what is happening to the plasma. Analyzing the image to extract the electron density, however, is very hard, so in some way it is not as useful.
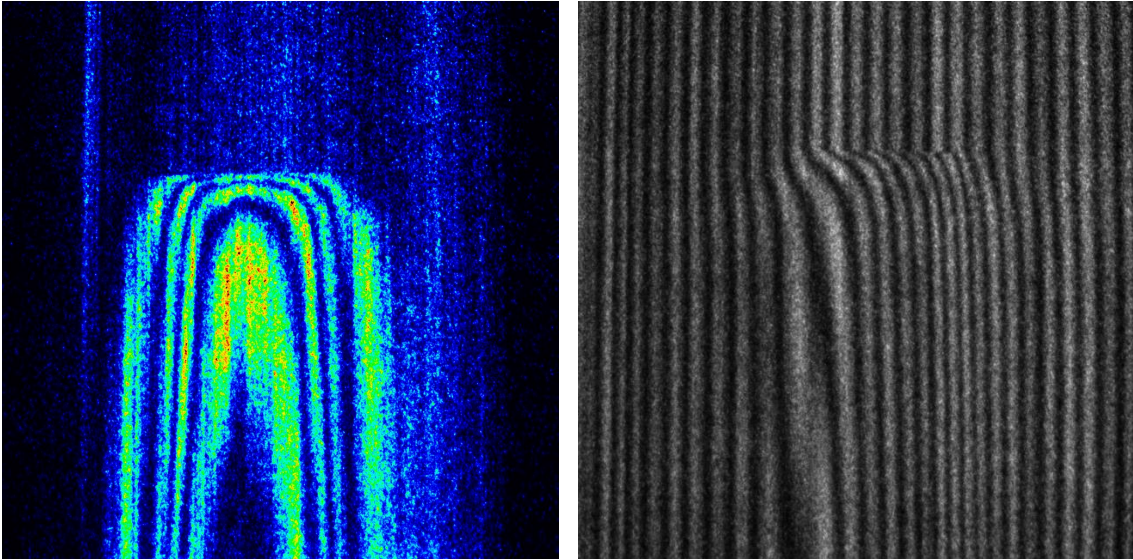
Figure 41.   Two sample images of Argon plasma showing the two ways of
             implementing the streaked interferogram, or "streakogram", diagnostic.

4.3.4. Extracting Phase

As discussed in Section 4.3.1, the probe light will accumulate phase as it traverses the plasma. And, as seen in Equation (4.12), the phase shift measured by the probe beam is required to calculate the electron density. This means we need to extract the phase shift information out of the captured interferograms shown in Sections 4.3.2 and 4.3.3. An overview of the process of extracting the phase information will be presented in this section.

First, the output beams of the interferometer are oriented such that they arrive at the camera with an angle, which is what produces the straight fringes. This represents two identical phase fronts interfering with each other in a normal way. When one of the beam's phase fronts is altered, this results in distorted fringes, as seen in the sample interferograms shown in the previous sections. Using the power of fast Fourier transforms, it is relatively straightforward to extract the information. Figure 42 shows the sequence of steps required to extract the phase shift of an image. A lineout of the

reference fringes is shown compared against a lineout of fringes which have been distorted by the plasma, shown in panel (a). The Fourier transform of the two lineouts are shown next. The reference FFT reveals the reference frequency peak, which is not as clearly seen in the FT of the distorted fringes. Now, we need to filter out the unnecessary information, such as high frequency noise and the amplitude changes (the zero frequency peak). This is done using a two-sided Gaussian filter around the reference frequency peak, as shown in panel (d). The result of this filtering is shown in panel (e). In order to remove the reference frequency of the fringes, we shift this to the left such that the peak reference frequency is now at the zero frequency position. Taking the inverse Fourier transform results in a complex array given by

$$A(x) = a(x)e^{i\varphi(x)} \tag{4.17}$$

where a is the amplitude of the signal and φ is the phase. Panel (f) shows the phase obtained, which has 2π discontinuities. Removing these discontinuities, while seemingly simple, can prove to be quite difficult, with entire books written on the subject known as phase unwrapping [65]. Finally, the unwrapped phase map is input into the integral, and the electron density can be obtained.

Analyzing the streakogram shown on the left side of Figure 41 is trickier because there is no reference frequency which can be filtered out. In this case, after taking the initial 2D Fourier transform of the image concatenated with a vertical mirror image (so that the FFT has a symmetric pattern), the "zero" frequency in each direction was set to zero, which essentially removes the DC intensity variation information. Additional prefiltering removed noise with frequencies higher than the frequencies of interest. Doing the inverse Fourier transform produced the phase, and the process from this point is similar as in the standard case described above.
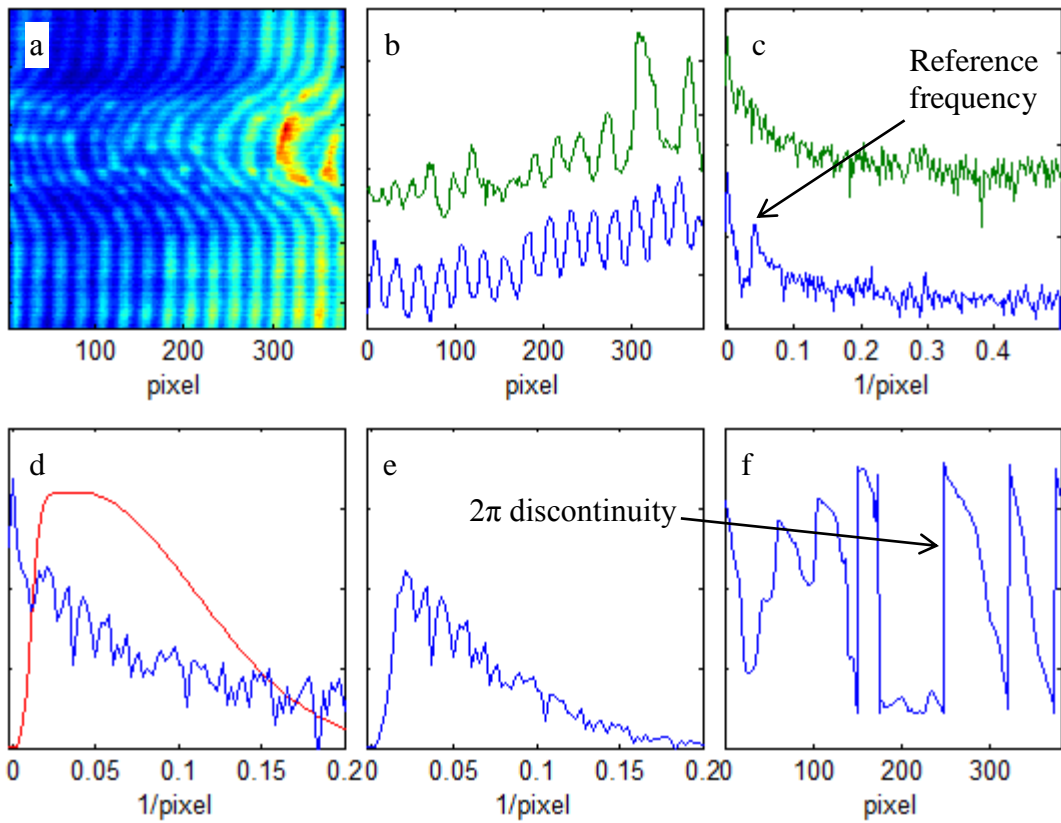
Figure 42.   Sequence of steps used to extract phase information from an image (a).
Lineouts of reference (red) and distorted (blue) fringes are shown (b) with
their respective Fourier transforms (c). The distorted FFT is shown with the
Gaussian filter overlaid (d), and the result of the filtering is shown in (e).
The complex part of the inverse FFT, containing the phase information, is
shown in (f) with the 2π discontinuities.

Chapter 5. Study of a Picosecond-Scale Relativistic Ionization Front

The primary focus of this work was to explore the impact an external magnetic field would have on the expansion and evolution, on a time scale of tens to hundreds of picoseconds, of plasma created by irradiating clustered-gas targets with a high intensity laser. While this objective was achieved, as described in Chapter 6, an additional study was necessary to understand the initial conditions of the experiment for the longer time study. As a result of this analysis, further understanding of the behavior of such a plasma on a time scale of 1-5 ps was achieved, as well as the first observation of a new ionization mechanism which was understood through the use of Particle-in-Cell (PIC) simulations. The results of this data, analysis, and modeling are presented in this chapter.

5.1. EXPERIMENTAL DATA

The experimental conditions used for this data are as follows. This data is focused primarily on argon gas, with comparisons drawn to helium gas. The backing pressure of the gas jet for argon was 100 PSI and 150 PSI, while the helium gas used only 150 PSI in this data. The laser energy at the target averaged about 1 J, but there was significant dither in the energy at the time the data used in this analysis was taken. Using the Hagena parameter [66],

$$\Gamma^* = k \frac{(0.74d/\tan\alpha)^{0.85}}{T_0^{2.29}} P_0 \tag{5.1}$$

we can estimate the size of the clusters expected, where k is a gas-dependent constant related to van der Waals bond formation, α is the half angle of the nozzle, d is the nozzle diameter (mm), P_0 is the backing pressure (mbar), and T_0 is the temperature of the nozzle (Kelvin). For argon at room temperature and the pressures above, with $k = 1650$ [67] and $d = 0.75$ mm, the Hagena parameter is then about 77,000 and 116,000, respectively.

The scaling of cluster size with the Hagena parameter is usually given by

$$N = 33\left(\frac{\Gamma^*}{1000}\right)^{2.35} \tag{5.2}$$

where N is the average number of atoms in the cluster. However, this scaling is generally accurate only up to $\Gamma^* \sim 10,000$ [68]. Dorchies, *et al.*, found that a different scaling is more accurate for larger values of Γ^*, which is [68]

$$N = 100 \left(\frac{\Gamma^*}{1000}\right)^{1.8} \tag{5.3}$$

Still another proposed scaling for larger Γ^* is given by Buck, *et al.*, which is [69]

$$N = \exp(-12.83 + 3.51(\ln \Gamma^*)^{0.8}) \tag{5.4}$$

The cluster radius can be calculated from N using

$$R[\text{nm}] \approx \frac{(9N)^{1/3}}{10} \tag{5.5}$$

Table 2 shows the cluster radii (in nm) that these scaling laws predict. However, recent data taken by a former master's student in our group, Andreas Henig, suggests the cluster size could be even smaller than what is predicted here [70]. Also, work performed by Lu, *et al.*, focusing on argon clusters from narrow conical nozzles measured even smaller sizes [71]. Since the last two results presented do have data with narrow conical nozzles, it is likely the cluster sizes for argon in these experiments are in this range rather than the larger values given by Equations (5.3-5). Helium, on the other hand, has a value of $k = 3.85$ [67], which means the gas will not cluster at these pressures.

	Hagena	Dorchies	Buck	Henig	Lu
100 PSI	20.1	13.1	9.7	6.6 (200 PSI)	3.7 (α=5°)
150 PSI	27.6	16.7	12.2	7.8 (300 PSI)	4.3 (α=5°)

Table 2. Cluster radius for argon (in nm) predicted by three scaling laws compared with two experimental results.

It is also important to know the average density of the gas coming out of the nozzle. This can be measured experimentally [72] or calculated [68]. Using the set of equations described in Ref. [68], the atomic density of the gases at 100 PSI and 150 PSI is about 3.5×10^{18} cm^{-3} and 5×10^{18} cm^{-3}, respectively. We also measured the gas density of the gas jet using a Q-switched Nd:YAG laser and a Mach-Zehnder interferometer. A sample image at 150 PSI for argon is shown in Figure 43, as well as the extracted gas

density. Since one leg of the interferometer passes through the gas, it will accumulate a phase shift due to the refractive index of the gas. Similar to what is done for the electron density interferograms, this image can be Abel inverted to give the gas density. The values for the gas density given above are for the density emerging from the nozzle, and Figure 43 shows that our measured gas density matches the theoretical prediction quite well. However, the plasma was generated between 3 and 4 mm from the nozzle output, and the density here is somewhat lower, roughly 3×10^{18} cm^{-3} on average. Similarly, the 100 PSI density at the location of the experiment was lower, roughly 1.5×10^{18} cm^{-3} on average.
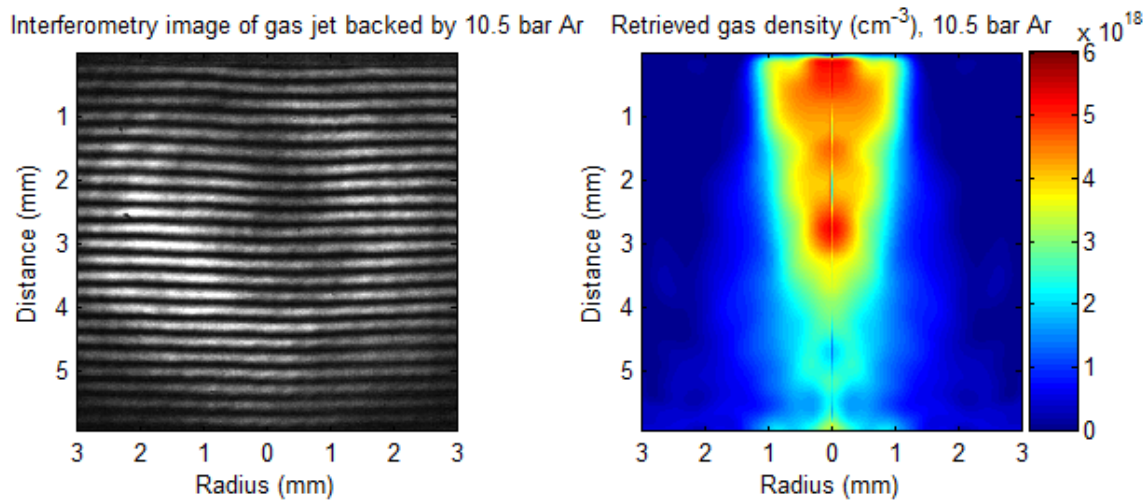
Figure 43.   Interferogram for 150 PSI argon measuring the gas density out of the nozzle (left), and analyzed gas density data (right). The output of the nozzle is at the top of each image.

First, let us consider the 150 PSI helium data. The reason for this is that since the helium is just monatomic gas, it will give us a baseline for what the laser will ionize by itself since the electrons will not retain any energy after they are ionized. As it turns out, this data by itself required some thought to explain. Figure 44 shows two sample interferograms of helium plasma at an early stage of evolution – so early, in fact, that the ionization from the laser itself is seen in the first image. Figure 44 also shows the retrieved electron density profile from the interferograms, as well as lineouts of both plasmas. The time between the snapshots is 75 ps, and little to no plasma expansion is

measured, indicating that the laser essentially "burned" a path through the gas. It is worth noting that the maximum electron density measured provides confirmation of the measurement of the neutral gas density performed with argon.
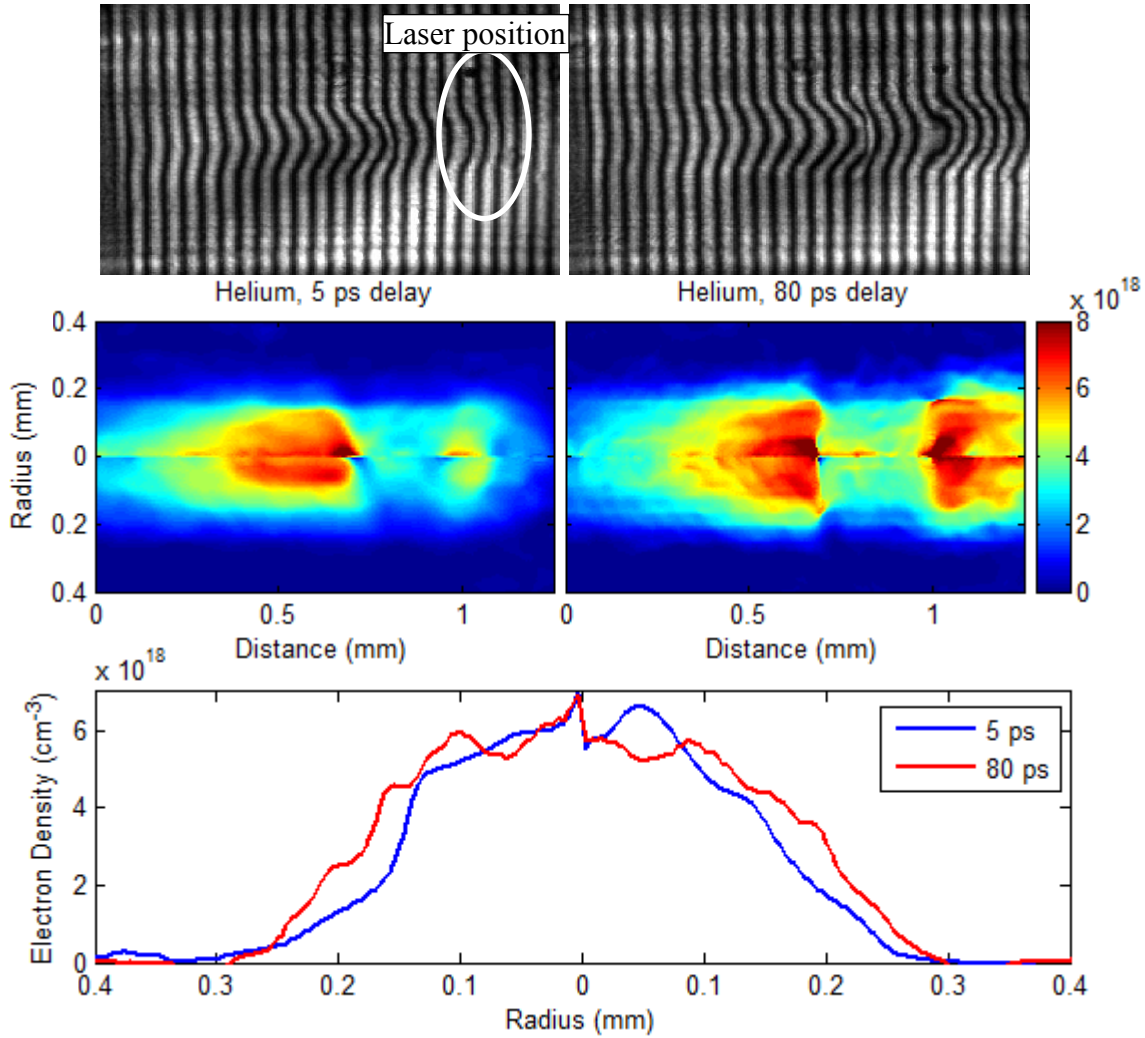
Figure 44.   Two helium plasmas separated by 75 ps, with their retrieved electron density profiles. The lineouts in the bottom plot are at z = 0.5 mm. The laser propagates from left to right.

One thing that stands out about this data is the size of the plasma, roughly 200 μm in radius (at a level of 10^{18} cm^{-3} electron density). As shown in Section 4.2.1, the measured FWHM of the laser focus is only 35 μm, so it is not immediately clear why the plasma is so much larger since there is little to no expansion at later times. The answer is

shown in Figure 45. Using neutral density (ND) filters calibrated at 1057 nm, the focal spot of the OPA beam was observed using a microscope, similar to how the measurement of the focus was done during the experiment. Then, in order to observe the lower intensity parts of the focus, ND was systematically removed such that the center saturated the camera, and an image was saved with each removal of ND. A total ND of nearly 3.0 was removed, allowing observation of the focal spot with a dynamic range of over three orders of magnitude. Using the calibration factors for the ND filters, the pixel values for the images could be rescaled and pieced together, producing the image in Figure 45. This clearly shows that there are spatial wings of the focal spot which extend out to about 200 μm radius which have sufficient intensity to ionize the gas (using a pulse energy of 1 J in this plot). This explains the large size of the plasma.
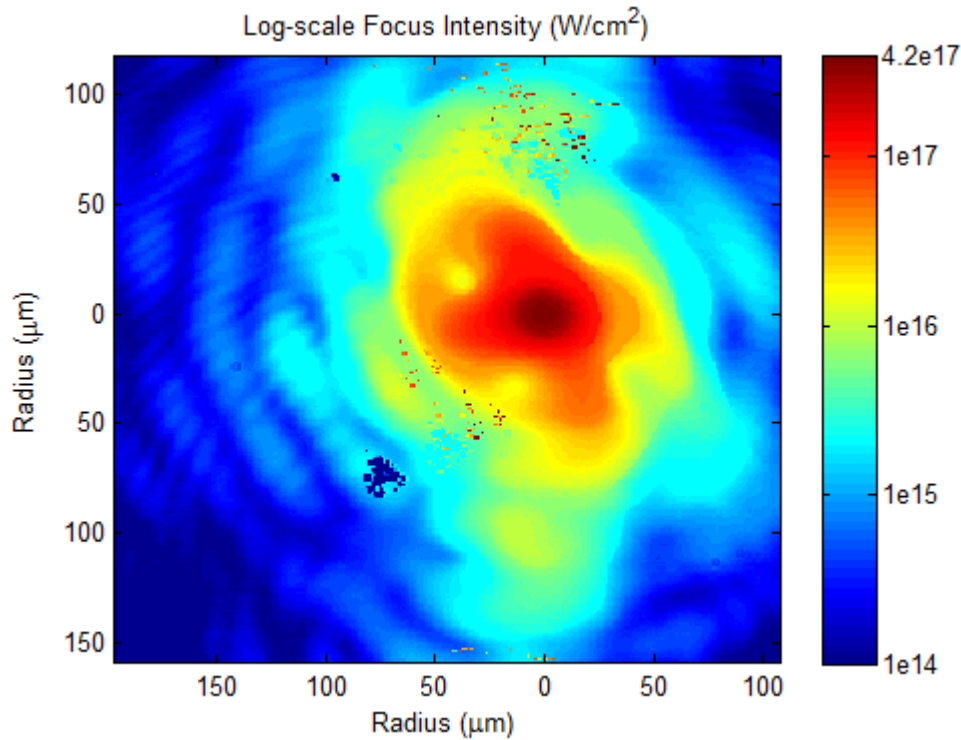
Figure 45.   Image of the focus showing the significant spatial wings.

Now, let's compare this to argon gas at the same backing pressure. As mentioned, the difference here will be that argon will form clusters of moderate size as opposed to

the helium being just monomer gas. The difference in the plasma evolution even on this time-scale is striking. Figure 46 shows an interferogram of argon plasma at the same time as the first helium interferogram in Figure 44, as well as the measured electron density. Of course, argon has many more ionization levels than helium, which accounts for the higher overall electron density. However, the plasma is nearly twice the size. This is due to the clusters, as explained in Chapter 2. The electrons ionized by the laser inside the clusters can be heated to energies of many keV, even up to and beyond the ponderomotive potential of the laser. It would seem, then, that these hot electrons are causing the plasma to expand very rapidly.
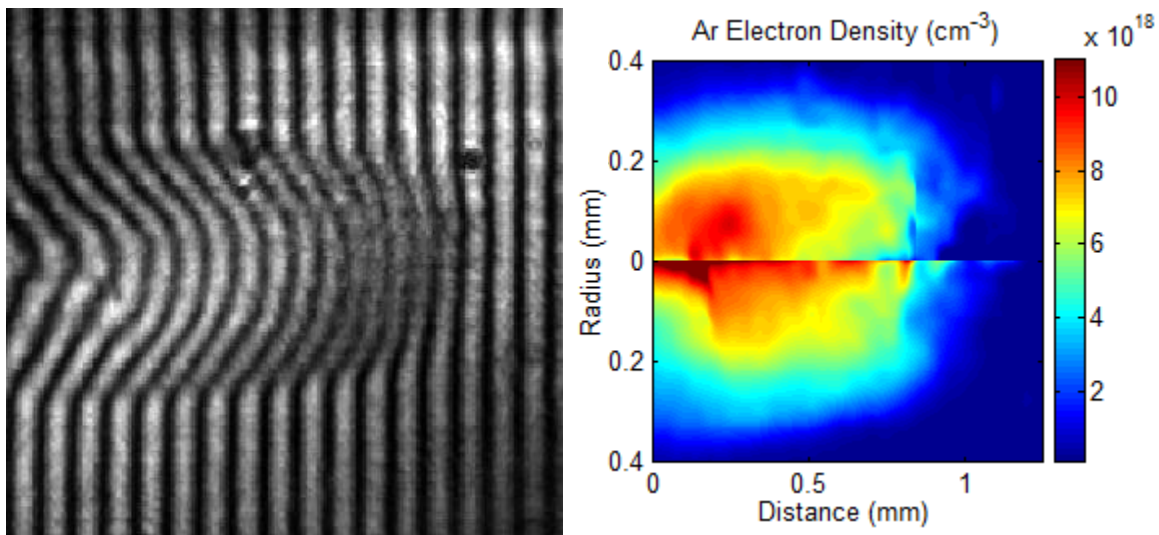
Figure 46.   Interferogram of argon plasma and retrieved electron density.

It is also noticeable that the plasma width varies as a function of z, which is the laser axis. As will be seen later, the plasma width at a delay of 5-10 ps, when the laser is outside the region being observed, is quite uniform. In addition, the Rayleigh length of the laser in these experiments was 2.5 mm, so variations of the laser spatial profile will be minimal. We can take advantage of this to introduce another way of analyzing this data. By converting the spatial scale of the laser axis to a temporal scale, we can then view this image as a time-resolved measurement of the plasma expansion on a sub-picosecond time-scale. Since the laser pulse is observed to travel across the observation region at

approximately *c* (within the accuracy of the delay stage used, and accounting for probable movements of optics due to vibrations), we can simply divide the spatial scale by *c* to obtain the temporal scale. The zero point along this axis could then be defined as the location of peak intensity of the laser. Determination of this point can be tricky, but the helium data above provides a clue for how to find it. On the screen, the iso-intensity contours of the laser pulse could be thought of as ellipses, with peak intensity obviously at the center of the ellipse. Once again, while the temporal FWHM of the compressed pulse is about 115 fs, it is apparent that the lower intensity rising edge, down to a level of $\sim 10^{14}$ W/cm^2, is noticeably larger than one might expect, about 300 fs. If we look at an electron density contour of the plasma near the outer radius, for example, 1×10^{18} cm^{-3}, we can see the contour takes on a half-elliptical shape where the laser is and then quickly flattens out in the "wake" behind the pulse. Figure 47 shows what this would imply in the helium data from before. It would seem, then, that looking at this contour can tell us where the peak intensity of the laser is. In the case of argon, peak intensity would be roughly where the plasma has reached the 200 µm radial width, or about 300 fs/100 µm
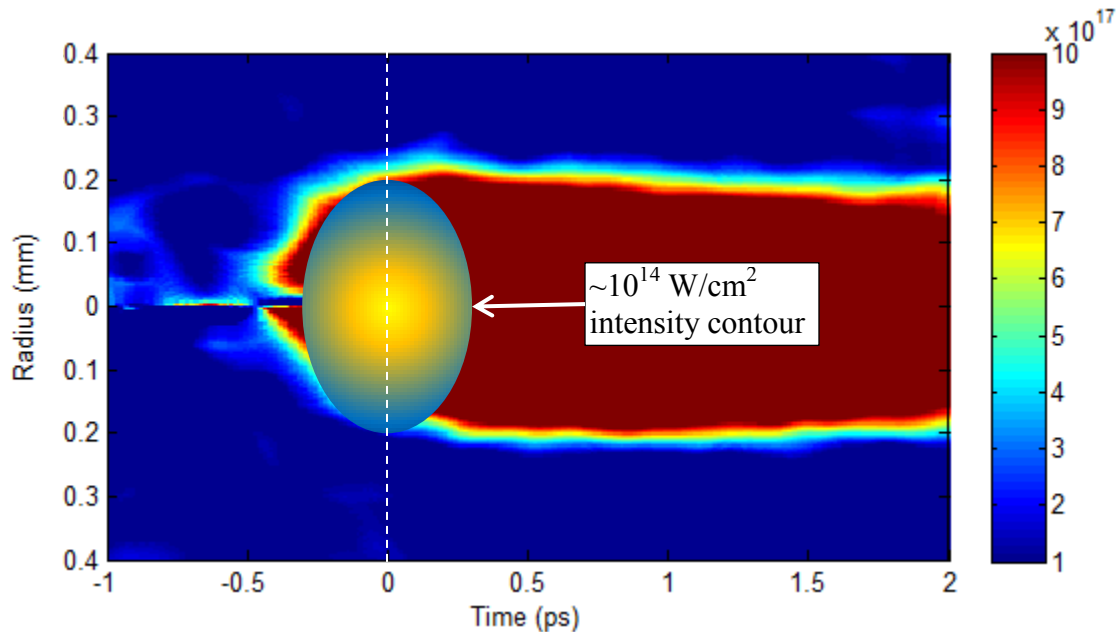
Figure 47.   Plot of helium electron density with an overlaid ellipse indicating where the laser pulse is at this snapshot in time.
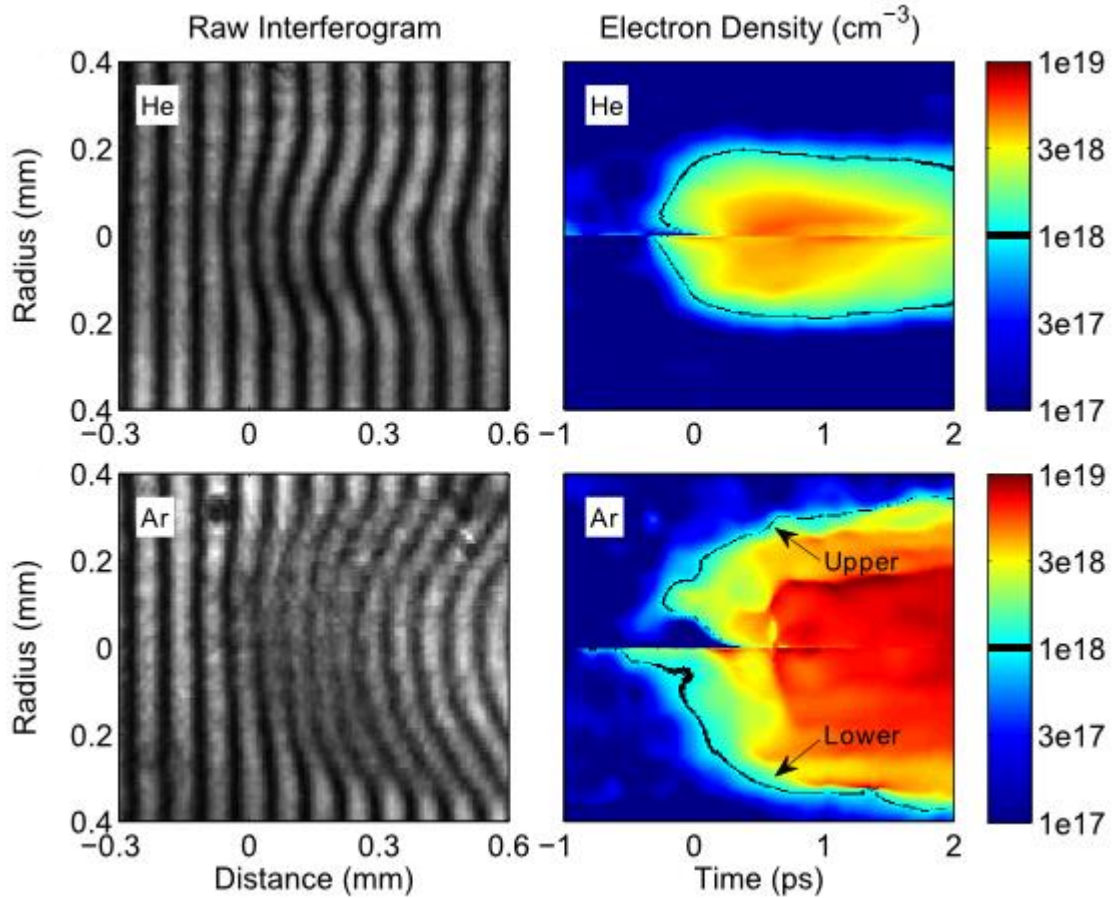
Figure 48. Direct comparison of helium and argon plasmas, with both the 10^{18} cm^{-3} contour and interior electron density clearly shown.

after the ionization has started. With the laser position known, we can then use the contour to measure an expansion velocity of the plasma as a function of time.

Figure 48 shows a helium plasma side-by-side with an argon plasma, more clearly illustrating the difference between the two plasmas. The colorscale on the electron density plots is also altered to clearly show the density contour that we are interested in tracking. The time axis on the density plots makes it clearer how the laser creates a similar shape to the plasma before t_0, but after that point, the difference between the two is remarkable. Now, let us focus on the argon data. Figure 49 shows a plot of a few 10^{18} cm^{-3} electron density contours from some analyzed argon plasmas in the first 2 ps after peak intensity of the laser. Commonly, snapshots of the plasma are taken with measured

time delays between the probe and pump laser pulses, and the average expansion velocity is calculated by measuring the radial difference between images (at a certain density level) and dividing by the time between the snapshots. Here, since we have a time history in one image, we can take the slope of the contour and measure an instantaneous velocity. The obvious advantage of this approach is that the data is in one shot, as opposed to using many snapshots and relying on the laser and gas jet being reasonably reproducible. Since the contour is made up of discrete points where $\Delta r / \Delta t$ will be either 0 or c (the pixels are nearly square), fitting a curve to the points will produce a more realistic measurement of the velocity. Figure 49 also shows the velocities of these contours. During the first couple hundred fs, the speed is often measured to be higher than c, which may be due to the laser pulse since it is still in the area. However, once the laser has passed, we see that the
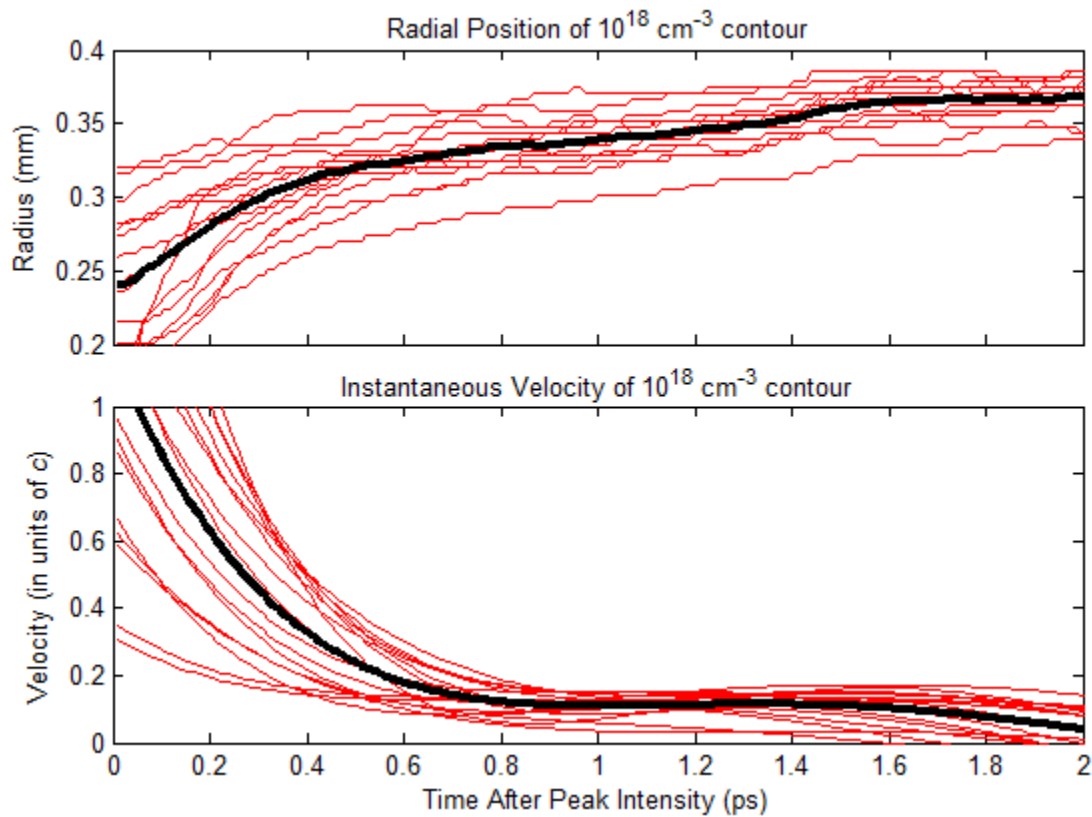
Figure 49.   Plots of radial position (top) and instantaneous velocity (bottom) of 1×10^{18} cm^{-3} electron density contours for 150 PSI argon. The black curve on each plot is the mean of the red curves.

contours are moving at speeds which are greater than $0.1c$ for over 1 ps. This is an exceptionally fast-moving front. The rather large spread of the contours is due to variance in the laser energy shot-to-shot, as well as asymmetry in the plasma on some shots.

Looking at the interior electron density, as shown in Figure 46 and Figure 48, we see that the density is not decreasing at all, and actually appears to be increasing. This observation leads to the conclusion that the plasma is not only expanding, as the increase in volume would lead to a subsequent drop in the density, but it is in fact ionizing the surrounding gas and clusters. So, we can think of this rapidly expanding front as an ionization wave, similar to what has been observed previously [73,74]. However, the wave observed here is directly measured to be at least as fast as the inferred, but not directly measured, velocity reported in Ref. 74. In addition, the observed increase in electron density can be explained by the fact that clusters, especially those which are ionized at lower intensities, will disassemble on a time-scale of picoseconds [75]. So initially, the interior electron density of the cluster is above the critical density described in Section 4.3.1, which means the probe light will not "measure" the electron density inside the clusters. Since the gas jet does not output clusters of just one size, but instead a distribution of sizes as well as a significant fraction of monomer gas [76], the density measured during the laser ionization is most likely only the contribution of gas and small clusters. As the larger clusters disassemble, their electron density will decrease and eventually drop under the critical density of the probe, which will result in measuring higher overall density in the plasma. Figure 50 shows this very clearly. Lineouts of the electron density of the argon plasma from Figure 48 are shown, with each lineout at a different time relative to when the peak intensity of the laser is expected to be (defined as 0 ps). The noticeable growth of the interior density, as well as the expansion radially, make the conclusions drawn in this section more robust.

An obvious question to ask is whether this velocity measurement is only observed at that specific electron density contour. The answer is that it is not, which is shown in Figure 51. Four different contour levels were selected, and the resulting velocity for each

contour is plotted. We can see that, with contours plus or minus a factor of two from the original 10^{18} cm^{-3} contour, the velocities recovered are in quite good agreement after 1 ps.
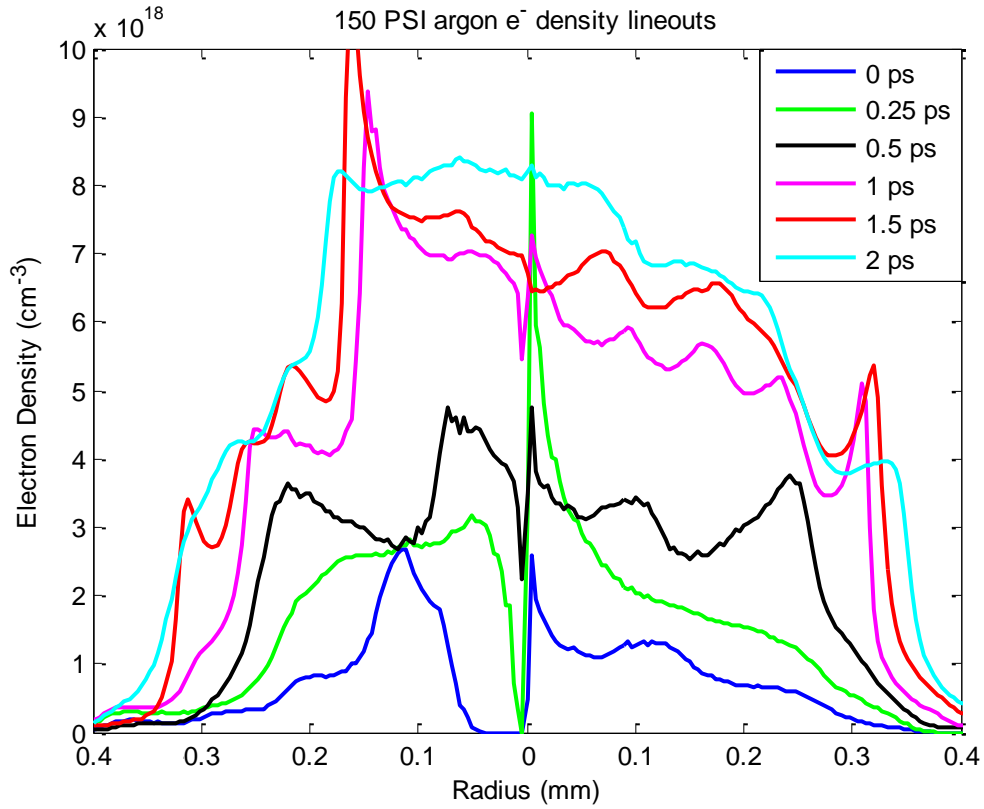
Figure 50.   Plot of lineouts of the argon plasma shown in Figure 48 at different times.
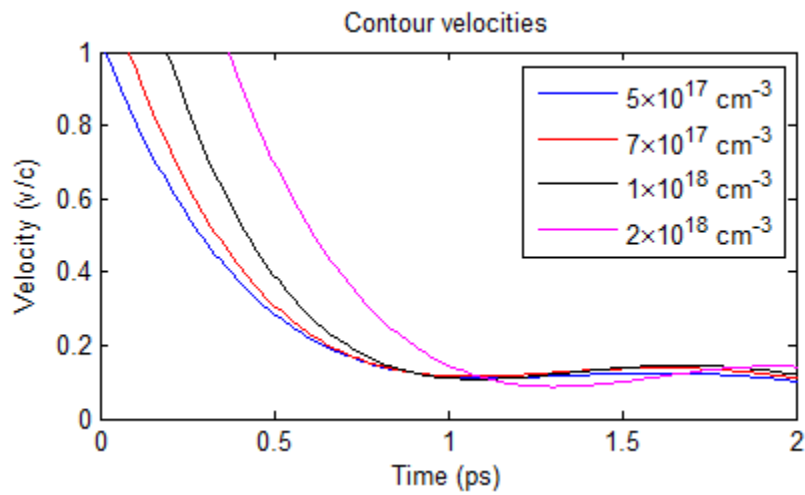
Figure 51.   Plot comparing the velocities for different contour levels of electron density.

It is worth noting that above about 3×10^{18} cm^{-3}, the velocities measured do not agree as well, but this can be attributed somewhat to the fact that it takes a bit of time for the overall electron density to reach that level. In addition, for reasons which will become clearer as we delve into the physics of this ionization wave, since these densities correspond to greater than $Z = 1$ ionization of the atoms, it is not surprising that the velocities for those higher level contours would not agree with the lower level contours.

Unfortunately, very little data of argon at 150 PSI was taken, especially in this early time regime. However, more analysis can be performed on argon data at 100 PSI, of which there is much more data. Here, we will perform the instantaneous velocity analysis as before, and we will compare this to the more conventional method of taking snapshots with known time separation. Also, since the backing pressure is lower, we might expect to see some differences in the behavior of the ionization wave.
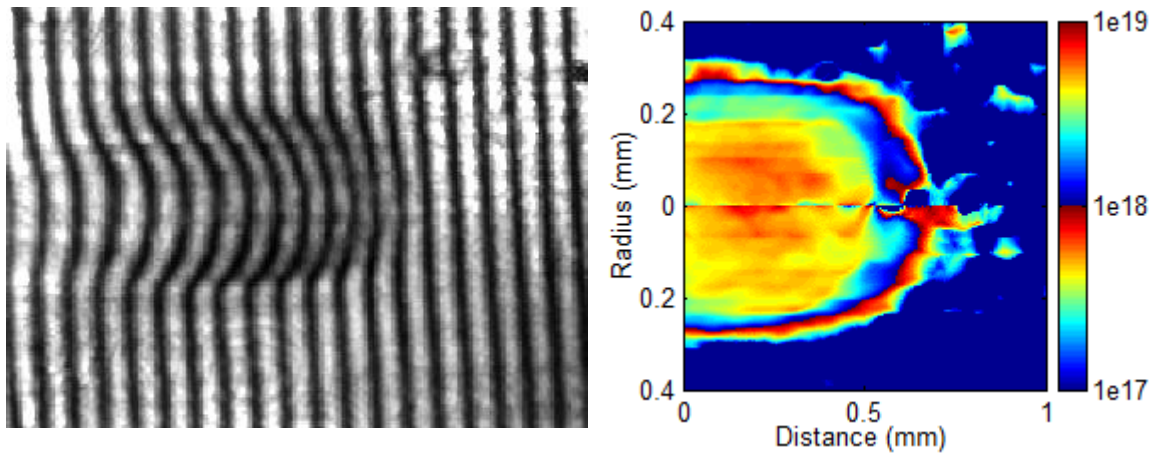
Figure 52. Interferogram and retrieved electron density for 100 PSI argon.

Figure 52 shows a sample interferogram of the lower pressure argon plasma, as well as the extracted electron density. First, we notice that the radial size of the plasma is somewhat smaller than the plasma with higher backing pressure, which implies that the ionization wave, for whatever reason, does not propagate as far. Figure 53 shows a plot of a few 10^{18} cm^{-3} electron density contours for different snapshots, as well as the measured instantaneous velocity of these contours. Figure 54 displays a direct comparison of the results for the two pressures of argon, which clearly shows that the ionization wave for

100 PSI argon does not travel as far radially, and the velocity of the waves, while still fast, are somewhat slower than the waves observed for 150 PSI argon.
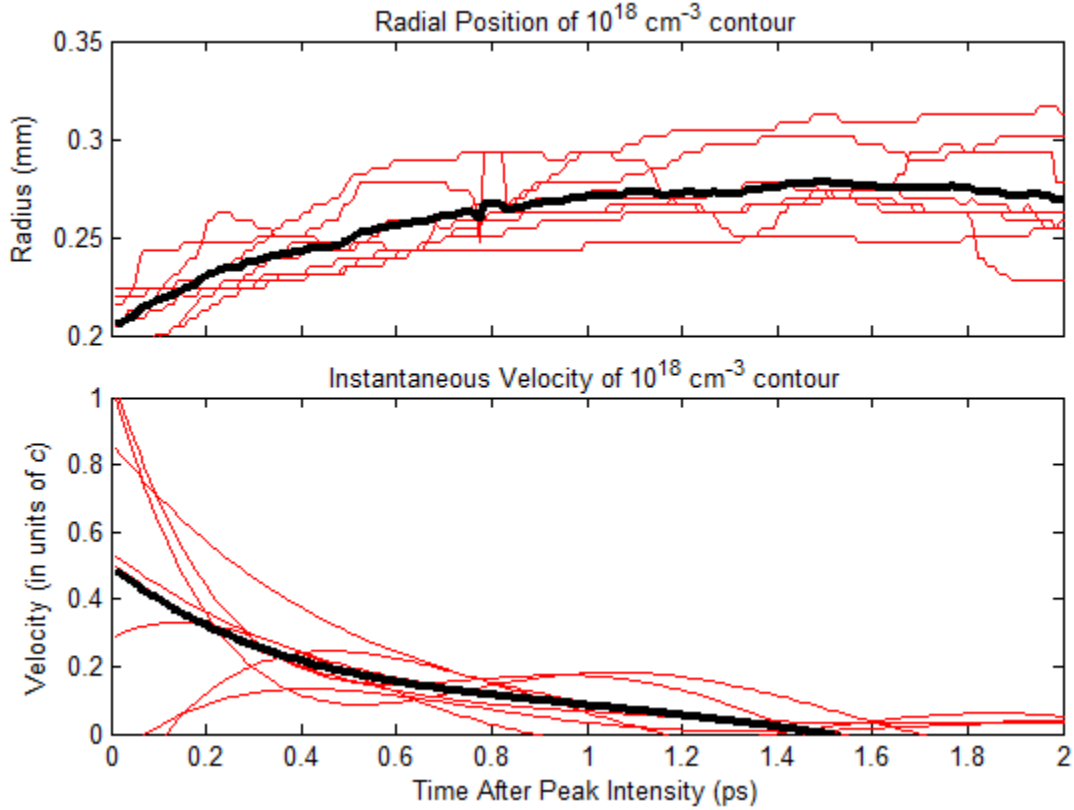
Figure 53.   Plots of radial position (top) and instantaneous velocity (bottom) of 1×10^{18} cm^{-3} electron density contours for 100 PSI argon. The black curve on each plot is the mean of the red curves. The extremely low (or negative) velocity curves near t = 0 are not real – they are artifacts of the curve fit.

Now, let us compare our instantaneous velocity measurements with the usual method of using snapshots with different pump-probe delays. Figure 55 shows a series of 10^{18} cm^{-3} electron density contours for three plasmas, each separated by 1 ps. Taking the difference of the contours and dividing by the time between them will give the average velocity of the expansion along each point of those contours. The result of this calculation is also shown in Figure 55. Indeed, we see that this method gives a result which is quite similar to the instantaneous velocity method. This lends some validity to the method, as it would raise some questions if the two methods gave differing results.
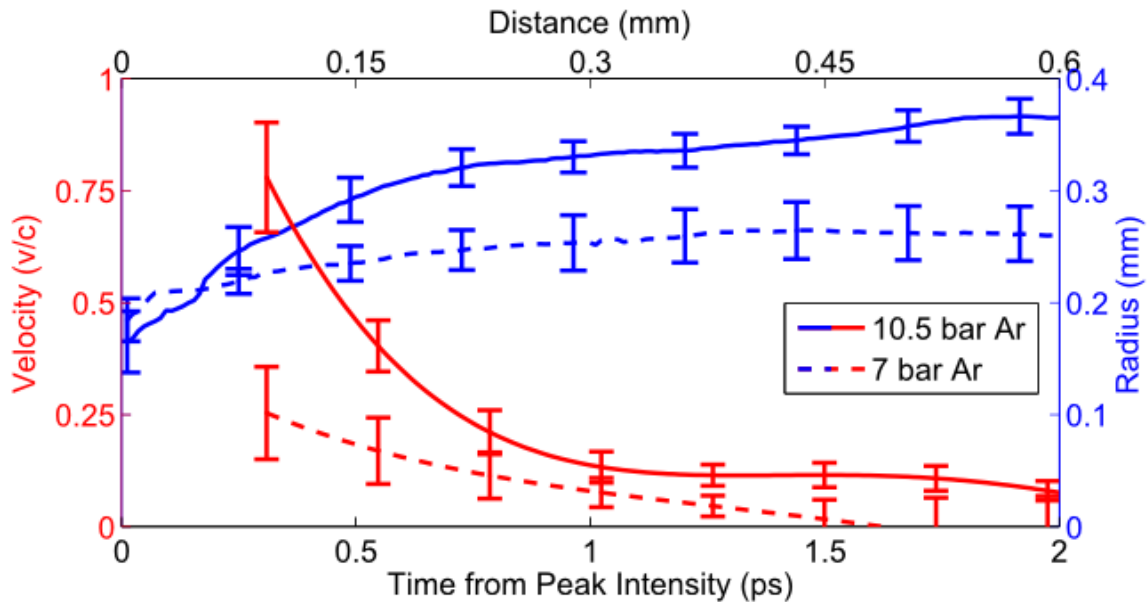
Figure 54.   Direct comparison of mean radial contours and instantaneous velocities for 100 PSI and 150 PSI argon. The velocity curves start after the approximate end of the laser pulse (see Figure 47).

Before we move on to trying to understand the physics of what is causing this ionization wave, as well as its remarkable speed, a few remarks on the overall ionization in the plasma will be made. As mentioned earlier in this section, the average gas density where the plasma is located is about 3×10^{18} cm^{-3} (for 150 PSI). Comparing this to the electron density, we can give an average Z of the plasma, which we see to be only about 3-4 at most. Many results, experimental and theoretical, have discussed the fact that clusters can be ionized to very high levels, so we might question why the ionization level here seems so low. First, it is quite likely that some large clusters are still above critical density after 2 ps. Also, the volume of high intensity, which could be considered to be above 10^{16} W/cm^2, is rather small, only about 50 μm radius. So, it is very likely that clusters and atoms in the center of the plasma are ionized to very high levels, but the outer regions in the lower intensity wings of the focus are not ionized to a very high level, and so the mixing of the two results in the average Z observed. In addition, as will be seen in the next section, the ionization wave can only ionize gas to Z = 1, while its effect

89

on clusters is not as clear. This explains the low electron density in the regions where the wave has propagated.
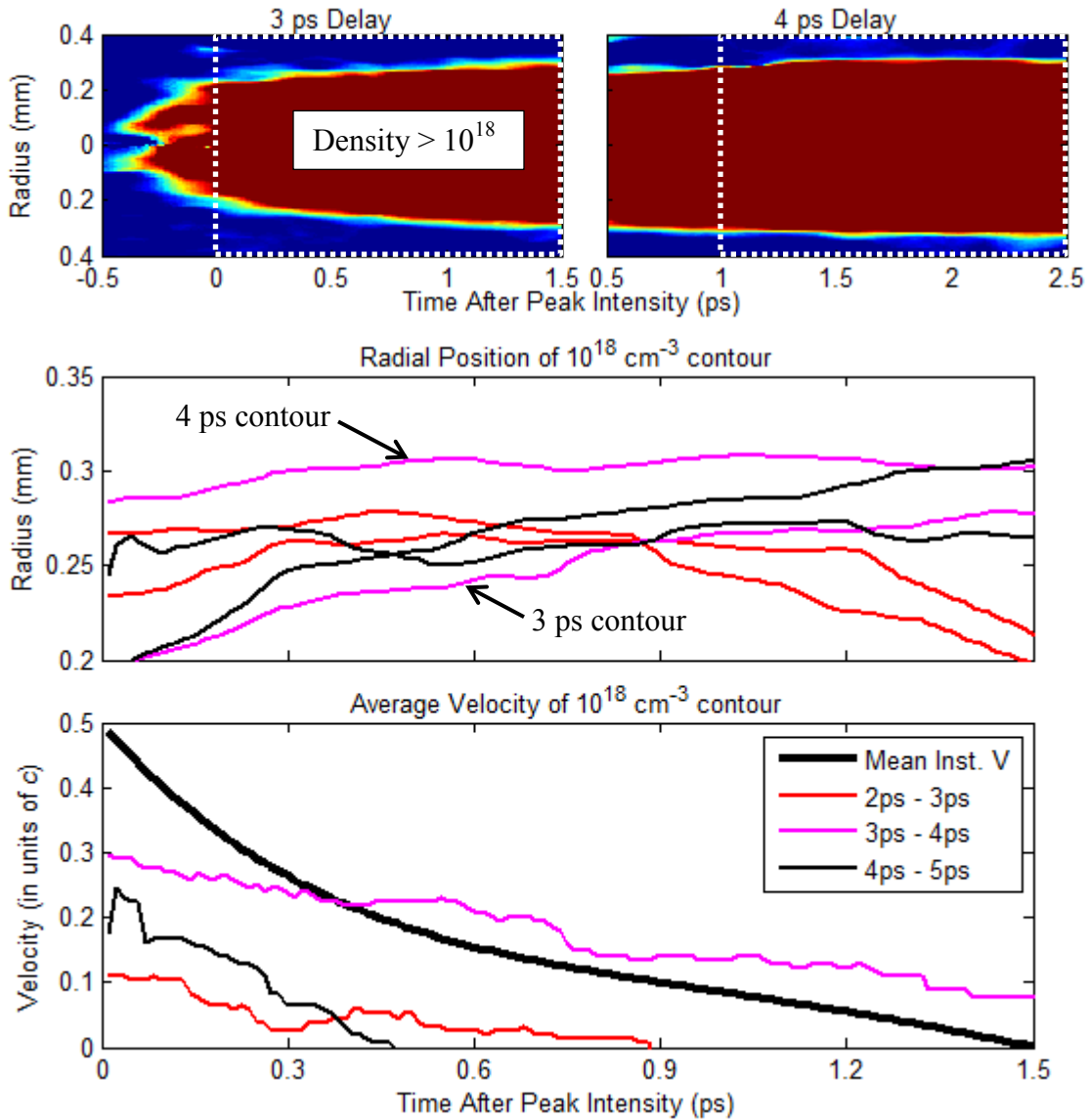
Figure 55. Plots of 10^{18} cm^{-3} contours separated by 1 ps, along with the two snapshots (top) which correspond to the magenta curves in the plots. The curves in the middle plot represent the mean contour of both "edges" of the plasma in the snapshot. The thick black curve in the bottom plot is the same line from Figure 53. The white dashed boxes show the area represented in the plots.

5.2. SIMULATION RESULTS

In order to explain what could cause the ionization wave described in the previous section, we first needed to get a feel for the basic parameters of the experiment, as well as see what possible explanations can be ruled out. First, suppose that this ionization wave was caused by free streaming electrons, and the ionization that we suspect is happening is caused by impact ionization. The thermal energy these electrons would need to travel at a speed comparable to the wave speed, about $0.5c$ maximum for 150 psi argon, would be given by

$$kT_e = m_e v_{Te}^2/2 \tag{5.6}$$

where k is Boltzmann's constant, which gives an energy of 64 keV. When we compare this to the pondermotive potential of our laser pulse, about 53 keV as given by Equation (2.5), we see that they are on the same order. As mentioned previously, it has been demonstrated theoretically and experimentally that lasers interacting with clusters can generate electrons with energies much higher than the ponderomotive potential [31, 32, 33], and the fact that our conditions only give a slight difference gives us some confidence that this is reasonable. However, very high energy electrons are not going to have large collision frequencies because the cross section for impact ionization with neutral atoms at these energies is very small [77]. Extrapolating the cross section data from Ref. 77, and using our average gas density for 150 PSI argon, the collision time is $\tau = 1/\sigma n v \approx 13$ ps, which is much too long for the time-scale of this wave. Not only that, the Debye length for this plasma is very small,

$$\lambda_D = \sqrt{\frac{\varepsilon_0 k T_e}{n_e q^2}} \approx 2 \ \mu\text{m} \tag{5.7}$$

which means that the electrons can't really "free stream" out of the plasma because of the charge separation which would result. So, collisional ionization by electrons does not appear to be the answer. However, a second hypothesis can be built using the statement about charge separation related to the Debye length.

91
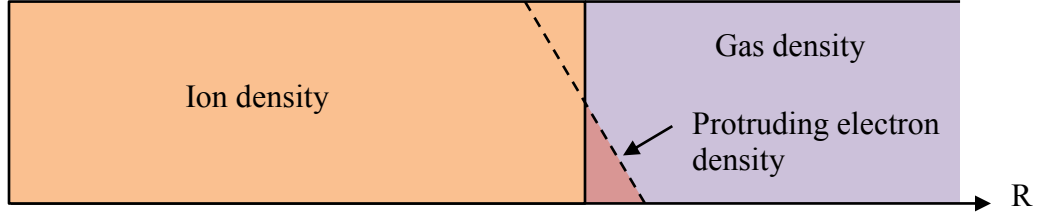
Figure 56.   View of the radial edge of the plasma, showing some hot electrons extending out into the surrounding gas.

When the clusters are ionized by the laser, the hot electrons will try to escape the plasma, causing some electrons to extend outside the interior ion density of the plasma. The situation can be visualized by looking at Figure 56. The charge separation created by this situation will give rise to an electric field at the boundary of the plasma. This electric field is estimated by

$$E = -\nabla\Phi = -\frac{\Delta\Phi}{\Delta r} \propto -\frac{\Delta\Phi}{\lambda_D} \qquad (5.8)$$

where Φ is the electric potential and λ_D is the Debye length. On the other hand, the fact that the electrons are confined implies that

$$kT_e \propto q\Delta\Phi \qquad (5.9)$$

Combining Equations (5.7-9), we see that

$$E \propto -\frac{kT_e}{q}\sqrt{\frac{n_e q^2}{\varepsilon_0 kT_e}} \propto \sqrt{n_e kT_e} \qquad (5.10)$$

which says the electric field is proportional to the energy density of the electrons which create it. If this electric field is strong enough, the atoms outside the plasma that overlap with the protruding electron density can be ionized via the tunnel ionization mechanism described in Section 2.1.2. The ionization time for this process is very short, roughly 10 fs for a field strength of 6×10^8 V/cm. Since all the atoms in the sheath exposed to this field would be ionized at a similar rate, the wave will move at a speed given roughly by λ_D/τ_{ADK}, which comes out to be about $0.6c$. The fact that this is about the speed of the observed ionization wave means that this explanation could be the answer.

92

However, there are a couple of problems with this hypothesis. Looking again at Equation (2.9), the ionization rate depends exponentially on the strength of the electric field. This means that as the wave expands, the density would drop as $1/r^2$ since there is no additional energy input to maintain the interior electron density, and the electric field would quickly drop below the level needed for rapid ionization. For example, decreasing the field strength above by a factor of two increases the ionization time from 10 fs to 10 ps. In addition, Figure 57 shows that (initially) the electric field is radially positive and only at the boundary, so the entire plasma can be viewed as a potential well. This means that the hot electrons most likely would not stay near the boundary long, which would also affect the field strength. So, while this hypothesis does show promise as a possible explanation, there is something missing that needs to be found.

We used a Particle-In-Cell (PIC) code to model what is happening in the plasma. The code we used, with help from Dr. Alexey Arefiev, was the Plasma Simulation Code [78], with 1D simulations run on a desktop computer and 2D simulations run on the LONESTAR high performance computing system at the Texas Advanced Computing Center. As a first step, we performed 2D simulations of a cylindrical plasma filament with a hot electron population that was allowed to expand into surrounding gas. Since the plasma we measured was very large, we scaled down the size (to save computing time) such that the plasma radius was initialized to be 50 μm. Plots of the electron density and radial electric field very early in time are shown in Figure 57. The gas used was Ar with density 7×10^{18} cm^{-3}, and the plasma was initially singly ionized. In simulations where we set the plasma to have higher Z, sharp discontinuities in the electron density would develop at locations where Z would change from 1 to 2, for example. The reason for this is that the strong field exists in an area of space for only a short time because of the high velocity and the small spatial extent of it ($\sim\lambda_D$), so there is insufficient time for the field to ionize atoms to $Z = 2$. Since we had no measurements of the real electron energy spectrum, the electron momentum distribution was set to be isotropic with a simple two temperature distribution: the "cold" electrons had momentum $p_e = 0.01m_e c$ while the "hot" electrons had momentum $p_e = m_e c$. In order to simulate the different backing

pressures of the gas jet in the experiment, which in essence determined how many hot electrons there would be, we used four test cases where the hot component made up 10%, 30%, 50%, and 70% of the initial population. Finally, as our estimates above described, collisional ionization processes are negligible in the time frame of this phenomenon, so we turned off the collisional processes in the code so that the atoms can only be ionized through the tunneling ionization mechanism and to significantly speed up the simulations.
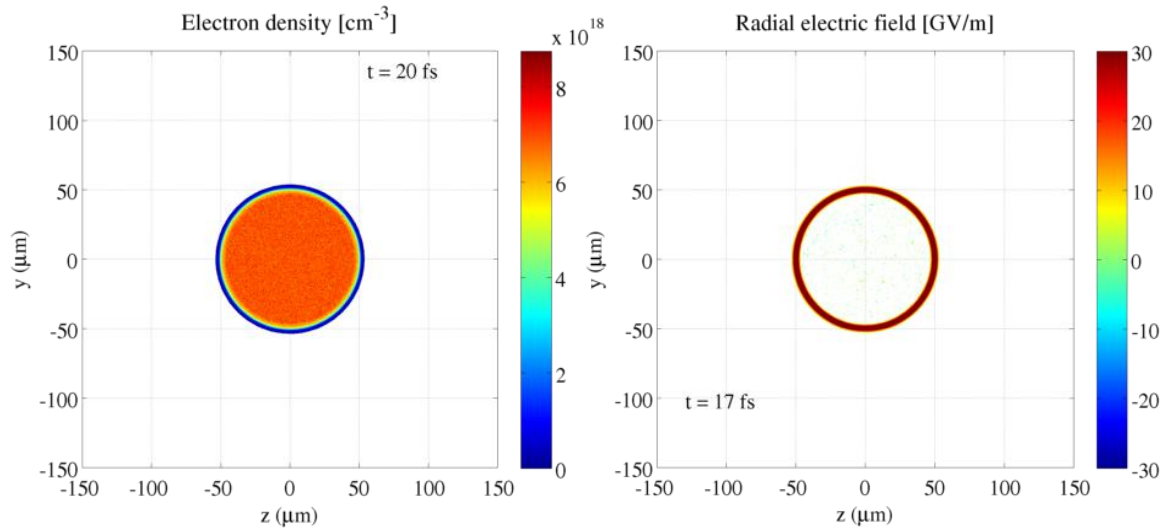
Figure 57.   Plots of the electron density and radial electric field at a very early snapshot in the 2D PIC simulations.

For ease of comparison, let us examine the results of the 10% e_{hot} case versus the 70% e_{hot} case. Figure 58 plots the electron density of the two plasmas at an early time (500 fs) and a late time (1.6 ps). We can see that, in the early stages, the two plasmas have expanded in a similar way, but when we go much later in time, the plasma with the higher number of hot electrons has expanded much farther radially, about twice the initial radial size. In addition, in the later snapshot we see the presence of what could be described as "fingers", indicating that the radial expansion is not cylindrically symmetric and has some sort of instabilities associated with it. A plausible explanation for these features will be described later. Since we have the electron density as a function of time (with many more time steps than are shown here), we can plot both the radial position and the expansion velocity of the plasma boundary very easily, which is shown in Figure

94

59. As expected, the plasmas with higher numbers of hot electrons expand faster as well as for longer periods of time. For the 70% case, the discrepancy between the maximum and angle-averaged curves is a result of the "fingers" mentioned above. The scale of the simulated data is similar to the results measured experimentally, so this tells us that our hypothesis used to generate the simulation parameters does appear to be valid. Of course, the electron density does not really explain what is causing this phenomenon, so let us examine other parameters from this simulation.
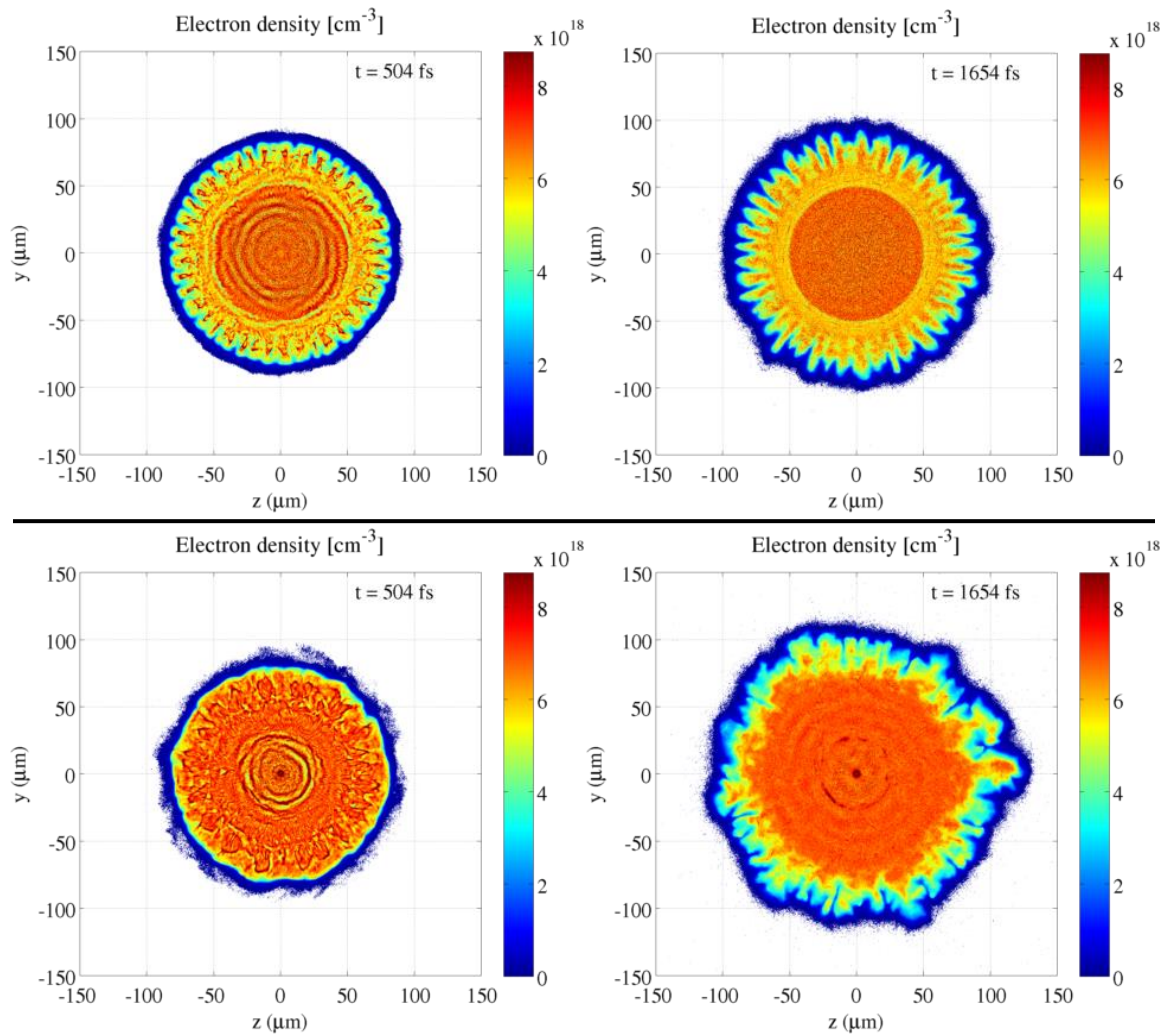
Figure 58.   Simulated electron density plots for plasma with a hot electron percentage of 10% (top) and 70% (bottom) at two time snapsnots. Both plasmas grow considerably in the first 500 fs, but the 10% e_{hot} plasma does not grow much over the next picosecond, whereas the 70% e_{hot} plasma continues to grow.
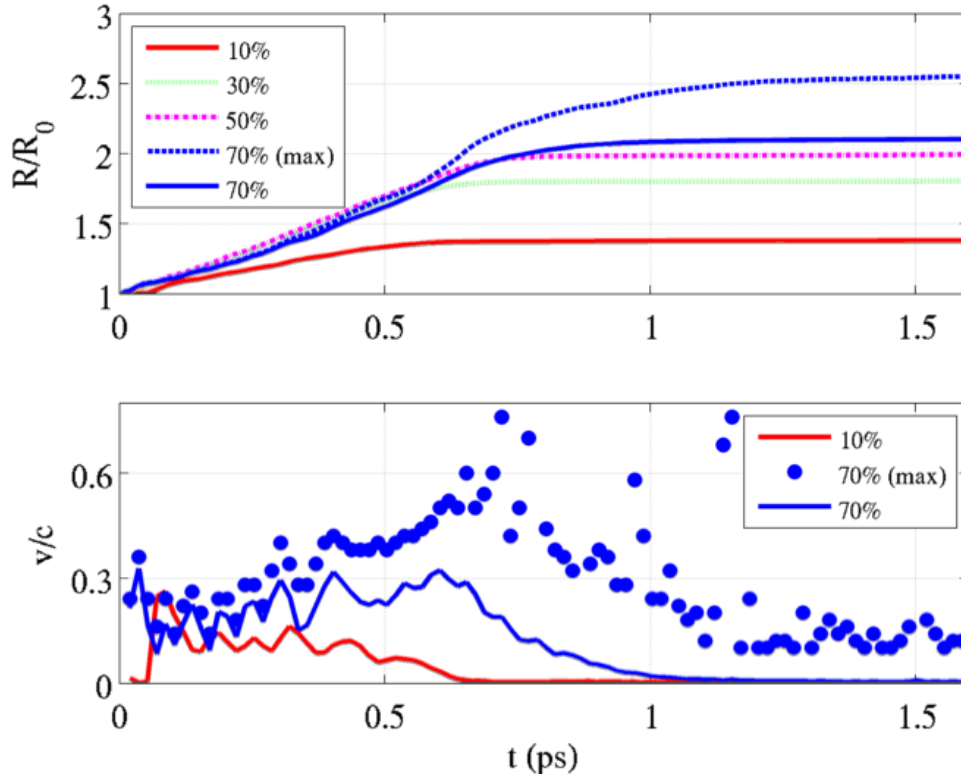
Figure 59.   Plots of the normalized angle-averaged radius (top) and velocity (bottom) of the ionization front. Also shown are the maximum radius and velocity for the 70% case to illustrate the non-uniformity of the 2D expansion.

Since it is the sheath electric field of the plasma which is ionizing the gas, it would make sense to plot the radial electric field. Figure 60 plots the radial electric field for the two plasmas at the same time steps in Figure 58. Unsurprisingly, early in time we see a very strong electric field at the boundary of the plasma. The field strength exceeds 30 GV/m, which is plenty strong to ionize the gas through tunnel ionization. What is interesting, however, is that immediately inside this strong radial field (which is pointed radially outward) is an electric field of similar magnitude, but pointed radially inward. This observation implies that a potential well exists near the boundary. If it is the case that the hot electrons are the source of the strong sheath field, then it could be that this potential well is confining them near the boundary of the plasma, which would certainly allow the field strength to be maintained during the 1-2 ps of expansion. It is not clear, however, why or how this potential well would confine the hot electrons but let the

ionized electrons pass through it into the plasma interior (notice there is no dense ring around the plasma in the electron density plots of Figure 58). The other pertinent question is how this potential well maintained during the expansion?
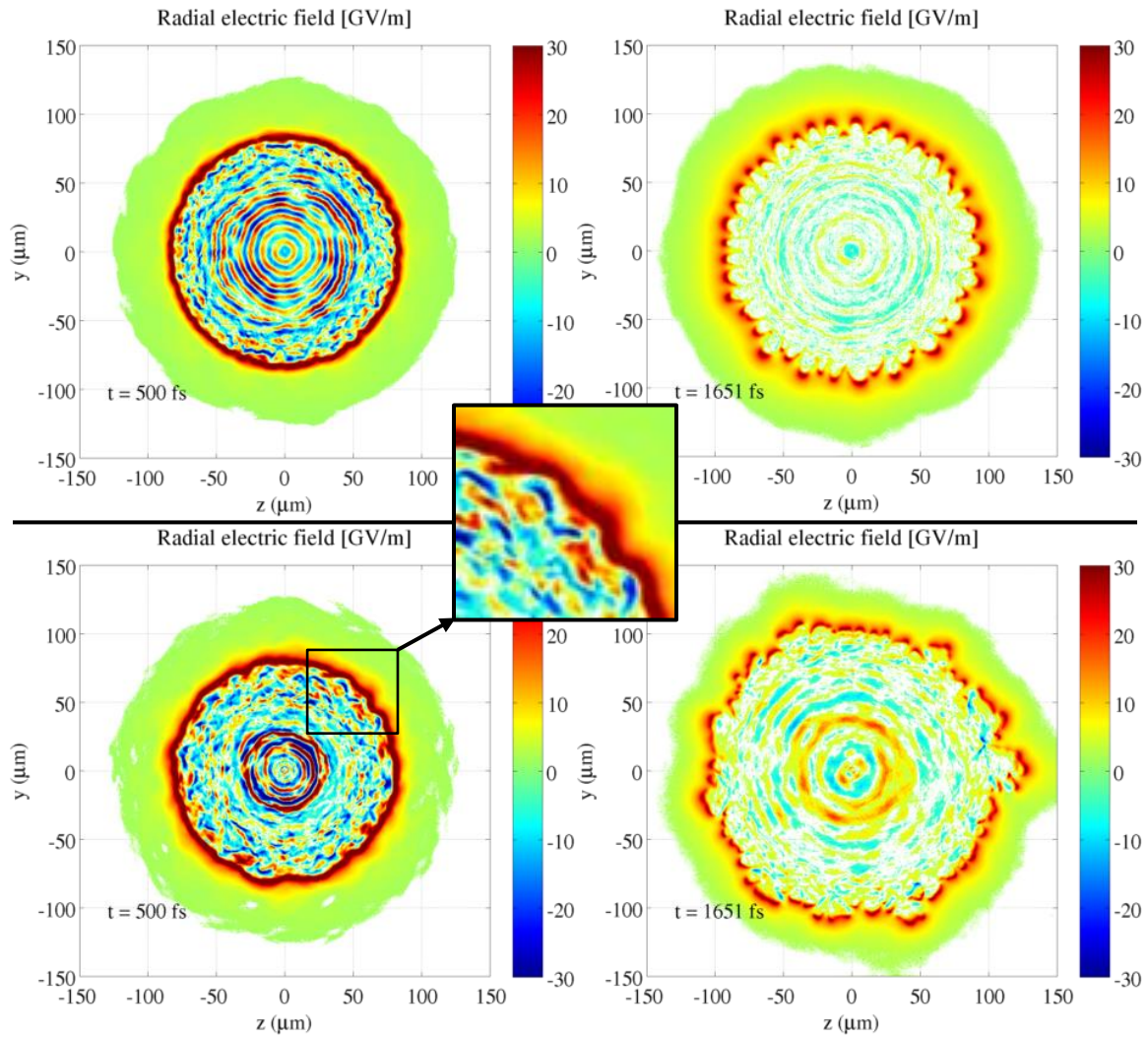
Figure 60.   Simulated radial electric field for plasma with a hot electron percentage of 10% (top) and 70% (bottom) at two time snapsnots. The center inset highlights the field structure that traps the hot electrons near the boundary

In order to answer these questions, we performed 1D simulations with roughly similar initial conditions. We found that the electron phase space is better visualized using a water-bag electron distribution with cut-offs at $p_e = \pm m_e c$ as well as using hydrogen with an initial density of 3.4×10^{19} cm^{-3}. The radial edge of the plasma was set

97

at $z = 100$ μm. Figure 61 plots the electron phase-space, electric field, and electron density near the plasma boundary after the boundary has expanded about 30 μm from the initial position. We see the similar electric field structure to what was observed in the 2D case as well as a high number of energetic electrons trapped in the potential well created by the field. Interestingly, the phase-space plot shows that while electrons which originated from the plasma are trapped in the well, the electrons which are ionized by the sheath field pass through the well and into the interior of the plasma. Once again, this seems counterintuitive to what should happen. This can be explained by examining the phase-space plot more closely. If we look at this situation in a frame moving with the ionization front (with the frame momentum indicated by the dashed line), it is clear that the electrons ionized by the field have higher momentum in this frame than the hot electrons at the ionization location. Therefore, when they are accelerated into the well and reach the other side, they have enough energy to escape. The hot electrons in the lab frame, however, are low energy in the moving frame, and consequently are confined by the well. If we imagine the "ball" of hot electrons in 1D phase-space in a 2D view, it would look like a ring at the edge of the plasma. As such, we have colloquially named this phenomenon the "ring of fire."

To address the second question from before, imagine the plasma when it is first formed. Hot electrons bunch up near the boundary and are confined by the ions they leave behind, forming the sheath field. Once the field reaches sufficient strength, atoms near the boundary are ionized, and these electrons are accelerated into the plasma by the field. At the same time, the boundary has moved since the atoms will be ionized together, and so the boundary motion begins. As the ionized electrons move away, their density drops below the background ion density as a result of flux conservation, and an oppositely directed electric field forms (labeled "trapping field" in Figure 61). In the moving frame, the ionized electrons have higher energy than the original electrons, and so this field (as the label implies) traps the original electrons. This field does begin to slow the ionized electrons, and their density spikes (seen in the electron density plot of Figure 61). This creates a new positive electric field which prevents those ionized

98
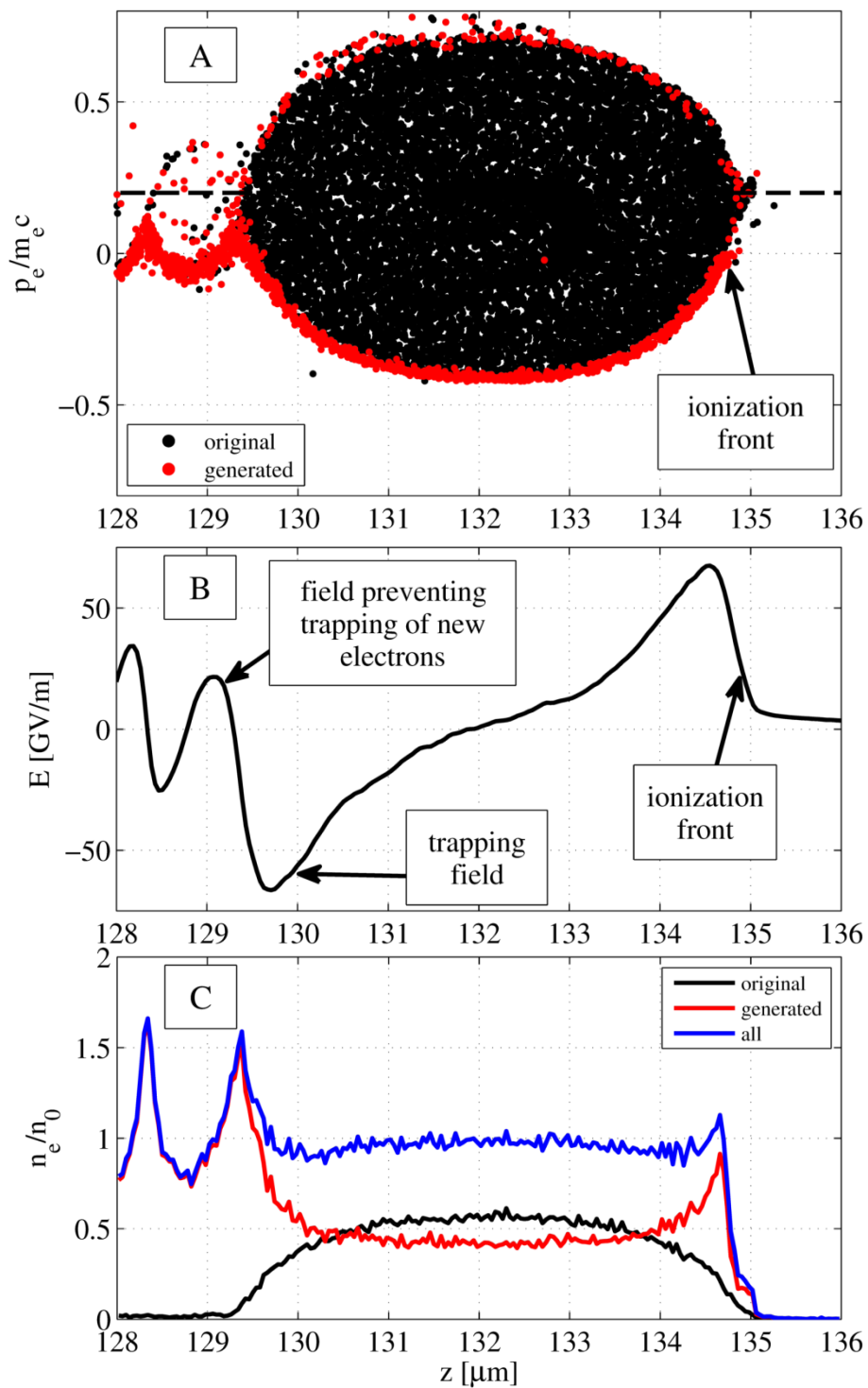
Figure 61. Snapshots of electron phase-space (A), electric field (B), and normalized electron density (C) from the 1D PIC simulation.

electrons from going back into the well. These electrons do carry away some energy from the process, and this leads to a decrease in the sheath field and the velocity of the ionization front. Once enough energy has been lost through the ionization process, the time required for the field to ionize the surrounding gas will become too long, and the ionization front will effectively stop.

Since this process is heavily dependent on the sheath field strength, which is sensitive to the energy density of the trapped electrons, it is easy to imagine that irregularities in how the electrons are spread around the ring would lead to non-uniform expansion. In addition, it is unrealistic to expect that the motion of the electrons in the ring will be purely radial, so it is very likely that there is electron motion in the azimuthal direction during the expansion. This is exactly the cause of the "fingers" mentioned before. Certain areas where a higher density of hot electrons occur will necessarily expand faster than nearby areas with a lower density, and so these higher density areas become isolated from the rest of the front. This results in these areas expanding in a quasi-1D way, which is shown in the late-time electron density plot of Figure 58. As it was noted before, this can lead to discrepancies in the measurement of the radial expansion. This is especially true in the simulation since we can observe this very easily, but it can also happen during the experiment. Figure 62 shows the probe beam traversing the plasma at a time when these "fingers" have formed. Since there is no way to predict where these will occur, it can certainly happen that on one side of the plasma, the probe measures a larger expansion because a "finger" appeared there. On the other side of the same plasma, it could also happen that fingers did not really appear (or are not at the maximum radius with respect to the probe beam direction), which would result in a smaller measured expansion. This could be an explanation for why so many of the measured interferograms were not very symmetric, especially near the boundary of the plasma.
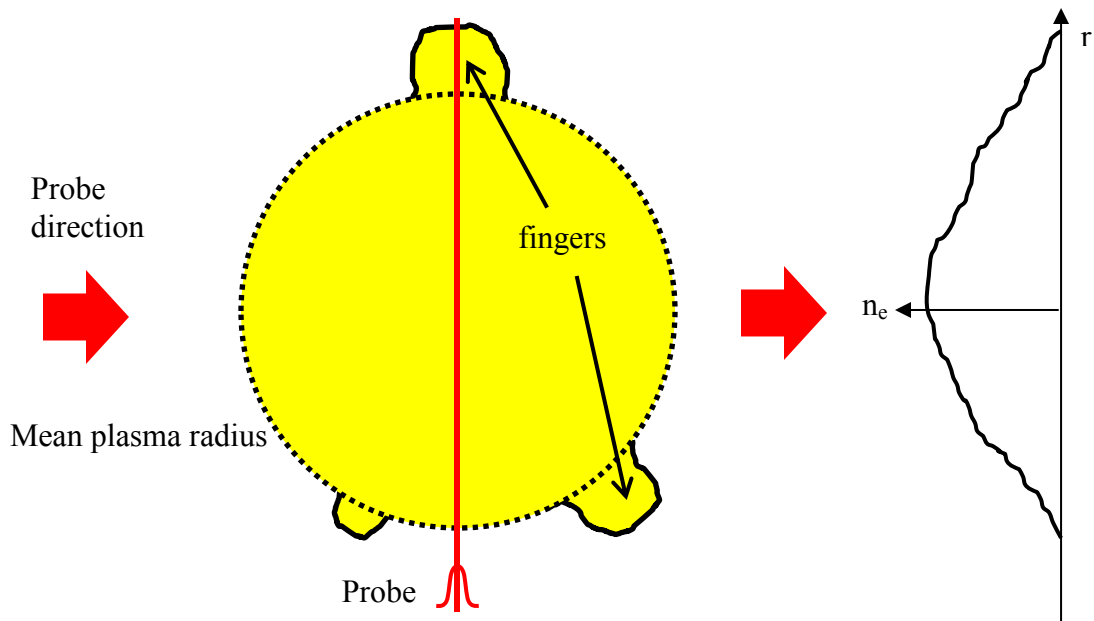
Figure 62.   Schematic view of the probe beam traversing the plasma from left to right when the quasi-1D "fingers" are present, with a representative plot of the electron density profile that would be retrieved.

Chapter 6. Plasma Expansion in an External Magnetic Field

Now that we have a better understanding of the initial conditions of the plasma, we can turn our attention to the longer time-scale behavior of the plasma with and without an external magnetic field. First, we will compare the experimental results of the two situations to see what differences are observed. Then, a simple model using the plasma transport equations presented in Chapter 2 will be used to simulate the data and explain the experimental observations.

6.1.   EXPERIMENTAL DATA

While the data in Chapter 5 was narrower in scope, the data applicable to this chapter is much broader. The gases used were argon, nitrogen, neon, and helium, and the backing pressures on the gas jet varied from 100 to 200 PSI, with very little data taken at higher pressures. Ultimately, the pressures used were a function of the fringe resolution in the 2D interferometry, as it was discovered that the fringes would often become blurred out at pressures above the range used, especially with argon. The laser parameters were the same for this data.

6.1.1. Helium, Nitrogen, and Neon Data

Before we dive into the data for these three gases, let us first discuss the expected cluster size for each gas at the pressures listed above. From Section 5.1, we know that helium will not form clusters at these pressures. The values for the constant k for neon and nitrogen are $k = 185$ [67] and $k = 528$ [79], respectively. For the two most often used backing pressures of 100 PSI and 150 PSI, the Hagena parameter for these gases is about 25,000 and 37,000 for nitrogen, and 8,500 and 13,000 for neon. While the Hagena parameters are quite large for these gases, we know that the clusters formed using these gases will be smaller than those formed using argon. Given the expectation that the clusters actually formed with argon would be quite a bit smaller than what is predicted by the various scaling equations, it is fair to assume that the clusters in these two gases will

be quite small, likely on the order of 1-2 nm radius for nitrogen and sub-nm radius for neon, and remembering that this is the mean radius expected. As will be seen, especially when comparing these two gases with helium, this assumption appears to be valid. Also, as was implied in Section 5.1, the atomic density emitted from the jet will be the same for each gas as the values quoted for argon at the two backing pressures used.
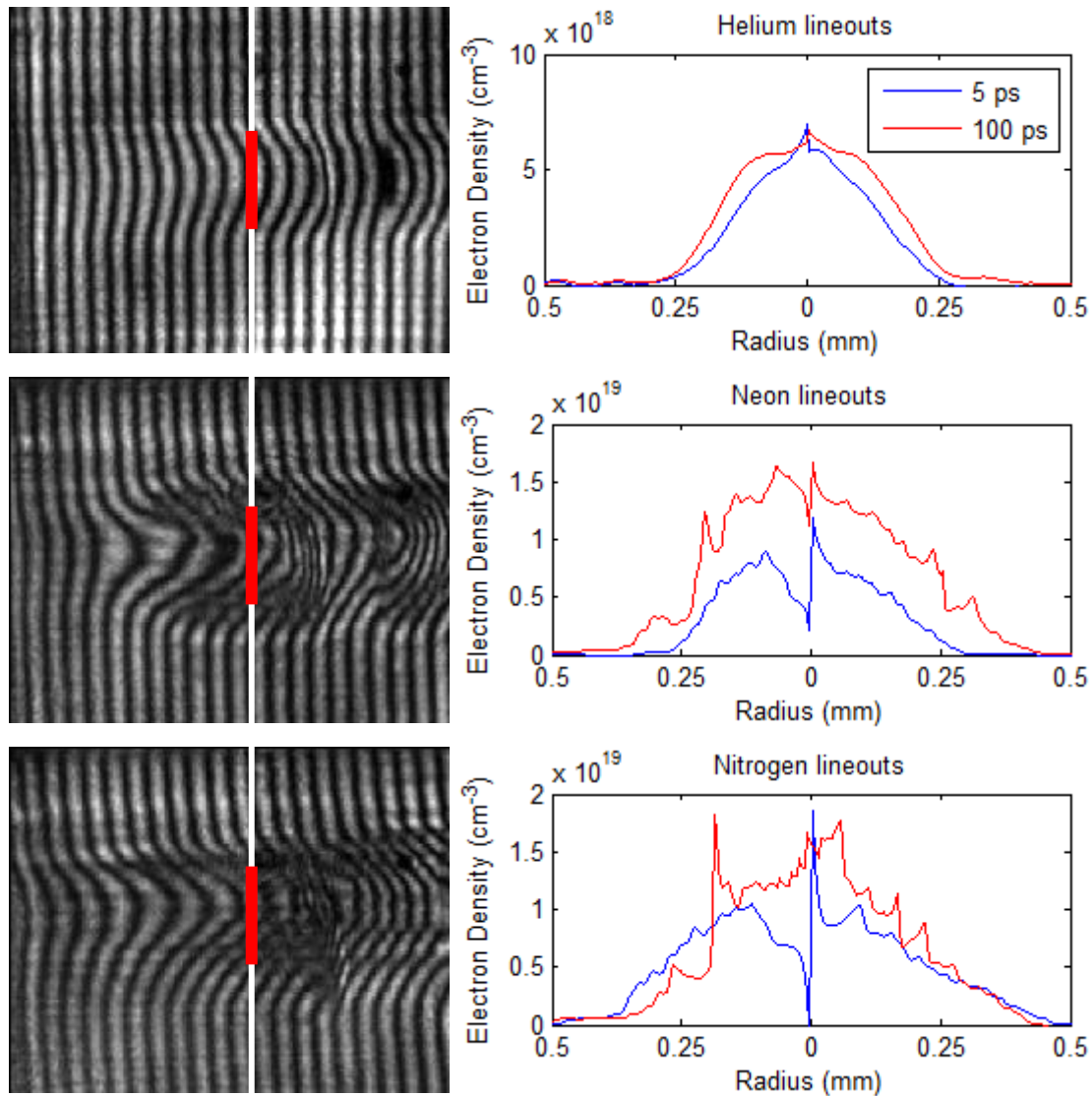
Figure 63.   Sample interferograms of He (top), Ne (middle), and N_2 (bottom) plasmas at 100 ps time delay with a red colorbar indicating the ionizing width of the laser pulse (discussed in Section 5.1). Also shown are lineouts (location given by the white line) for each plasma at time delays of 5 and 100 ps.

With this in mind, we can now get a feel for the data. Figure 63 shows a sample interferogram for each of the three gases, using backing pressure of 150 PSI and at 100 ps time delay, along with lineouts of the electron density at two time delays. These images and plots are for plasmas with no magnetic field present. First, as we saw in Chapter 5, helium is ionized by the laser with little change in the electron density over time, consistent with a laser ionizing monomer gas. Neon and nitrogen do show differences compared to helium, which indicates there are likely clusters present in the gas. Interestingly, it appears that neon is ionized somewhat similarly to helium initially, but then over time, there is noticeable growth in the electron density. Conversely, nitrogen seems to show a "ring of fire" expansion early on since the plasma width is considerably wider than the laser, but after that occurs, there is minimal change in the electron density profile. The result in nitrogen would seem to imply that the clusters are large enough that the laser produces a sufficient number of hot electrons to trigger the fast ionization effect, but the electron energy distribution is very skewed with the rest of the electrons being rather cold, resulting in minimal plasma growth later in time. The neon result, however, could imply that the small clusters cannot produce enough hot electrons for the fast ionization, and so possibly the plasma temperature is generally higher and the observed expansion is related to thermal expansion. What isn't seen here is that the neon data displayed some strange behavior, which will be seen later, so it may be tough to draw any clear conclusions from this data set.

Given the results shown in the previous figure, there is little expectation that we will see an effect of the magnetic field on these plasmas, with the exception of neon if indeed the expansion hinted at in the plot is real. We will first examine the helium data, which consisted of shots with no field and shots with a 4 T field present. Figure 64 plots the 10^{18} cm^{-3} electron density contour of the plasma as a function of time, with each of the time points having two data shots each (and consequently four contour points). As expected, we see very little difference in the width of the plasma with and without the field, at least within the error bars of the curves. An obvious question that arises is why the data points at 5 and 40 ps, and even 10 and 60 to some degree, deviate from the trend

104

of the rest of the data. The reason is that during this run, the gases were connected to the same tubing that fed the gas jet, and while efforts to vent the line when switching gases were made, sometimes it did not end up being quite good enough. In this case, argon was the gas used before this helium data, so it would appear that there was still enough argon in the line that it skewed the data on the first shots. Also, in order to help sort out problems like this, the data shots (as well as for all of the 150 PSI data sets shown in this chapter) were taken in the following order: 5 ps, 40 ps, 10 ps, 60 ps, 15 ps, 80 ps, 20 ps, 100 ps, and 30 ps, with each of the four field strengths used during each time step. Clearly, the 5 and 40 ps shots were contaminated, but after those shots, most of the contaminants had been cleared out. While I was taking the data, I noticed especially that the 5 ps shots seemed abnormal, so I went back and took more shots from 0-10 ps. The 0 T data at 5 ps represents this, clearly showing the other data points are no good.
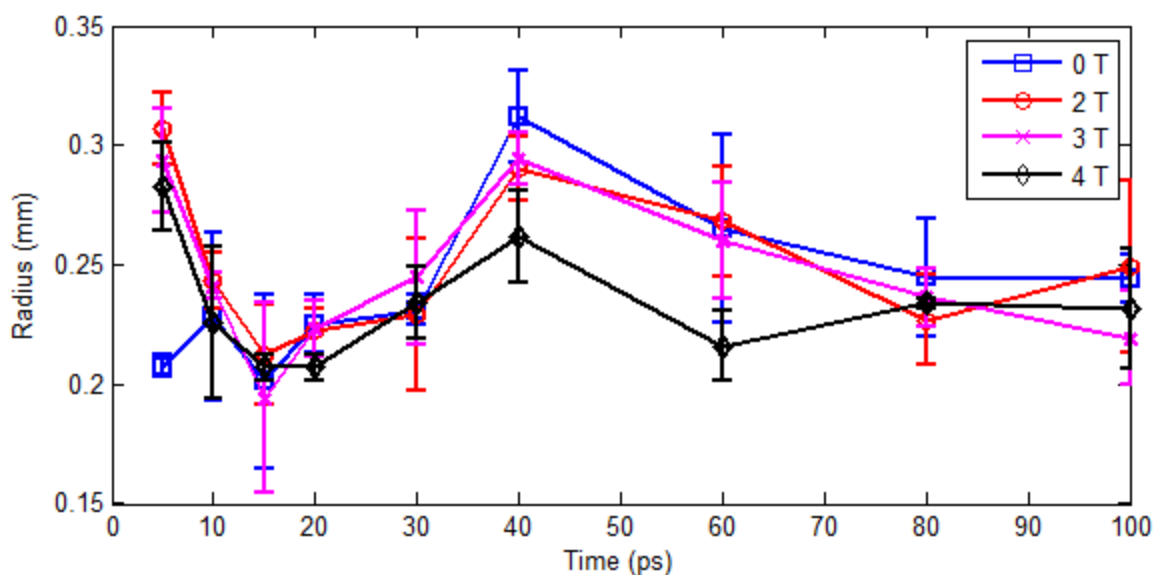
Figure 64.   Plot of the 10^{18} cm^{-3} contour as a function of time for helium at 150 PSI. Disregarding the contaminated data points, the field shows little effect.

Next, let us examine the neon data more closely. Figure 65 plots the same contour level as a function of time for neon at 150 PSI. Once again, we seem to observe two trends in the data, and so it becomes a question of which trend is correct. In this case, nitrogen had been used before switching to neon, and when I began taking the data, the

plasma was observed to get smaller later in time, which made it clear that there was still nitrogen in the line. I then started over and took the data shown below. What appears to be happening is that the reverse situation happened with neon than what happened with helium – the gas was primarily neon during the first data points, but starting with the 60 ps data, nitrogen was mixed in and so the plasma began to artificially grow. A more likely explanation would be that the laser energy started low and became higher in the later shots, but the data from the photodiode used to monitor the laser energy did not support this hypothesis – in fact, while there was dither shot to shot, the average energy was quite steady. Therefore, the gas impurity hypothesis would seem to explain the strange oscillatory nature of the plasma size. Since the "bad" data is more numerous than the good data in this set, it is hard to draw strong conclusions of what is occurring. However, it can be said that in the cleaner data points (and even most of the bad ones), the field has little effect on this plasma as well.
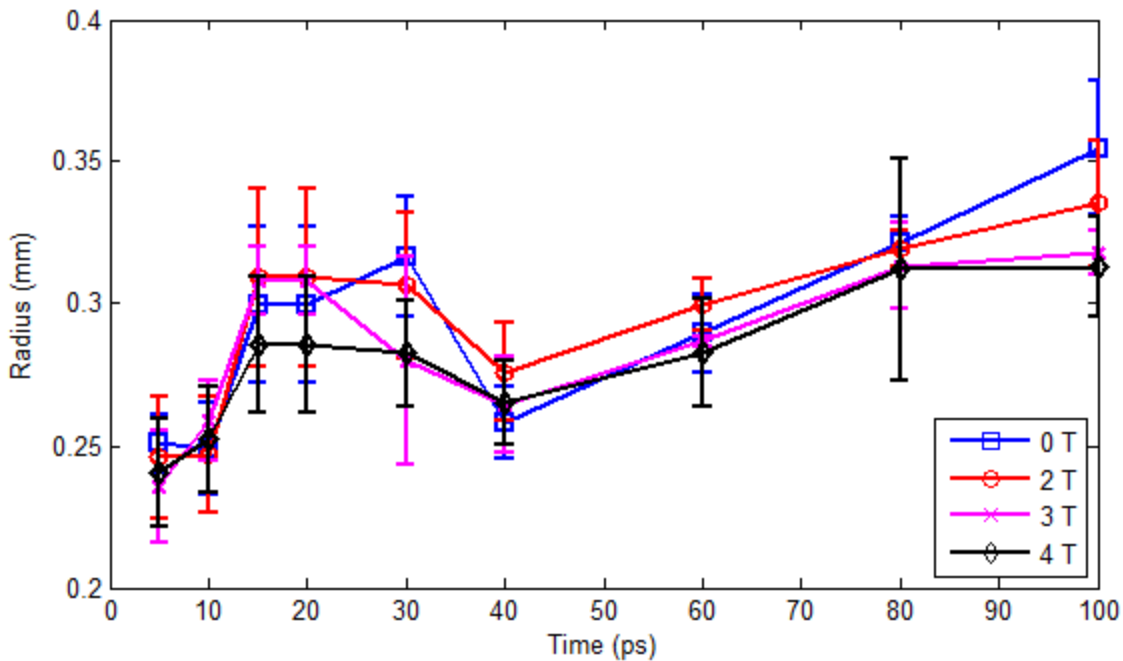
Figure 65.   Plot of the 10^{18} cm^{-3} contour as a function of time for neon at 150 PSI. Once again, the field shows little effect.

While the data for neon at 150 PSI was not very clean, data taken during the second experimental run at 100 PSI proved to be much cleaner. Much of this is because more effort was put into venting the gas lines when switching gases. Figure 66 shows the results of this data. A sample interferogram at 50 ps time delay (with no field) and a no field streakogram shows the typical size of the plasma, and the corresponding plot tracking the size of the plasma as a function of time matches what is seen in the interferogram. Clearly, neon at this pressure is almost all monomers since there is essentially no plasma expansion observed, which the streakogram also makes very clear.
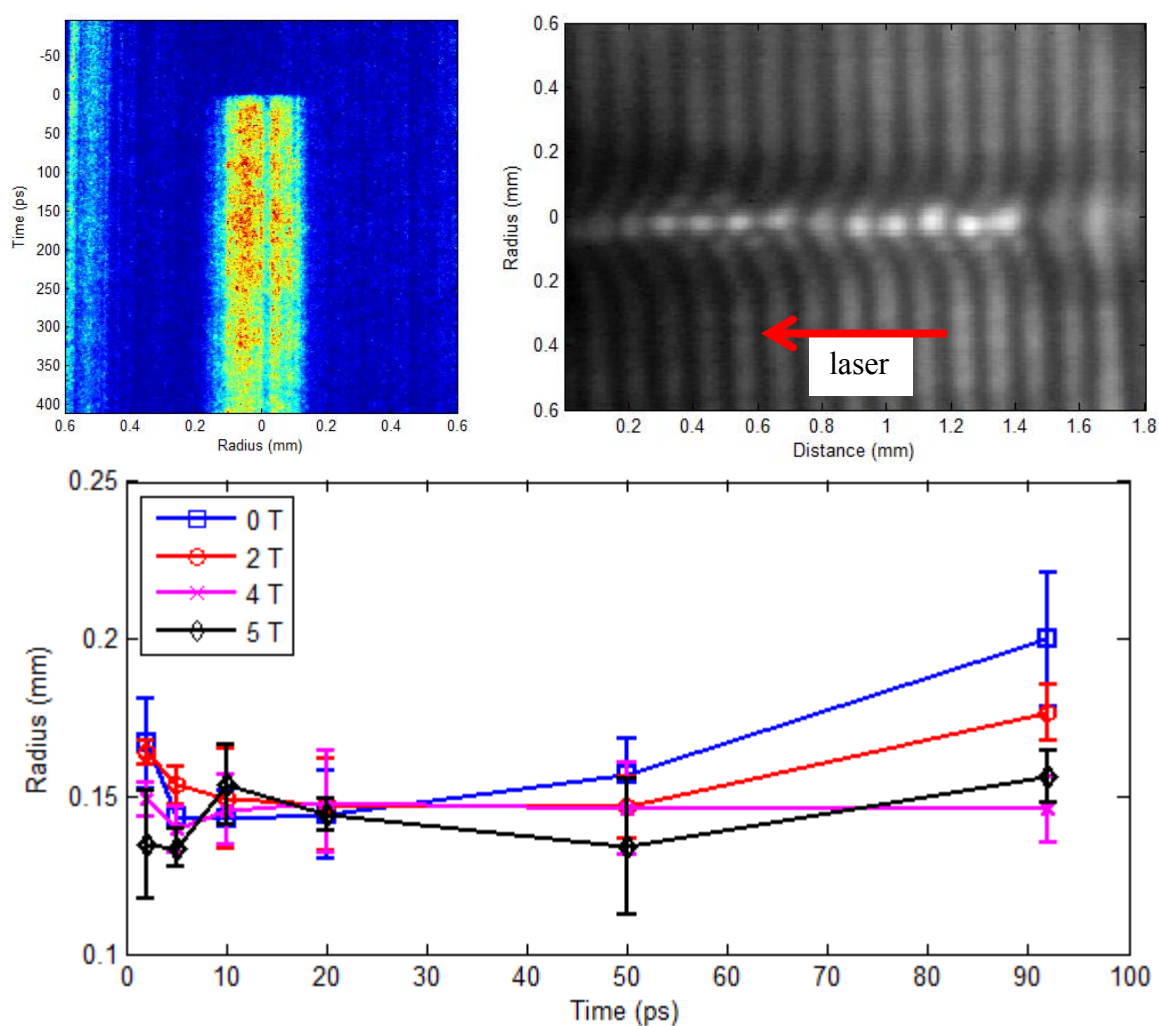
Figure 66.   Sample streakogram and 50 ps delay interferogram of 100 PSI neon plasma (top), and plot of the 10^{18} cm^{-3} electron density level as a function of time.

The data points at 92 ps disagree with this statement, but the 0 T and 2 T shots there were some of the highest energy shots taken during this data set, as well as at least 20% more energetic than the 4 T and 5 T shots at the same time delay, so it is not definite that the size difference there is real. In addition, we see that the field has essentially no effect on this plasma, which is to be expected from a low temperature plasma created by ionizing monomer gas.

Finally, we will examine the nitrogen data. Like the neon data, two data sets were taken, one at 150 PSI and one at 100 PSI. Overall, this data did not suffer from the problems of gas contamination, so conclusions can be drawn fairly easily. Figure 67 shows the plot of the 10^{18} cm^{-3} electron density level as a function of time for the 150 PSI nitrogen plasma. Interestingly, as mentioned previously, a rapid growth in size is seen right after the laser creates the plasma, which hints at a "ring of fire" type of phenomenon occurring. However, after that happens, very little expansion is seen later in time. This seems rather strange on the surface because the fast expansion would require quite a number of hot electrons, but the lack of growth later in time would seem to imply the
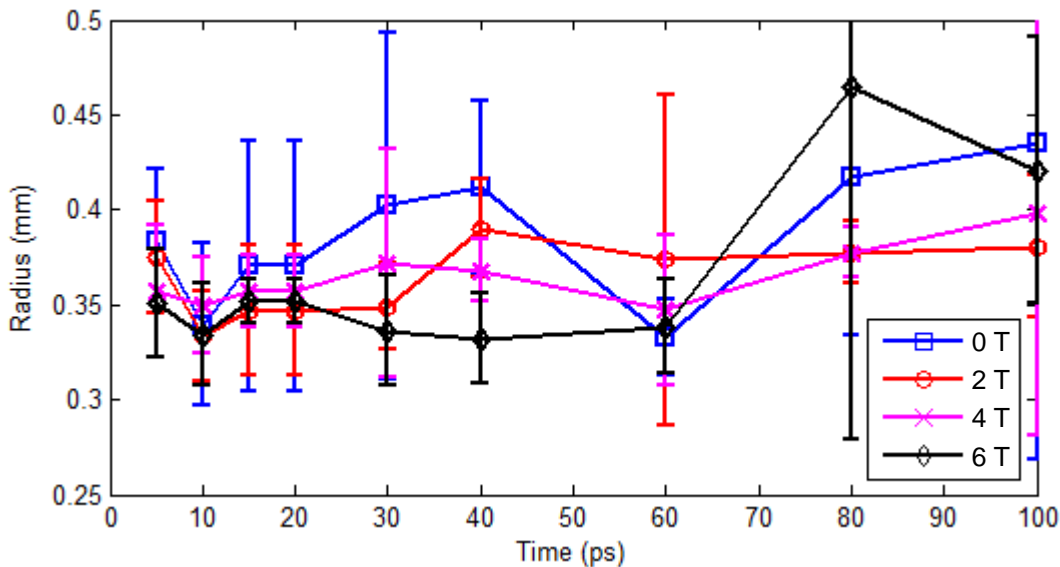
Figure 67.   Plot of the 10^{18} cm^{-3} contour as a function of time for nitrogen at 150 PSI. The plasma is larger initially, but no expansion is seen later, and so the magnetic field shows little effect.

plasma temperature is quite low. It is not immediately clear how this could happen. One possible explanation may be that there is a significant fraction of monomers in addition to small clusters, and when the clusters are ionized, almost all of those electrons get heated very strongly and go into causing the fast expansion, whereas the electrons ionized from the monomers are cold and get left behind. More detailed experiments would need to be performed to figure out exactly what is going on. We do see, though, that since the plasma is rather cold, the magnetic field does not affect the plasma size since the "ring of fire" is not affected by the field and there is no other plasma expansion for the field to inhibit.

The 100 PSI nitrogen data show a similar result, which is plotted in Figure 68. As with the 150 PSI data, there is an initial fast expansion (which is also observable between the 2 and 5 ps data points), and then after that, no further plasma evolution is seen. The streakogram image also makes this very clear. Once again, we see that the magnetic field has no effect on the plasma, essentially because there is nothing for it to affect. One interesting thing that is worth noting about this nitrogen data is the shape of the interferogram fringes. It will be especially enlightening when these are compared with an interferogram of the 100 PSI argon plasma from this same run, which will be seen in the next section. In Chapter 5, some argon interferograms were presented that showed the fringes were quite round. Looking at the interferogram in Figure 68, it is quite different in the nitrogen case (and somewhat in the neon case as well) – the fringes are sloped up to a central peak. If we compare an electron density profile retrieved from fringes like these (this particular lineout is from a 10 ps shot) and compare it to a log-scale plot of the laser intensity, the resemblance is very interesting. This comparison is shown in Figure 69. What we see is that the interior density, within a radius of about 150 μm, rather closely matches the laser intensity profile, and then there are low density wings extending out another 150-200 μm. Notice that the density of these wings stays below roughly 3×10^{18} cm^{-3}, which says that the ionization in this region is only up to $Z = 1$. This exactly matches what is expected for the "ring of fire". In addition, the laser itself can ionize nitrogen up to $Z = 5$ through barrier suppression ionization. Using Equation (2.10), the

intensity above which this can occur is roughly 1.5×10^{16} W/cm^2, which occurs inside a radius of 50 μm. The left half of the electron density profile (the right half suffered some phase unwrapping problems) seems to show that the area inside 50 μm is close to the expected electron density for Z = 5, about 1.5×10^{19} cm^{-3}. Based on this, it would seem that nitrogen (at this pressure) is mostly monomers with some percentage of clusters that have decent size, maybe up to 1 nm radius. However, the percentage of clusters is sufficient for there to be enough hot electrons to create the "ring of fire."
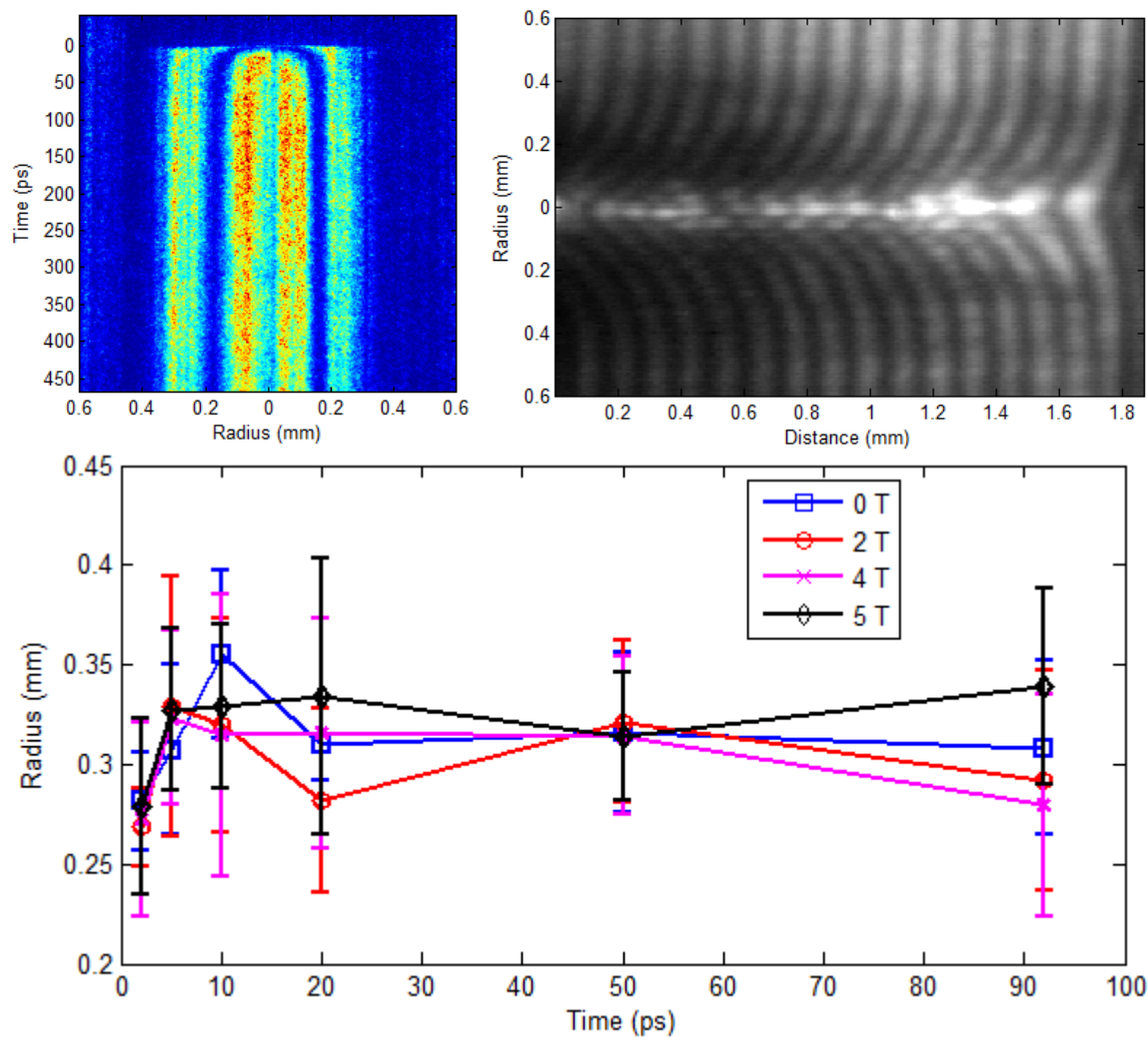
Figure 68.   Sample streakogram and 50 ps delay interferogram of 100 PSI nitrogen plasma (top), and plot of the 10^{18} cm^{-3} electron density level as a function of time and magnetic field strength.
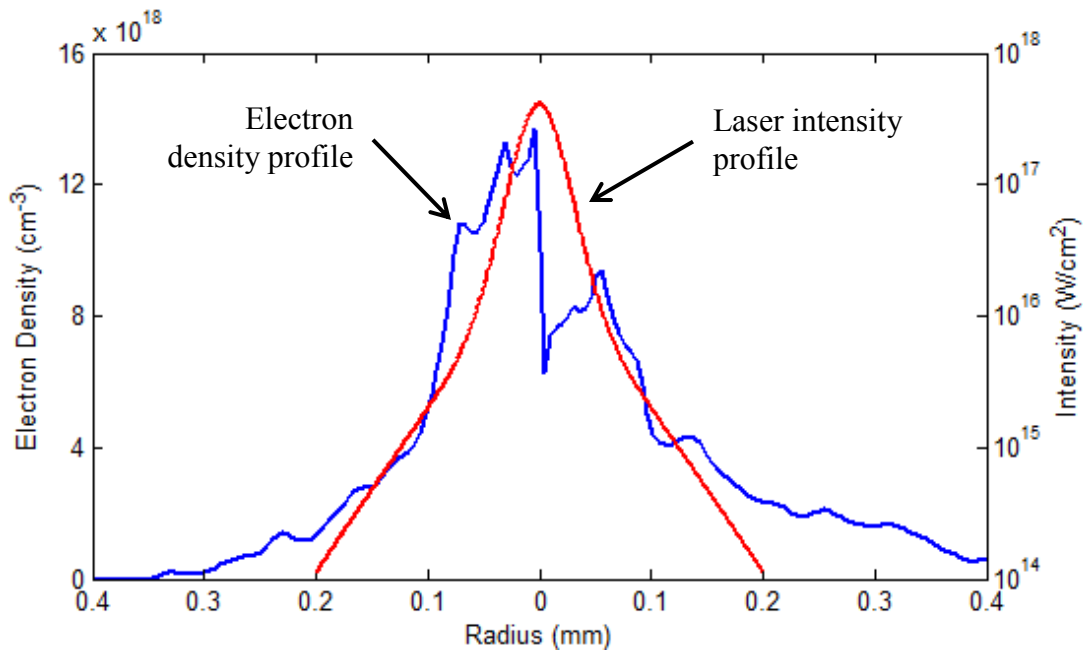
Figure 69.   Log-scale plot of the laser spatial profile (red) overlaid on the electron
density profile retrieved from a 100 PSI nitrogen interferogram (blue).

6.1.2. Argon Data

Unlike the gases in the previous section, when the argon plasma was exposed to the magnetic field, a very distinct difference was observed compared to when no field was present. In fact, the argon plasma also behaved differently without the field present when compared to the plasmas in the previous section. It is not completely clear why this is the case, but a reasonable assumption is that since the clusters in argon are the largest of the gases used, the overall temperature of the plasma created by the laser would have been the highest in this case for reasons described in Chapter 2.

First, let us examine the unmagnetized case. Figure 70 shows two sample interferograms taken of 150 PSI argon plasma when the field is not present. The time delay between the two snapshots is 75 ps, and the size of the plasma at the later time is noticeably larger, nearly 50% at the very low density level of 10^{18} cm^{-3}. Once again, we see that the interior electron density has increased with time, indicating that the "expansion" observed is likely the result of additional ionization. This is in contrast to the

plasmas observed in the previous section that showed little to no additional expansion after about 5 ps.

Ar, 150 PSI, 5 ps delay   Ar, 150 PSI, 80 ps delay
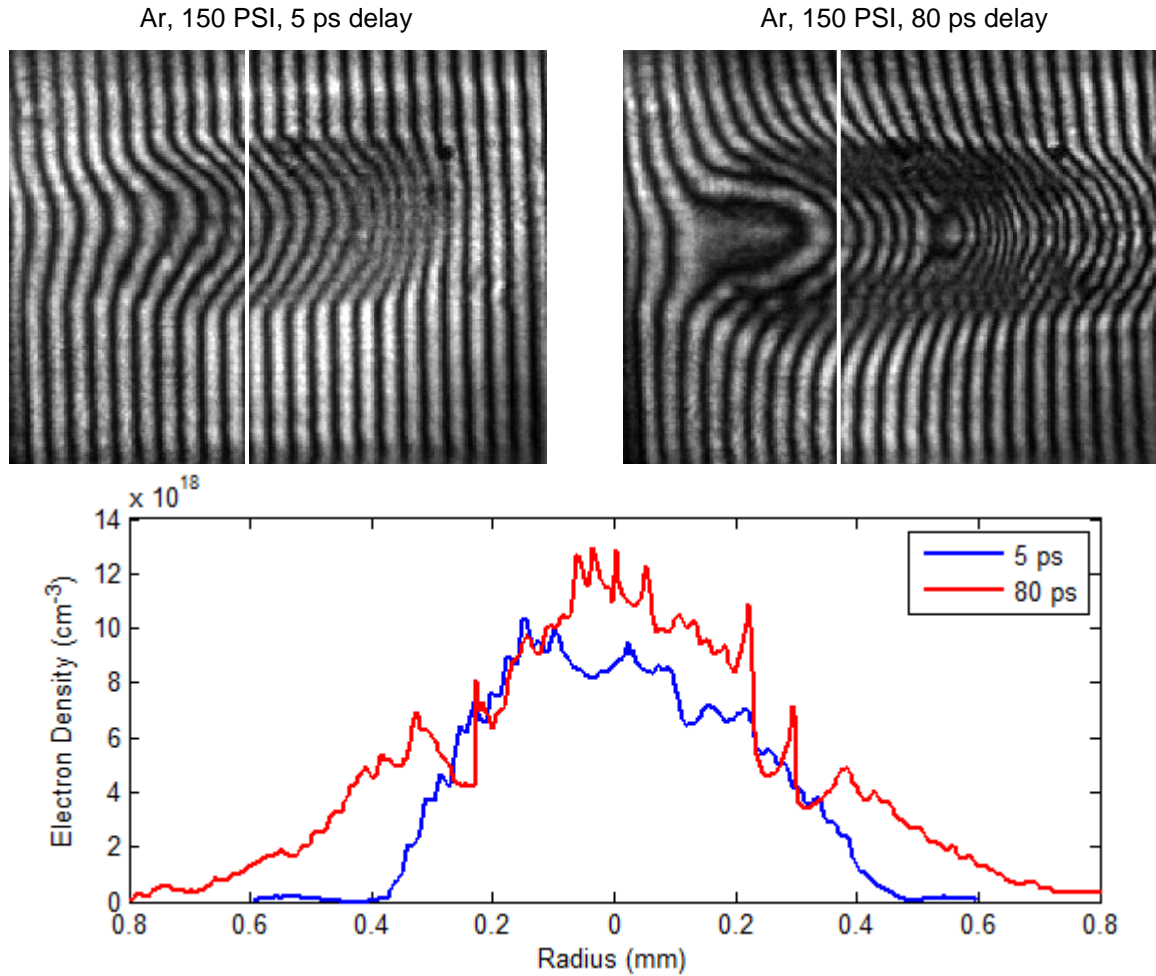
Figure 70. Two sample interferograms of unmagnetized argon plasma at different time delays with lineouts comparing the electron density. The white line on each image represents the location of the lineout.

Before moving on, a quick point should be made. It is clear that the later-time image on the right does not have a uniform radius along the laser propagation axis (the main laser moves from left to right). It would appear, then, that the laser energy was not uniformly absorbed as it passed through the cluster jet. However, as is seen in the left image, this non-uniform absorption does not appear to show itself until later in time, possibly when effects from the bulk of the thermal electrons begin to appear. To further

emphasize this point, Figure 71 shows an interferogram of the plasma at 10 ps delay. The width of the plasma is quite uniform in the region of the gas jet where the density is relatively uniform (the left ¼ – ⅓ is along the edge of the gas jet where the density drops off). So, while it seems that our assumption of uniform laser absorption is probably not totally correct, the creation of the hot electrons by the laser, and hence the behavior of the ionization wave described in Chapter 5, does seem to be uniform along the laser axis.
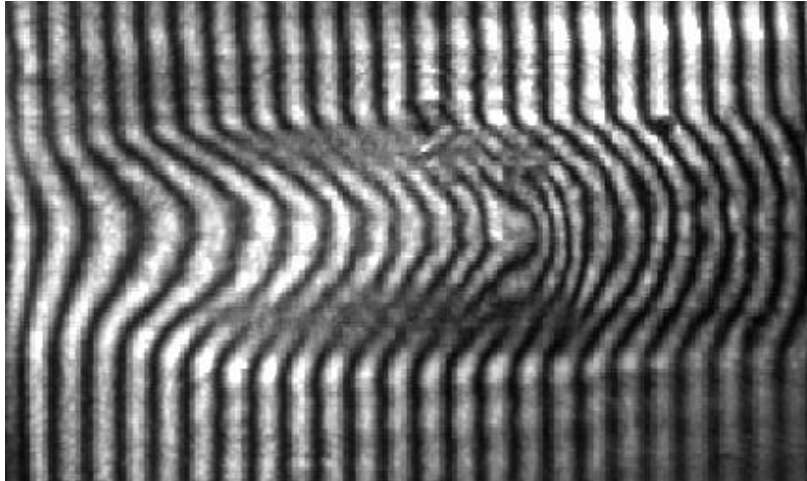
Figure 71.　Interferometric image of 150 PSI Ar plasma at a time delay of 10 ps.

The next thing to examine is how the plasma expands as a function of time. Measurements of the expansion velocity can give an estimate of the electron temperature, which will be useful for evaluating important parameters of the plasma such as the mean free path. Figure 72 shows data for two backing pressures of argon, 100 and 150 PSI, at time delays up to 100 ps after the plasma formation. Each set of data is plotted with a curve showing the average of the 10^{18} cm^{-3} contour location and a fit of each set of data to use for calculating the velocity (the displayed fit equation is for the units of the plot, mm and ps), and hence the temperature. Each data point corresponds to a single contour, so the 150 PSI data had two laser shots at each time point while the 100 PSI data had only one laser shot per point, but the finer temporal resolution helps make up for that in some way. However, the data point for 100 PSI at 80 ps, as well as both shots for 150 PSI at 100 ps, had much lower laser energy, which is why they deviate from the others. In

113

each case, the expansion of the plasma seems to begin to slow after 60-80 ps. The data plotted is from the z-position where the plasma expanded the most, which is approximately the location shown in Figure 70. The blue fit covers the time delays from
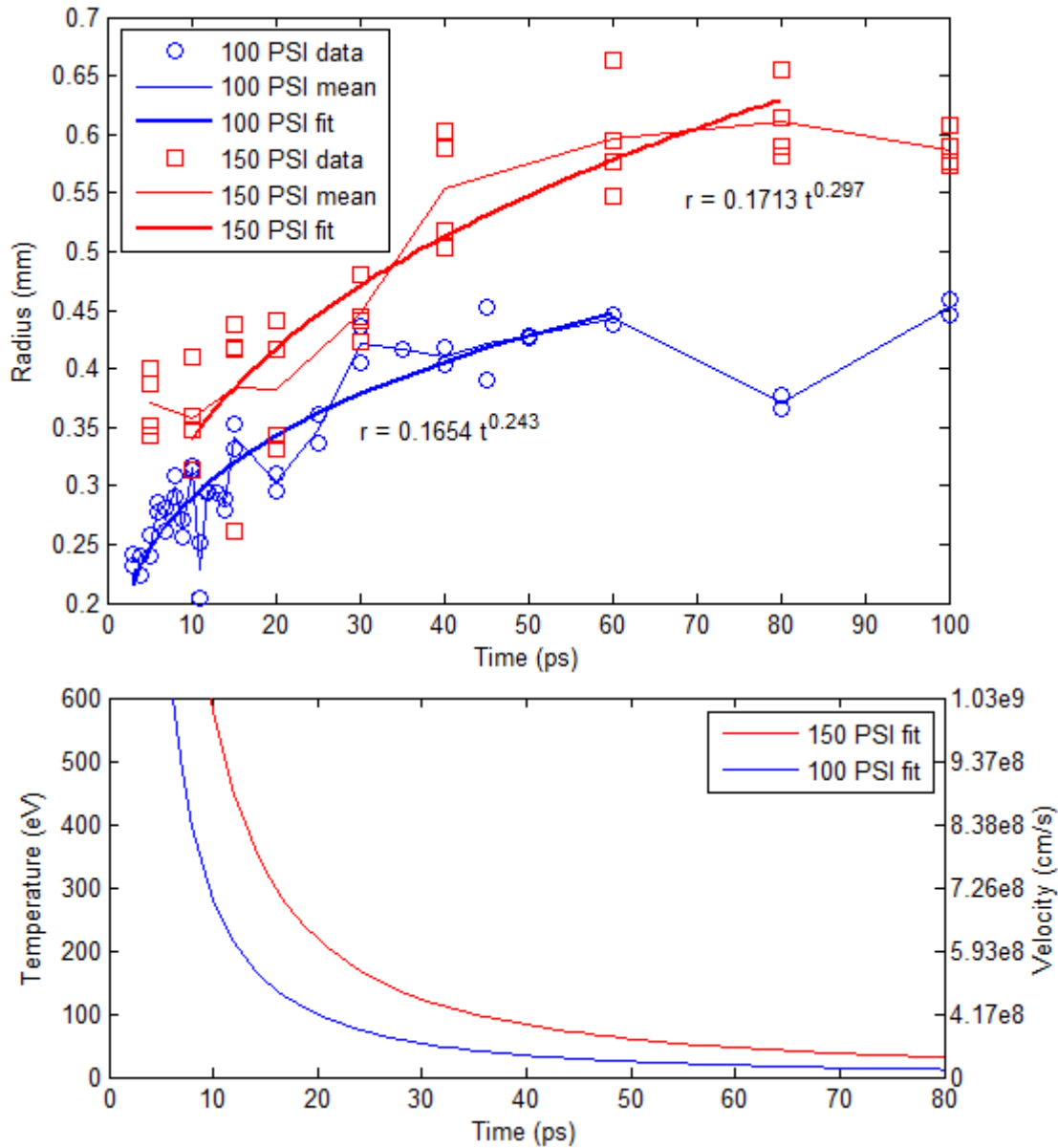
Figure 72. Plots of the 10^{18} cm^{-3} contour location for argon at two backing pressures as a function of time (top) with curve fits, and the resulting velocity and corresponding free-streaming electron temperature at the boundary (bottom).

3-60 ps, while the red curve covers time delays from 10-80 ps since the fast ionization wave from Chapter 5 makes the data points at 5 ps outside the trend of the other data. The resulting velocity, also shown in Figure 72, is simply the slope of each curve fit, and the electron temperature is estimated using Equation (5.6) (in this case, without the factor of two).

Looking closely at Figure 72, an argument could be made that the expansion of the plasma is not as uniform as the curve fits indicate, especially in the 150 PSI case. The data from 5 – 20 ps does appear to be relatively flat, indicating that little to no expansion is occurring during this time, and then from roughly 20 – 60 ps, a noticeable expansion occurs with stagnation again after 60 ps. As will be seen shortly, the streaked interferograms (admittedly for a different data set) do not seem to show the pause in the expansion during the first 20 ps, although this could be related to the lower temporal resolution of that diagnostic. A natural question to ask is why would there be a pause in the initial 20 ps of the plasma? A possible answer is that when the "ring of fire" rapidly expands the size of the plasma, the electron heat deposited by the laser has not had time to diffuse to the new boundary of the plasma. It would follow, then, that the pause observed after the initial fast expansion is the thermal wave related to electron heat conduction propagating through the plasma. Once it reaches the boundary after 20 ps, the plasma then starts expanding again because of the thermal wave propagation. This will be discussed in further detail in the next section.

The two data sets above were taken during the same experimental run, so it is easy to compare the results. Another data set of 100 PSI argon was taken during another run, and the results are fairly similar to the data above, which indicates that the results do seem to be reproducible. Figure 73 shows the same plot tracking the 10^{18} cm^{-3} contour location out to a time delay of 100 ps along with the curve fit to the data. The laser energy used for this data was generally about 15% higher than the previous data, but both data sets had considerable dither in the laser energy on target, at least ±15%, so there is still some overlap. Looking at the fit of the data, the expansion does track very closely to the data from before, so while the higher average laser energy does seem to result in an

115

observable difference in the size of the plasma, especially out near 100 ps and close to t = 0, it appears the expansion velocity in the 10-60 ps range is very similar. Also, we can see the pause in the expansion during the first 20 ps (and the curve fit does seem to help point this out), which would indicate this is a real effect.
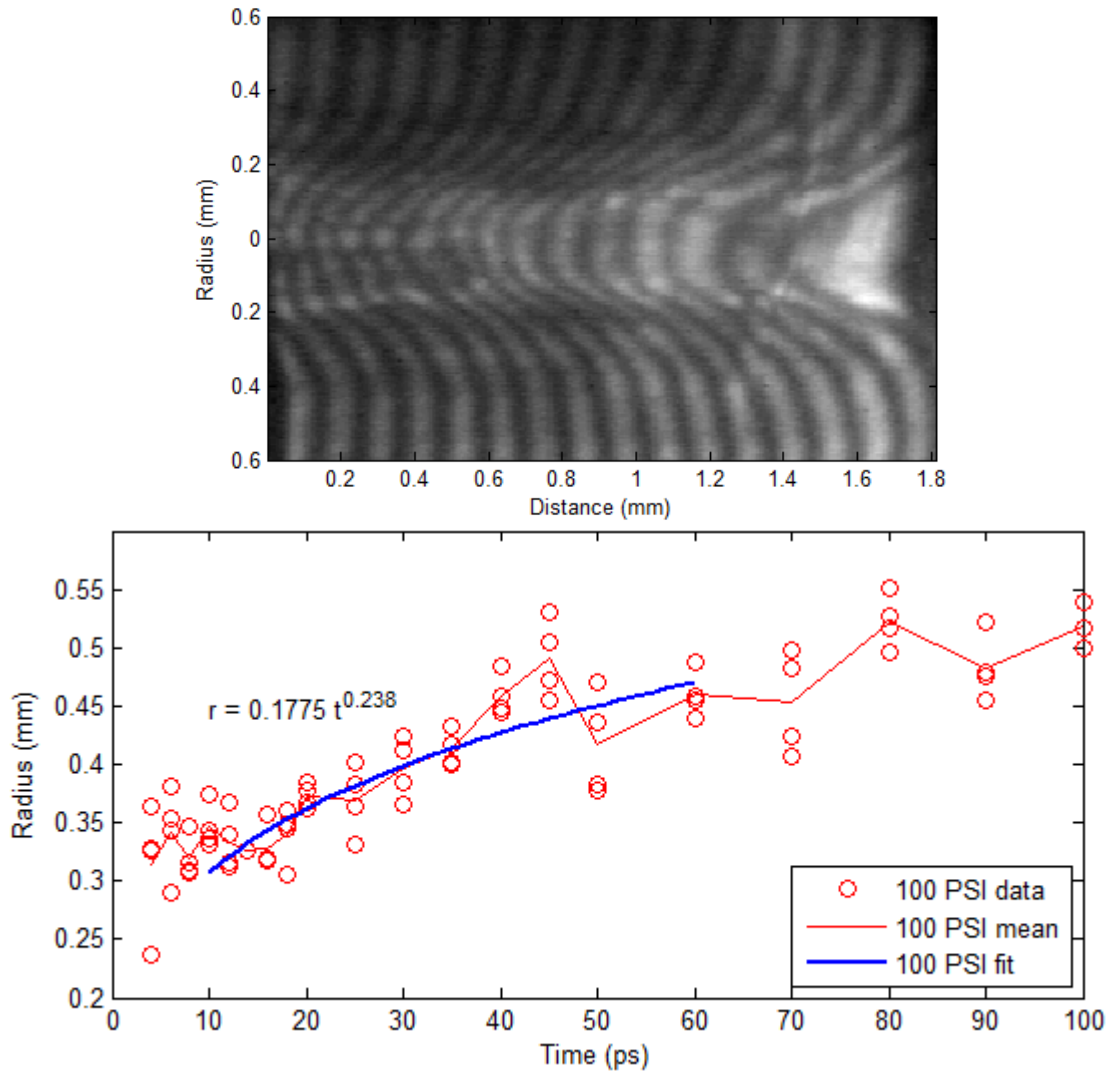
Figure 73.   Plot of second set of 100 PSI argon data with overlaid fit from 10-60 ps, along with a sample interferogram taken at 50 ps time delay.

The data above was the first set which also recorded data using the streakogram diagnostic, so we can directly compare the results of the two diagnostics. It should be pointed out that, unlike the data corresponding to Figure 70, the plasma expansion in this

116

data set was more uniform along the laser axis throughout the 100 ps, so that even though the streak camera is sampling only one radial cross section, the measured result in this case should be representative of the plasma as a whole. In fact, the streakogram allows us to easily see how the laser energy on the target can result in very clear differences in the plasma behavior. Figure 74 shows three streakograms which cover the low, middle, and high values of the laser energy recorded in this data set, and it is quite clear how both the plasma density (number of fringe shifts) and the width of the plasma vary depending on the laser energy into the cluster target. One advantage of this implementation of the diagnostic is that (relatively) constant density contours are immediately available from the image, and so tracking the expansion of the plasma can be done easily without having to go through the phase unwrapping and Abel inversion process.
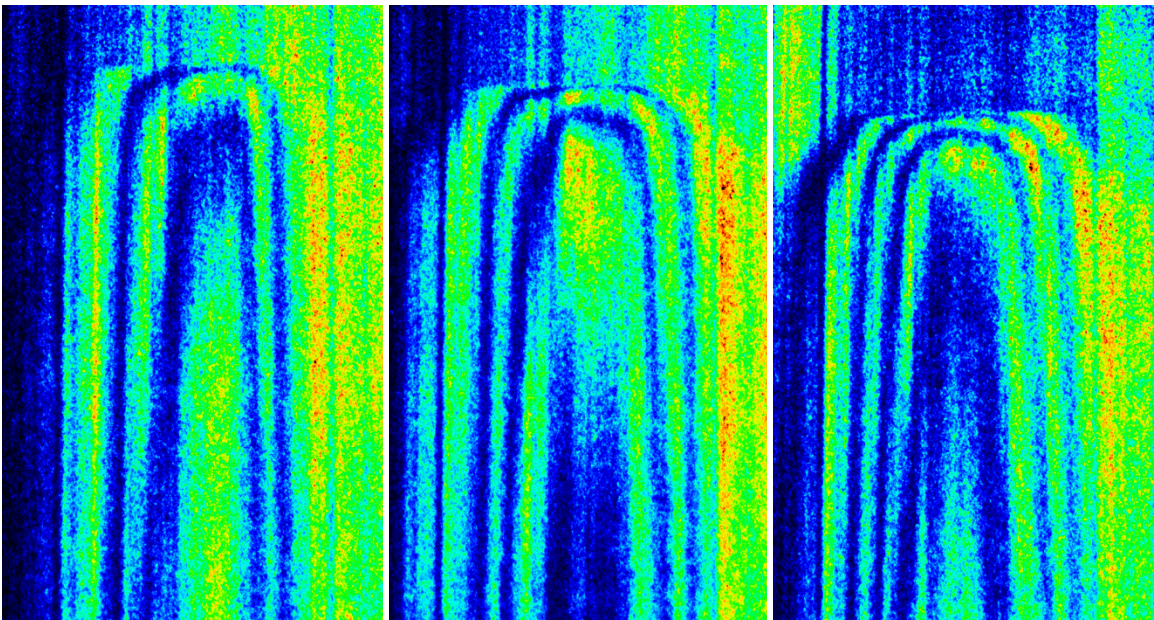
Figure 74.   Three sample streakograms representing plasmas created by laser energy on target of 0.8 J (left), 1.05 J (center), and 1.33 J (right). Each streak covers 500 ps with the time axis going from top to bottom.

In order to analyze these images in the way described above, some care must be taken. First, since the starting intensity of the fringe incident on the slit can vary (as seen above), we need to select images which have fairly similar initial intensities. Then, after

117

smoothing the images to remove high frequency noise, the same contour level is chosen. In this case, as seen in Figure 75, the contour level used was not far from the initial
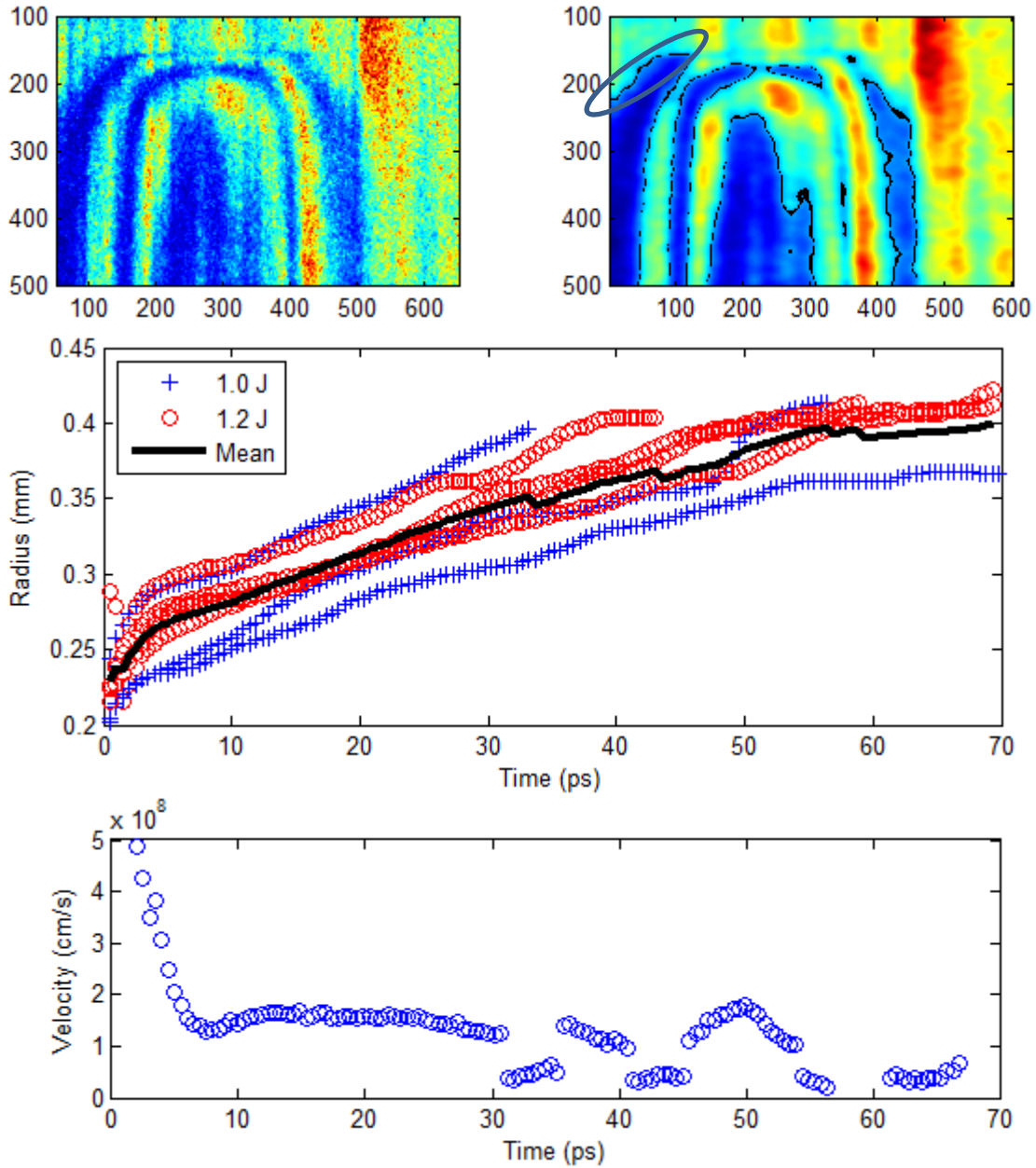
Figure 75.   Raw data image (top left), cropped for clarity, and resulting smoothed image using Fourier filtering (top right). Following contours at the same level for seven images produced the middle plot, and the slope of the resulting average of the contours gave the velocity (bottom).

intensity. The top images show an original data image (cropped) and the resulting image after smoothing using Fourier filtering. The black lines show the contour level chosen for the images plotted in the middle plot. With the irregularities which were often seen on the right side of the images, the left outside contour of each image was the one used to generate the data, indicated by the gray oval. The mean of all the curves is then calculated (the jumps result from some curves ending – for example, when the top plus's end at ~33 ps, the mean curve has a sudden jump), and the velocity is directly measured from the slope of the mean. Clearly, this velocity is noticeably lower than the velocities measured previously. The reason for this is likely because the 532 nm probe beam has decreased electron density resolution, so the electron density at this location is slightly higher, at least 2×10^{18} cm^{-3}. As was described in Chapter 5, the velocities measured at or below 10^{18} cm^{-3} were fairly similar, but as we used contours which were higher in density, especially above 2×10^{18} cm^{-3}, the velocity measured was not quite the same. Here, we see the same case. We can also see that, generally, higher energy laser shots produced wider plasmas.

The general conclusion from the data above is that, after the fast ionization described in Chapter 5, the argon plasma expands again by at least 50% in radius on a time scale of about 50 ps. The resulting expansion velocities are in the mid-upper 10^8 cm/s, so while these velocities are not relativistic, they are still quite fast. Once again, since the plasma density does not drop during this expansion (the streaked images definitely show this), we might suspect that additional ionization is part of this expansion. We will delve more into what exactly is causing this second fast expansion in the next section, but first, we need to compare this data when no external magnetic field is present to data when the field is present. Most of the data covered here will have field strengths up to about 5 T.

First, let us examine the data that corresponds to the first set of data presented. For the 150 PSI argon, shots were taken with field strengths of 2 T, 3 T, and 4 T, while the 100 PSI argon only had shots taken with a 3.5 T field. Figure 76 shows the position of the 10^{18} cm^{-3} contour for 150 PSI argon shots with no field (also plotted in Figure 72) and

the three field strengths listed above. Also plotted are curve fits to each data set between 10 and 80 ps. The 5 ps points were omitted as these are tied to the ionization wave, and the 100 ps points were omitted as the laser energy on those shots was noticeably lower, which is clear from the disagreement with the trends of the other data points. We observe an interesting effect of the field here, with the 2 T field seeming to show some inhibition of the expansion, while both the 3 T and 4 T field strengths strongly inhibit the expansion. This would imply that, for the conditions of this experiment, the threshold field strength required for the suppression of electron transport is right around 2 T.
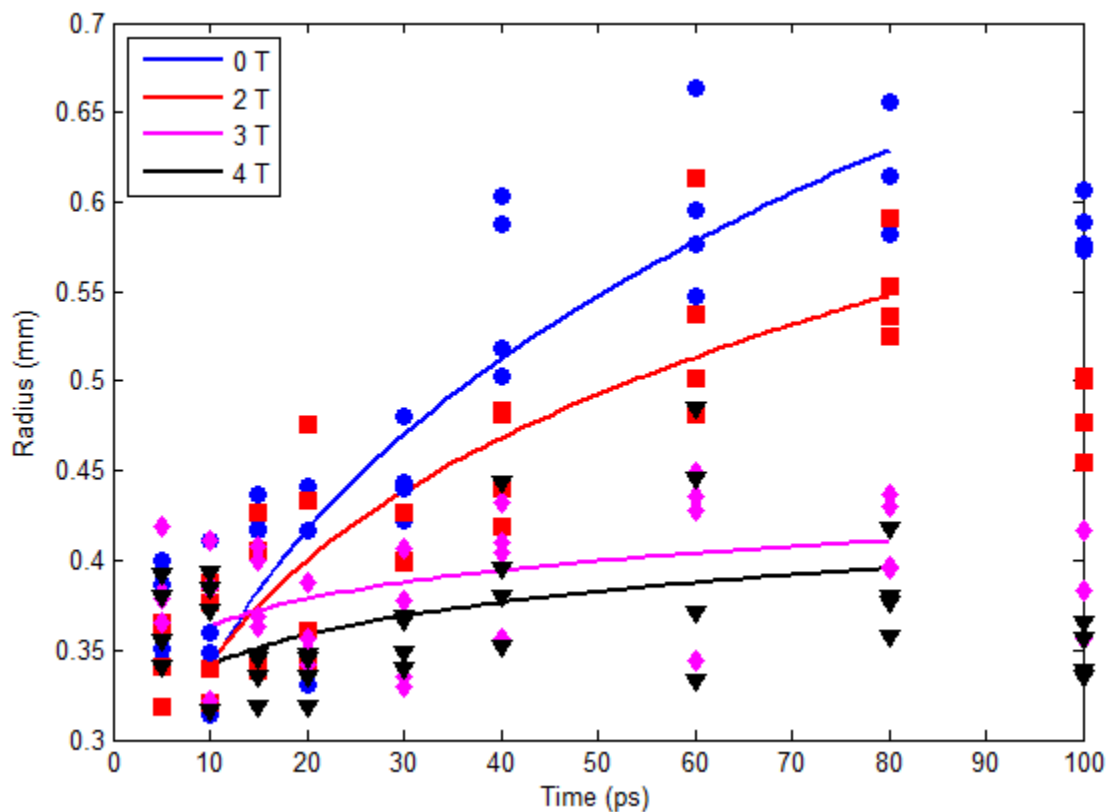
Figure 76.   Plots of the position of the 10^{18} cm^{-3} electron density contour for 150 PSI argon plasma with and without magnetic field present. Both the data points and the fits of the data between 10 and 80 ps show a clear effect of the stronger field strengths on the plasma expansion in this temporal regime.

Next, we can examine the effect of the magnetic field on the 100 PSI argon data. Figure 77 plots the no-field data from Figure 72 against data taken with a 3.5 T field

present. Once again, we see a strong inhibition of the plasma expansion when the field is present. Unfortunately, this data set only had the one field strength, but it offers further proof that the field is having an effect on these plasmas. However, we can look at 100 PSI argon from another data set which had the streakogram diagnostic in use. Figure 78 shows the raw interferograms for varying field strengths, similar to the data in Figure 76, along with the laser energy of each shot. We can see that the strong fields of 4 T and 5 T significantly suppress the expansion, while the 2 T shots seem to indicate that this field strength is again near the threshold value for when it begins to affect the plasma expansion (under these conditions).
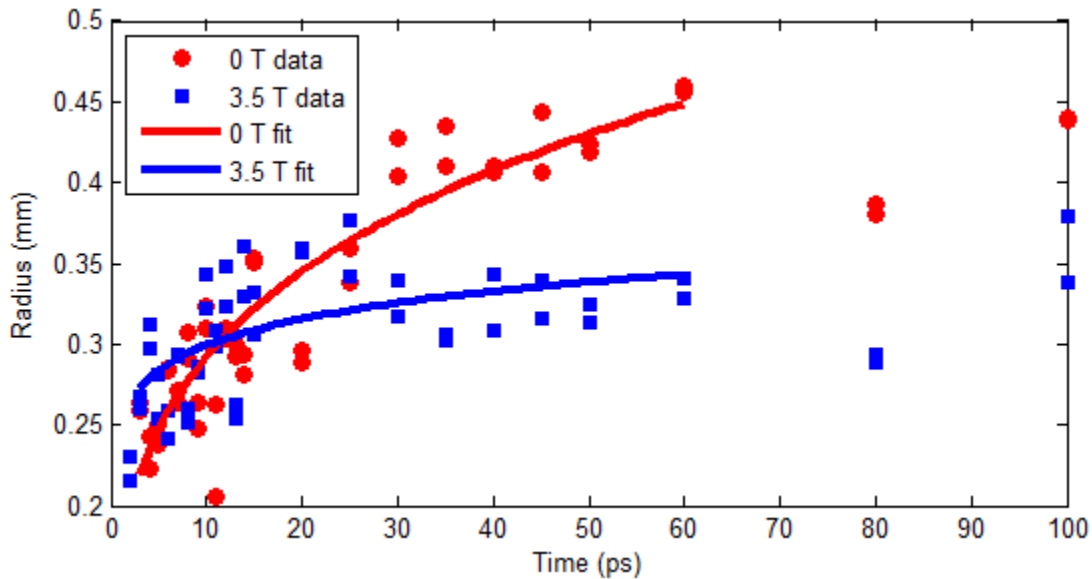
Figure 77.   Plot of data for 100 PSI argon with and without the magnetic field.

121
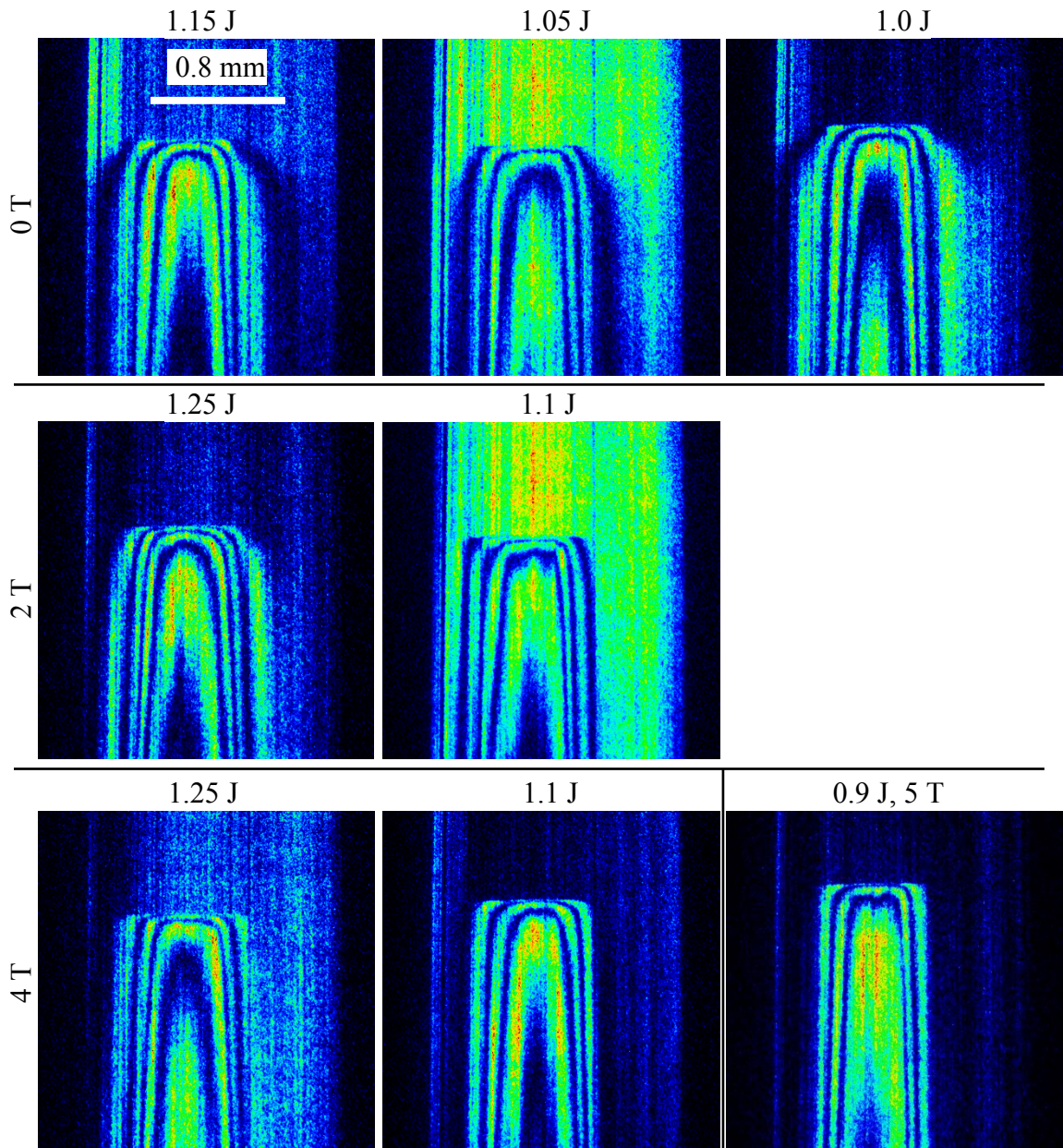
Figure 78.   Raw streakogram images of 100 PSI argon plasma with and without external field. Each image is a 500 ps streak with the laser energy on the shot listed above it. The results here show a similar effect of the field as observed in Figure 76.

6.2. THEORETICAL MODELING AND EXPLANATION

The electron temperature in the argon plasma created by the laser will be quite hot, with initial temperatures likely in the keV range after the fast expansion of Chapter 5. Naturally, there will be electron heat transport, whether through standard diffusion methods or via non-local effects [73,80]. One previous experiment demonstrated that a 12 T magnetic field quenched the non-local heat transport of electrons on a nanosecond time-scale [81], but we have demonstrated a clear effect of the field even on time-scales nearly two orders of magnitude less. Regardless of the exact method of heat transport, one common way of determining when the field will suppress this is by comparing the mean free path (MFP) of the electrons with the gyroradius. If the gyroradius is larger than the MFP, electrons will collide and transfer energy much like when no field is present. Conversely, if the gyroradius is smaller than the MFP, the electrons will only collide within the gyroradius, and hence the transport of energy will be inhibited.

Since there are many ways to calculate the mean free path, the method used here will be the one that seems to be the most applicable to our situation, but will also be simple. The plasma is expanding out into un-ionized gas, and so it would make sense to examine the MFP for collisions between electrons and neutral atoms (ionizing only the first electron). Using the simple formula for the MFP given by Equation (2.25), we need to know the cross section for ionization and the neutral gas density. From the beginning of Section 5.1, we know the gas density for the two backing pressures, and the ionization cross section for argon has been experimentally measured and tabulated for a range of temperatures [82]. We can also calculate the electron gyroradius for the various field strengths by using Equation (2.22). The result of these calculations is plotted in Figure 79 for 150 PSI argon. Remarkably, this simple calculation matches what the data in the previous section was predicting. Since the 2 T field has a gyroradius that is nearly equal to the MFP over a wide range of temperatures, it is reasonable to expect that this would be when we start to see some inhibition of heat transport. Similarly, since the gyroradius for the stronger fields is roughly a factor of two or more smaller than the MFP, it is not surprising at all that the plasma expansion was strongly inhibited by those field strengths.
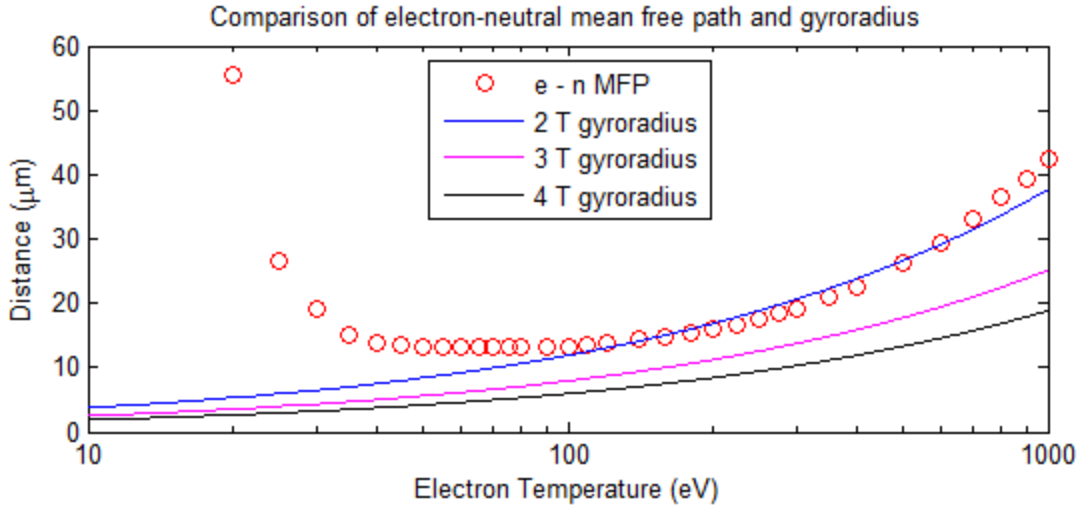
Figure 79. Plot comparing the mean free path (MFP) for electron-neutral collisions with the electron gyroradius for fields ranging from 2-4 T. Electron transport should be inhibited when the MFP becomes larger than the gyroradius.

Since the explanation above is related to the inhibition of heat transport, we wanted to try a simple 1D simulation to see if we could approximately reproduce the experimental observations. To do this, we used a simplified version of Equation (2.31) focusing simply on the evolution of the temperature from the heat transport,

$$\frac{3}{2} n_e \frac{dT_e}{dt} = -\nabla \cdot \vec{q}_e \tag{7.1}$$

where the electron heat flux $\vec{q}_e$ is given by the common equation,

$$\vec{q}_e = -\kappa \nabla T_e \tag{7.2}$$

with different relations for the thermal conductivity κ given for the case when no field is present (or propagation parallel to field lines) and for perpendicular propagation across the magnetic field. Simply using this equation to propagate heat will result in an unrealistically sharp temperature gradient, and in cases when the temperature is very high, the heat will propagate faster than is physically possible. A simple fix for this is to include a flux limiting factor which scales the free streaming value for the heat flux,

$$q_{FS} = n_e m_e \left(\frac{kT_e}{m_e}\right)^{3/2} \tag{7.3}$$

The value used in the transport equation for $\vec{q}_e$ can then be written as

$$\frac{1}{q_e} = \frac{1}{-\kappa \nabla T_e} + \frac{1}{f q_{FS}} \qquad (7.4)$$

where f is the flux limiting factor, often chosen to be between 0.03 and 0.1 to match experimental results [83].

Next, we need a way to evolve the electron density as the temperature changes. Of course, Equations (2.29-31) provide a way to do this, but it depends on a bulk fluid velocity, which we are assuming is 0 for this simple case. Instead, consider that when an area of plasma gains energy, some energy will go into heating the plasma while some will go into ionization. This is based on an assumption that the plasma is in a state where Saha ionization applies, which is questionable in our case, but might work for a first order simulation. This relation can be written as

$$E_{int} = \frac{3}{2} n_e k T_e + \frac{1}{3} \overline{Z}^3 I_H n_i \qquad (7.5)$$

where $\overline{Z}$ is the average ionization level and I_H is the ionization potential of hydrogen. Iterating between evolving the temperature and recalculating the electron density would produce a plot of the electron density as a function of time, which we can track at a similar level near the boundary like we did in the experimental data. Then, comparing the simulations with and without the field should show the effect of the field inhibiting electron heat transport. At this time, this work is still in progress, so we do not have results to show.

Chapter 7. Conclusion

The primary goal of this work was to build a pulsed power device to explore the difference in electron transport in a laser-produced plasma with an external magnetic field present. The time-scale of these observations ranged from sub-picosecond into the hundred picosecond range. After a number of technical difficulties were overcome, the pulsed power device was able to operate reliably in conjunction with the gas jet that was used to produce the target for the laser. Measured field strengths were up to 6 T with the coils that were used. Using argon gas that formed ~5 nm clusters, the laser created a warm plasma that expanded noticeably when no field was present. The external field, when larger than 2 T, was observed to inhibit this expansion on the tens of picoseconds scale. Simple estimates and modeling matched our conception of electron heat transport and collisional ionization being inhibited by the magnetic field.

A second very interesting observation was made during these experiments. A new collisionless ionization phenomenon was observed, with the actual mechanism of the ionization explained through the use of PIC simulations. In plasmas created with a sufficient number of hot electrons (hot meaning on the order of 100 keV in our case), the sheath field formed by the hot electrons trying to escape the plasma can become strong enough to ionize atoms outside the plasma. As the electrons ionized by the sheath field go into the plasma, they help create a potential well at the boundary which traps the hot electrons. This moving potential well with the strong sheath field continues to ionize atoms as long as the hot electrons in the well can maintain the field strength needed to ionize. Our observations of this ionization wave showed it had velocities as high as 0.5 c. It is also important to note that this wave propagated without additional energy input from the laser, as it was found to expand for nearly 2 ps after the laser had created the plasma. Also, it was observed that the wave was not affected by the magnetic field.

Finally, a few words will be said about future directions this work could be taken. Since the interferometry was really the only diagnostic used during these experiments, additional diagnostics could be implemented to learn more about the plasma and how it is

affected by the field. An obvious example would be using an x-ray pinhole camera or Thomson scattering to try and diagnose the electron temperature in the plasma. This would be especially useful for modeling purposes. In addition, with the somewhat ad-hoc discovery of the ionization wave, a number of parameters could be varied to study when the wave forms and when it doesn't, as well as possibly trying to optimize the expansion of the wave. In the case of fusion plasmas, it may be preferable to inhibit the wave (if it is present in these plasmas) so that the idea of electrostatically confining the ions by magnetically confining the electrons could possibly work better. Also, with the rather large spatial wings on the focal spot used for the experiments, it would be interesting to try and use a "cleaner" focal spot to see what effect this has on the wave.

References

[1] D. Strickland and G. Mourou, *Optics Communications* **56**: 219 (1985).

[2] G. Malka and J. L. Miquel, *Physical Review Letters* **77**: 75 (1996).

[3] E. L. Clark, K. Krushelnick, J. R. Davies, M. Zepf, M. Tatarakis, F. N. Beg, A. Machacek, P. A. Norreys, M. I. K. Santala, I. Watts, and A. E. Dangor, *Physical Review Letters* **84**: 670 (2000).

[4] M. Borghesi, A. J. MacKinnon, A. R. Bell, R. Gaillard, and O. Willi, *Physical Review Letters* **81**: 112 (1998).

[5] J. Lindl, *Physics of Plasmas* **2**: 3933 (1995).

[6] A. Modena, Z. Najmudin, A. E. Dangor, C. E. Clayton, K. A. Marsh, C. Joshi, V. Malka, C. B. Darrow, C. Danson, D. Neely, and F. N. Walsh, *Nature* **377**: 606 (1995).

[7] A. L'Huillier and Ph. Balcou, *Physical Review Letters* **70**: 774 (1993).

[8] A. Braun, G. Korn, X. Liu, D. Du, J. Squier, and G. Mourou, *Optics Letters* **20**: 73 (1995).

[9] E. W. Becker, K. Bier, and W. Henkes, *Zeitschrift für Physik A* **146**: 333 (1956).

[10] A. W. Castleman and R. G. Keesee, *Science* **241**: 36 (1988).

[11] T. Ditmire, J. Zweiback, V. P. Yanovsky, T. E. Cowan, G. Hays, and K. B. Wharton, *Nature* **398**: 489 (1999).

[12] T. Donnelly, T. Ditmire, K. Neuman, M. D. Perry, and R. W. Falcone, *Physical Review Letters* **76**: 2472 (1996).

[13] T. Ditmire, R. A. Smith, and M. H. R. Hutchinson, *Optics Letters* **23**: 322 (1998).

[14] T. Ditmire, K. Shigemori, B. A. Remington, K. Estabrook, and R. A. Smith, *The Astrophysical Journal Supplement Series* **127**: 299 (2000).

[15] L. V. Keldysh, *Soviet Physics JETP* **20**: 1307 (1965).

[16] P. Agostini, F. Fabre, G. Mainfray, G. Petite, and N. K. Rahman, *Physical Review Letters* **42**: 1127 (1979).

[17] B. Yang, K. J. Schafer, B. Walker, K. C. Kulander, P. Agostini, and L. F. DiMauro, *Physical Review Letters* **71**: 3770 (1993).

[18] L. D. Landau and E. M. Lifshitz, *Quantum Mechanics*, Pergamon, New York (1965).

[19] M. V. Ammosov, N. B. Delone, and V. P. Krainov, *Soviet Physics JETP* **64**: 1191 (1986).

[20]   S. Augst, D. D. Meyerhofer, D. Strickland, and S. L. Chin, *Journal of the Optical Society of America B* **8**: 858 (1991).

[21]   T. Ditmire, T. Donnelly, A. M. Rubenchik, R. W. Falcone, and M. D. Perry, *Physical Review A* **53**: 3379 (1996).

[22]   I. Last and J. Jortner, *Physical Review A* **60**: 2215 (1999).

[23]   C. Siedschlag and J. M. Rost, *Physical Review A* **67**: 013404 (2003).

[24]   W. Lotz, *Zeitschrift fur Physik* **216**: 241 (1968).

[25]   T. Ditmire, J. W. G. Tisch, E. Springate, M. B. Mason, N. Hay, R. A. Smith, J. Marangos, and M. H. R. Hutchinson, *Nature* **386**: 54 (1997).

[26]   M. Lezius, S. Dobosz, D. Normand, and M. Schmidt, *Physical Review Letters* **80**: 261 (1998).

[27]   K. W. Madison, P. K. Patel, M. Allen, D. Price, R. Fitzpatrick, and T. Ditmire, *Physical Review A* **70**: 053201 (2004).

[28]   B. N. Breizman, A. V. Arefiev, and M. V. Fomyts'kyi, *Physics of Plasmas* **12**: 056706 (2005).

[29]   G. J. Pert, *Journal of Physics A: General Physics* **5**: 506 (1972).

[30]   F. Brunel, *Physical Review Letters* **59**: 52 (1987).

[31]   Y. L. Shao, T. Ditmire, J. W. G. Tisch, E. Springate, J. Marangos, and M. H. R. Hutchinson, *Physical Review Letters* **77**: 3343 (1996).

[32]   L. M. Chen, J. J. Park, K.-H. Hong, J. L. Kim, J. Zhang, and C. H. Nam, *Physical Review E* **66**: 025402 (2002).

[33]   Y. Fukuda, Y. Akahane, M. Aoyama, Y. Hayashi, T. Homma, N. Inoue, M. Kando, S. Kanazawa, H. Kiriyama, S. Kondo, H. Kotaki, S. Masuda, M. Mori, A. Yamazaki, K. Yamakawa, E. Yu. Echkina, I. N. Inovenkov, J. Koga, and S. V. Bulanov, *Physics Letters A* **363**: 130 (2007).

[34]   J. Purnell, E. M. Snyder, S. Wei, and A. W. Castleman, Jr., *Chemical Physics Letters* **229**: 333 (1994).

[35]   T. Ditmire, J. Zweiback, V. P. Yanovsky, T. E. Cowan, G. Hays, and K. B. Wharton, *Nature* **398**: 489 (1999).

[36]   J. Zweiback, T. E. Cowan, J. H. Hartley, R. Howell, K. B. Wharton, J. K. Crane, V. P. Yanovsky, G. Hays, R. A Smith, and T. Ditmire, *Physics of Plasmas* **9**: 3108 (2002).

[37]   F. F. Chen, *Introduction to Plasma Physics and Controlled Fusion, 2nd Edition*, Springer Science+Business Media, New York, (2006).

[38] L. J. Spitzer, *Physics of Fully Ionized Gases*, John Wiley & Sons, New York, (1962).

[39] S. I. Braginskii, *Transport Processes in a Plasma*, in *Review of Plasma Physics*, Consultants Bureau, New York, (1965).

[40] J. D. Huba, *NRL Plasma Formulary*, Naval Research Laboratory (2006).

[41] L. Spitzer, *Physics of Fully Ionized Gases*, Interscience, New York (1962).

[42] D. Bohm, E. H. S. Burhop, and H. S. W. Massey, *The Characteristics of Electrical Discharges in Magnetic Fields*, ed. A. Guthrie and R. K. Wakerling, McGraw-Hill, New York, (1949).

[43] O. V. Gotchev, J. P. Knauer, P. Y. Chang, N. W. Jang, M. J. Shoup, III, D. D. Meyerhofer, and R. Betti, *Review of Scientific Instruments* **80**: 043504 (2009).

[44] F. Paschen, *Annalen der Physik* **273**: 69 (1889).

[45] B. C. Wadell, *Transmission Line Design Handbook*, Artech House, Boston, (1991).

[46] J. D. Jackson, *Classical Electrodynamics*, John Wiley & Sons, Inc., New York (1999).

[47] D. A. Ward and J. L. T. Exon, *Engineering Science Education Journal* **2**: 105 (1993).

[48] I. H. Hutchinson, *Principles of Plasma Diagnostics*, Cambridge University Press, New York, (1987).

[49] E. S. Barr, *Applied Optics* **4**: 631 (1967).

[50] G. Auday, Ph. Guillot, J. Galy, and H. Brunet, *Journal of Applied Physics* **83**: 5917 (1998).

[51] R. Hackam and G. R. Raju, *Journal of Applied Physics* **45**: 4784 (1974).

[52] P. K. Loewenhardt, B. D. Blackwell, and Beichao Zhang, *Review of Scientific Instruments* **64**: 3334 (1993).

[53] W. Koechner, *Solid-State Laser Engineering*, Springer-Verlag, Berlin (1996).

[54] G. Hays, "Development of Broad Spectrum Technologies for High Energy Chirped Pulse Amplification", Ph.D. Thesis, The University of Texas at Austin, 2007.

[55] G. Wagner, M. Shiler, and V. Wulfmeyer, *Optics Express* **13**: 8045 (2005).

[56] F. G. Patterson, J. Bonlie, D. Price, and B. White, *Optics Letters* **24**: 963 (1999).

[57] W. Grigsby, "Experimental Studies of High Energy Density Silicon Using Ultra-Fast Lasers", Ph.D. Thesis, The University of Texas at Austin, 2007.

[58] Y. X. Chu, X. Y. Liang, L. H. Yu, L. Xu, X. M. Lu, Y. Q. Liu, Y. X. Leng, R. X. Li, and Z. Z. Xu, *Laser Physics Letters* **10**: 055302 (2013).

[59] E. W. Gaul, M. Martinez, J. Blakeney, A. Jochmann, M. Ringuette, D. Hammond, T. Borger, R. Escamilla, S. Douglas, W. Henderson, G. Dyer, A. Erlandson, R. Cross, J. Caird, C. Ebbers, and T. Ditmire, *Applied Optics* **49**: 1676 (2010).

[60] P. F. Moulton, *Proceedings of the IEEE* **80**: 348 (1992).

[61] I. Ross, P. Matousek, G. New, and K. Osvay, *Journal of the Optical Society of America B* **19**: 2945 (2002).

[62] S. Feldman, "Isochoric Heating of Copper to Warm Dense Matter State Using Protons Produced Through Laser Solid Interactions", Ph.D. Thesis, The University of Texas at Austin, 2013.

[63] K. Struve, J. Argo, R. Bengtson, D. Headley, J. Kellogg, S. Lewis, H. Quevedo, M. Savage, B. Stoltzfus, C. Waugh, and M. Wisher, *IEEE Pulsed Power Conference Proceedings*, Chicago, IL (2011).

[64] M. Deutsch and I. Beniaminy, *Applied Physics Letters* **41**: 27 (1982).

[65] D. C. Ghiglia and M. D. Pritt, *Two-Dimensional Phase Unwrapping: Theory, Algorithms, and Software*, John Wiley and Sons, Inc. (1998).

[66] O. F. Hagena, *Review of Scientific Instruments* **63**: 2374 (1992).

[67] J. Wormer, V. Guzielski, J. Stapelfeldt, and T. Moller, *Chemical Physics Letters* **159**: 321 (1989).

[68] F. Dorchies, F. Blasco, T. Caillaud, J. Stevefelt, C. Stenz, A. S. Boldarev, and V. A. Gasilov, *Physical Review A* **68**: 023201 (2003).

[69] U. Buck and R. Krohne, *The Journal of Chemical Physics* **105**: 5408 (1996).

[70] A. Henig, "Ultrafast Dynamics in Explosions of Atomic Clusters Irradiated by Ultra-High Intensity Laser Pulses", Masters Thesis, The University of Texas at Austin, 2005.

[71] H. Lu, G. Ni, R. Li, and Z. Xu, *The Journal of Chemical Physics* **132**: 124303 (2010).

[72] K. Y. Kim, V. Kumarappan, and H. M. Milchberg, *Applied Physics Letters* **83**: 3210 (2003).

[73] T. Ditmire, E. T. Gumbrell, R. A. Smith, A. Djaoui, and M. H. R. Hutchinson, *Physical Review Letters* **80**: 720 (1998).

[74] E. T. Gumbrell, A. S. Moore, J. A. Lazarus, E. L. Clark, P. M. Nilson, W. J. Garbett, A. J. Comley, J. S. Robinson, M. Hohenberger, R. D. Edwards, R. E.

Eagleton, R. J. Clarke, D. R. Symes, and R. A. Smith, *New Journal of Physics* **10**: 123011 (2008).

[75] X. Gao, X. Wang, B. Shim, A. V. Arefiev, R. Korzekwa, and M. C. Downer, *Applied Physics Letters* **100**: 064101 (2012).

[76] A. V. Arefiev, X. Gao, M. R. Tushentsov, X. Wang, B. Shim, B. N. Breizman, and M. C. Downer, *High Energy Density Physics* **6**: 121 (2010).

[77] M. R. Talukder, S. Bose, M. A. R. Patoary, A. K. F. Haque, M. A. Uddin, A. K. Basak, and M. Kando, *European Physical Journal D* **46**: 281 (2008).

[78] *Introduction to Computational Methods in Many Body Physics*, edited by Michael Bonitz and Dirk Semkat, Rinton, Princeton, NJ (2006).

[79] J. Arno and J. W. Bevan, *Jet Spectroscopy and Molecular Dynamics*, edited by J. M. Hollas and D. Phillips, Blackie, London (1995).

[80] J. F. Luciani, P. Mora, and J. Virmont, *Physical Review Letters* **51**: 1664 (1983).

[81] D. H. Froula, J. S. Ross, B. B. Pollock, P. Davis, A. N. James, L. Divol, M. J. Edwards, A. A. Offenberger, D. Price, R. P. J. Town, G. R. Tynan, and S. H. Glenzer, *Physical Review Letters* **98**: 135001 (2007).

[82] R. Rejoub, B. G. Lindsay, and R. F. Stebbings, *Physical Review A* **65**: 042713 (2002).

[83] P. Mora and J. F. Luciani, *Laser and Particle Beams* **12**: 387 (1994).

Vita

Matthew Warren McCormick was born in Denver, Colorado, in 1983, the son of William and Beryle McCormick. After graduating as valedictorian from Caliche Jr./Sr. High School in Iliff, Colorado, he attended Rose-Hulman Institute of Technology in Terre Haute, Indiana. He received his B.S. (Cum Laude) with a double major in Mathematics and Physics in 2005. In fall of 2005, he entered the Physics graduate program at the University of Texas at Austin.

Email address: mccormm@physics.utexas.edu

This dissertation was typed by the author.